COMBINED EXPERIMENTAL/THEORETICAL APPROACH TOWARD THE DEVELOPMENT OF CARBON TOLERANT ELECTROCATALYSTS FOR SOLID OXIDE FUEL CELL ANODES

by

Eranda Nikolla

A dissertation submitted in partial fulfillment
of the requirements for the degree of
Doctor of Philosophy
(Chemical Engineering)
in The University of Michigan
2009

Doctoral Committee:

Assistant Professor Suljo Linic, Co-chair
Professor Johannes W. Schwank, Co-chair
Professor Erdogan Gulari
Professor John W. Halloran
Professor Phillip E. Savage

2009

"The most important thing in science is not so much to obtain new fact as to discover new ways of thinking about them"

Sir William Bragg (1862-1942)

"The important thing is not to stop questioning"

Albert Einstein (1879-1955)

This dissertation is dedicated to my parents Liljana and Nik Nikolla for all their love and endless support.

ACKNOWLEDGEMENTS

I would first like to thank my advisors Prof. Suljo Linic and Prof. Johannes Schwank for their help and support throughout my graduate studies. I would like to express my thanks to Prof. Linic for his guidance and mentoring. He has been instrumental to my academic growth. He has introduced me to the combined experimental and theoretical approach, which has had a great impact on my thesis work. I would like to thank Prof. Schwank for being very supportive of all my decisions during graduate school. I appreciate his constant support and for allowing me to attend multiple conferences and important seminars.

I would like to thank my thesis committee: Prof. Phillip Savage, Prof. John Halloran and Prof. Erdogan Gulari. I am very thankful to Prof. Savage for all his support and willingness to listen and share his advice with me in multiple occasions. I would like to thank Prof. Halloran for his help with synthesizing the solid oxide fuel cells. I really appreciate his readiness to help me all the time. I would also like to thank Prof. Gulari for being very supportive of my work.

I believe that the Department of Chemical Engineering at the University of Michigan has a number of great individuals as part of their departmental staff. I would like to thank Leslie Cypert and Sandy Swisher for all their help and consistent support. Furthermore, I would also like to acknowledge Claire O'Conner, Linda Casto, Susan Hamlin, Shelly Fellers, Ruby Sowards, Christine Moellering and Tina Jimenez for their

help. I would also like to thank Harald Eberhart for designing and building my quartz reactors and boats. I really appreciate his willingness to help every time I knocked on his door.

I also believe that I have had the great opportunity to work with bright individuals in both the Linic and Schwank research groups. I really appreciate their support and assistance. These individuals are: Linic research group: Siris Laursen, Hongliang Xin, Neil Schweitzer, David Ingram, Phillip Christopher, Adam Holewinski, Matthew Morabito, Katrina Ramsdell and Schwank research group: Tom Gilbert, Jim Bucher, Joe Mayne, Ben Harris, Liz Ranney, Tom Westerich, Sameer Parvathikar, Steve Edmund, Xiaoyin Chen, Hui Feng. I would like to wish them all the best during the rest of their graduate studies and in their future careers.

I have also been very fortunate to have had the opportunity to work with a number of great undergraduate students. I would like to thank Adam Holewinski (now a graduate student in Prof. Linic's group) for performing some of the initial density functional theory work. I would like to thank Teresa Mitisi for being very helpful with synthesizing supported catalyst and solid oxide fuel cells. I would like to thank Matt Morobito (now a graduate student in Prof. Linic's group) for all his help with synthesizing and testing solid oxide fuel cells. I would also like to thank Preeta Maitra for help with synthesizing solid oxide fuel cells.

At University of Michigan I have also met a number of individuals that have greatly impacted my graduate work. I would like to thank Dr. Kai Sun for his tremendous help with electron microscopy and spectroscopy. I really appreciate his endless patience in helping me with operating the scanning electron microscope and the electron energy

loss spectroscopy. I would also like to thank Dr. Andy Tadd for his help with editing my qualifying and preliminary examinations. I really appreciate his support especially during my first two years of graduate school. I would like to thank Dr. Joydeep Mukherjee for his help when he was a postdoctoral fellow in Prof. Linic's group. I really appreciate his help with density functional theory calculations.

I would like to express my deepest gratitude my best friend, Maha Hammoud, for all her support and help throughout my stay at the University of Michigan. She has been more than a friend; she has been like a sister that has always advised and supported me. She has been part of my family in Ann Arbor. I would also like to thank her husband, Ali, for all his support and her daughter Alma for being so loving. I would also like to congratulate her on the new addition to her family, her baby girl Rina.

I would also like to thank Dr. Valarie Thomas for being a great friend. It has been a great pleasure getting to know her and I really appreciate all her support. I also would like to thank Natalie Rebacz for being a great friend and always supporting me. It has been great getting to know her and I wish her all the best in her future endeavors. I would also like to acknowledge Peter Aurora, Hima Nandivada, Saadet Albayrak, Bilge Ozel, Desh Mukhija, Khamir Mehta and Tony Lachawiec for being great friends.

I would not be in graduate school if it were not for the advice and consistent support of my undergraduate advisor Prof. Kenneth Harmon. He was instrumental in convincing me to pursue my graduate studies. I cannot thank him enough for giving me the opportunity to work in his lab. I am in debt to him for his guidance and support throughout my undergraduate studies.

I would also like to acknowledge my friends Bonnie and Thomas Willick for their consistent support during my graduate studies. I cannot thank them enough for their help and encouragement every step of the way.

Last but not least, I would like to thank my family for their endless love and consistent support. I would like to thank my brother for always encouraging me and being supportive of my decisions. I would also like to thank his wife Magdalena for her support and my niece Fiona for being so joyous and loving all the time. I would like to express my sincere thanks to my parents Liljana and Nik Nikolla. They are the best parents in the world and I don't think that there exist enough words to express my gratitude to them for sacrificing a lot so my brother and I can succeed in life. I am proud to be their daughter, to have known and learned from them.

TABLE OF CONTENTS

LIST OF FIGURES

Figure

LIST OF TABLES

ABSTRACT

The main objective of this dissertation was to utilize a molecular approach combining DFT calculations and numerous experimental techniques to develop carbon tolerant electrocatalysts for solid oxide fuel cell (SOFC) anodes. SOFCs are solid-state electrochemical devices that can convert the chemical energy of hydrogen, CO, and hydrocarbons into electrical energy. One of the main issues associated with the direct operation of SOFCs using hydrocarbons is the deactivation of the conventional anode electrocatalysts, such as Ni on yttria-stabilized zirconia (YSZ) due to the formation of carbon deposits.

To tackle the problem of carbon-induced deactivation of Ni electrocatalysts, we have utilized DFT calculations to identify the chemical transformations that govern carbon poisoning of Ni. We found that the processes of C-C and C-O bond formation as well as carbon nucleation played an important role in the carbon-induced deactivation of the Ni catalysts. These insights led to the identification of the Ni surface alloys (i.e. Sn/Ni, Au/Ni…) as promising carbon tolerant catalysts.

Electrocatalysts containing Sn/Ni and Ni supported on YSZ were synthesized. Extensive characterization of electronic and geometric characteristics of the Sn/Ni electrocatalysts suggested the formation of a Sn/Ni surface alloy. The carbon tolerance of the Sn/Ni surface alloy and monometallic Ni was tested using packed-bed reactor

experiments and electrochemical SOFC studies. We found that the Sn/Ni surface alloy exhibited a significantly improved carbon tolerance compared to monometallic Ni in hydrocarbons steam reforming reactions and as SOFC anode electrocatalyst.

To advance our understanding of the chemistry that occurs on the Sn/Ni surface alloy, we have also performed detailed kinetic studies and isotope labeling experiments in combination with DFT calculations to identify the critical elementary steps that govern the performance of the Ni and Sn/Ni electrocatalysts. Furthermore, we have utilized electron microscopy and spectroscopy experiments to measure the electronic structure (i.e electronic states just above and below the Fermi Level) of the supported nonmodel catalysts (i.e. Ni and Ni alloys) and have related that to their chemical and catalytic performance. These detailed atomistic studies allowed us to derive a very general set of principles that allow us to identify novel carbon tolerant alloy catalysts for hydrocarbon reforming and electro-oxidation.

The work described in this dissertation presents a rare example where DFT calculations combined with various experimental techniques led to the bottom-up (based on molecular insights rather than on empirical trial and error testing) identification of improved electrocatalysts.

CHAPTER 1

GENERAL INTRODUCTION

1.1 Summary

This chapter gives an introduction to “rational” catalyst design as an effective approach toward the development of new and improved heterogeneous catalysts and electrocatalysts. The utility of this approach is demonstrated through the example of improving the long-term stability of steam reforming catalysts and on-cell reforming solid oxide fuel cells (SOFCs) anode electrocatalysts. We focus on carbon poisoning as a crucial problem in the long-term stability of the currently utilized Ni based steam reforming catalysts and on-cell reforming SOFC anode electrocatalysts when operating on hydrocarbon fuels. Therefore, it is imperative to develop carbon tolerant catalysts and electrocatalysts in order to improve the long-term stability of steam reforming processes and on-cell reforming SOFCs. In order to provide a background on the progress of research on the subject we discuss the main literature on the subject. We conclude by stating the scope of the thesis and providing a brief summary of each chapter included in this thesis.

1.2 Rational Catalyst Design

Traditionally, catalytic and electrocatalytic materials for most processes have been developed using "trial and error" experimental approaches. Although these approaches have led to major discoveries, they mainly rely on a combination of chemical intuition and extensive empirical observations. For example, the development of new catalysts typically requires running multiple reactions in parallel with materials that have different supports, different preparation methods, different amounts of active catalyst etc. The best combination of the support material, amount of metal loading and other variables is identified as the "optimal" catalyst.

Recently, with the advancements in the computational power and powerful experimental techniques, the idea of a "rational design" approach has emerged.[1] This approach, unlike the "trial and error" approaches, is based on a sufficient understanding of and control over the underlying elementary step chemistry that governs the outcome of a catalytic process. Recent theoretical and experimental advances have contributed significantly to the implementation of "rational design" in catalysis and electrocatalysis. These theoretical and experimental advancements include: 1) the development of powerful microscopy and spectroscopy techniques that have allowed us to study at the molecular level the chemical transformations that occur during a chemical process, [2-5] 2) the development of the density functional theory (DFT) methodology which has allowed us to obtain elementary step mechanisms, adsorption energies, vibrational spectra for adsorbates, transition states, stable geometries for adsorbates and substrates with high efficiency and accuracy[6-10] and 3) the advances in synthetic chemistry that

have allowed for the manipulation of materials at the nanoscale and even in some cases at the atomic scale[11-14].

There have been a few recent contributions that have shed light on the utility of the “rational design” as an effective approach toward the development of new or improved heterogeneous catalysts. For example, Norskov and coworkers have employed state of the art quantum chemical calculations to identify catalytic materials for various heterogeneous processes such as steam reforming and selective hydrogenation of acetylene, that are more robust than the existing catalysts.[15-17] Furthermore, the contributions of Linic at al. have also played an instrumental role in demonstrating the utility of “rational design” approach in developing selective catalysts for the process of ethylene epoxidation.[10, 18-21] This was demonstrated through a combination of quantum DFT calculations coupled with surface science experiments and reactor.

In this work, we have attempted to employ a “rational design” approach combining state of the art experimental and theoretical tools to improve the long-tem stability of steam reforming processes and on-cell reforming solid oxide fuel cell (SOFC) by identifying carbon tolerant catalysts and electrocatalysts. The work described herein is significant since it represents a rare example where advanced experimental and theoretical techniques can be concurrently utilized to systematically approach problems in heterogeneous catalysis and electrocatalysis.

1.3 Fuel Cell Technology

Conventional energy conversion systems, such as internal combustion engines, rely on the use of dwindling fossil fuel resources, contribute heavily to environmental pollutants, and are fairly inefficient. For example, the efficiency of an internal

combustion engine is ~30% (only 30% of the chemical energy of fuel is converted into useful energy). In addition, the combustion process produces high amounts of environmental pollutants such as NO_x. A promising alternative to the combustion processes relies on the direct electrochemical conversion of the chemical energy of combustible fuels into electricity using fuel cells. Fuel cells can achieve higher efficiencies and produce less environmental pollutants than the internal combustion system. [22] For example, the overall efficiency of the fuel cells can exceed 60% since they are not limited by the Carnot cycle (i.e. the conversion of the chemical energy of fuels to thermal energy to electrical energy - the process by which combustion engines operate).[22] Furthermore, these systems minimize the production of environmental pollutants such as NO_x.

Fuel cells are generally divided in two categories: low temperature fuel cells and high temperature fuel cells. Low temperature fuel cells such as polymer membrane fuel cells (PEMFC) operate at temperatures of less than 100°C. The main drawback with these systems is that they require pure hydrogen as a fuel and suffer from slow kinetics. [23] For example, hydrocarbon fuels undergo extensive reforming and CO removal before pure H_2 is obtained and supplied to the PEMFCs. On the other hand, high temperature fuel cells such as solid oxide fuel cells (SOFCs) which operate at temperatures 600-1000°C, can in principle facilitate the direct on-cell electrochemical conversion of any hydrocarbon fuel into electricity without the need of extensive external reforming. Aside from that, SOFCs also produce valuable exhaust heat that can be used to run other external processes.[22, 23] The proper utilization of the generated heat significantly improves their overall efficiency. The potential applications for SOFCs are

auxiliary and stationary power units. For example, the utilization of SOFCs as auxiliary power units (APUs) could result in a significant reduction in fuel cost, especially for the military.

1.4 Solid Oxide Fuel Cells

Solid Oxide Fuel Cells (SOFCs) are solid-state devices that convert the chemical energy of H_2, CO and hydrocarbons into electrical energy. SOFCs operate at temperatures between 600-1000°C. They consist of three compartments: an oxygen-ion-conducting electrolyte and two porous ceramic electrodes, the cathode and anode as shown in Figure 1.1. The anode has reforming ability and is electronically conductive, typically composed of nickel supported on yttria-stabilized zirconia (Ni-YSZ). The cathode is used to reduce the O_2 from air to O^{2-} ions. It is electronically conductive and typically composed of lanthanum strontium manganese oxide (LSM). The electrolyte is a solid ceramic material with high ionic conductivity and usually composed of dense yttria-stabilized zirconia (YSZ). In a SOFC, the cathode is usually exposed to air and the oxygen in the air is reduced to oxygen ions, see Figure 1.1. The oxygen ions diffuse through the electrolyte and react in the anode compartment with the fuel (i.e. H_2, CO and hydrocarbons) at the triple phase boundary region (TPB) – the region where the electrolyte, the anode and the fuel meet and the electrochemical reactions take place - forming H_2O, CO_2 and electrons. The electrons are exerted through an external circuit and re-circulated to the cathode where oxygen reduction continues to occur, while CO_2 and H_2O diffuse away from the TPB and out of the anode to the exhaust.

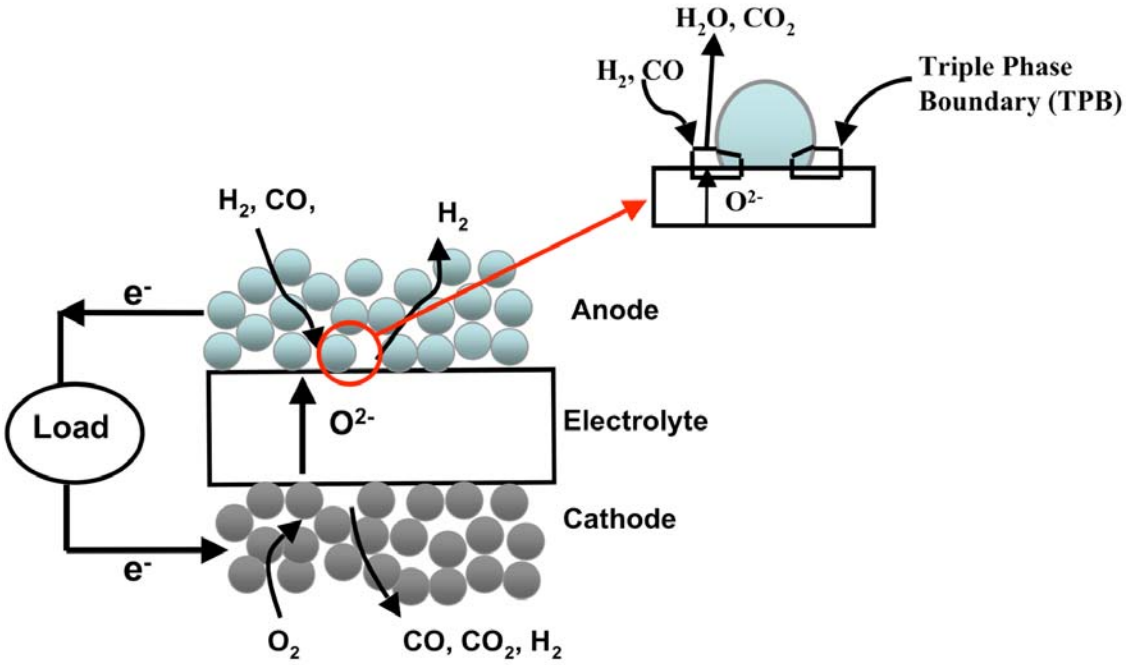

Figure 1.1. A schematic of an anode, electrolyte, cathode assembly of a SOFC. The image on the right is the schematic of the triple phase boundary (TPB) region.

In on-cell reforming SOFCs, as H_2O diffuses away from the TPB, it encounters the incoming fuel and it interacts with it via steam reforming. Therefore, steam reforming is an important component of the on-cell hydrocarbon reforming SOFCs.

The on-cell hydrocarbon reforming process in SOFCs is a complex interplay between the electrochemical oxidation and steam reforming processes. As a result, the anode (electro)catalyst has to facilitate both the electrochemical oxidation reactions at the TPB and the steam reforming reactions away from the TPB. Commonly used SOFC anode (electro)catalysts, such as Ni supported on YSZ can accommodate some of these functions. For example, under typical SOFC operating conditions, Ni is an excellent catalyst for the electrochemical oxidation of H_2 and CO and also a good steam reforming catalysts. One of the main problems with Ni based anodes is that they get poisoned by carbon deposits when exposed to hydrocarbons.[22, 24-27] Furthermore, Ni is also prone to sulfur poisoning when exposed to sulfur containing fuels. These problems have been an obstacle in the commercialization of on-cell reforming SOFCs. In this thesis, we will mainly focus on the problem of the carbon poising of Ni anodes and finding anode materials that are more carbon tolerant than Ni.

Steam reforming

As mentioned above, steam reforming is an important component in the direct on-cell reforming of hydrocarbon fuels using solid oxide fuel cells (SOFCs). Steam reforming is also the most employed process for hydrogen production. Furthermore, this process is also important since it produces a mixture of synthesis gas ($CO + H_2$) that can be utilized to produce valuable fuels and chemicals via the Fisher-Tropsch process.

Steam reforming is an endothermic reaction that involves the conversion of hydrocarbons and water into hydrogen and CO (rxn 1). In a catalytic reactor, this reaction is accompanied by the slightly exothermic water gas shift reaction (WGS) (rxn 2), which converts CO and steam into CO_2 and hydrogen.

$C_nH_m + nH_2O \Rightarrow nCO + (n + m/2)\ H_2 \quad (\Delta H_{298} > 0)$ rxn 1

$CO + H_2O \Leftrightarrow CO_2 + H_2 \quad (\Delta H_{298} = -41.2\ kJ/mol)$ rxn 2

Most traditional steam reforming catalysts contain Ni metal supported on an oxide.[28, 29] Ni is the preferred catalyst due to its high activity toward C-H bond cleavage and low cost. The oxide supports are utilized since they offer superior mechanical and thermal stability.[28] The mechanism of steam reforming has been studied for many years. It has been shown by both experiments and theory that the rate-limiting step in methane steam reforming on Ni catalysts is C-H bond activation.[8, 30-32] The main problem with Ni steam reforming catalysts as with Ni based SOFC anode (electro)catalysts is the deactivation due to carbon and sulfur poisoning when operating on hydrocarbon fuels. [33, 34]

1.5 Carbon Poisoning

The carbon-induced deactivation of Ni catalysts and (electro)catalysts has been an obstacle in the implementation of the on-cell reforming SOFCs and the long-term stability of steam reforming processes.[33, 34] To illustrate the problem of carbon poisoning, in Figure 1.2 we show images of a Ni/YSZ anode pellet before and after exposure to isooctane steam reforming at a steam to carbon ratio of 1.5 and an operating temperature of 1073 K.

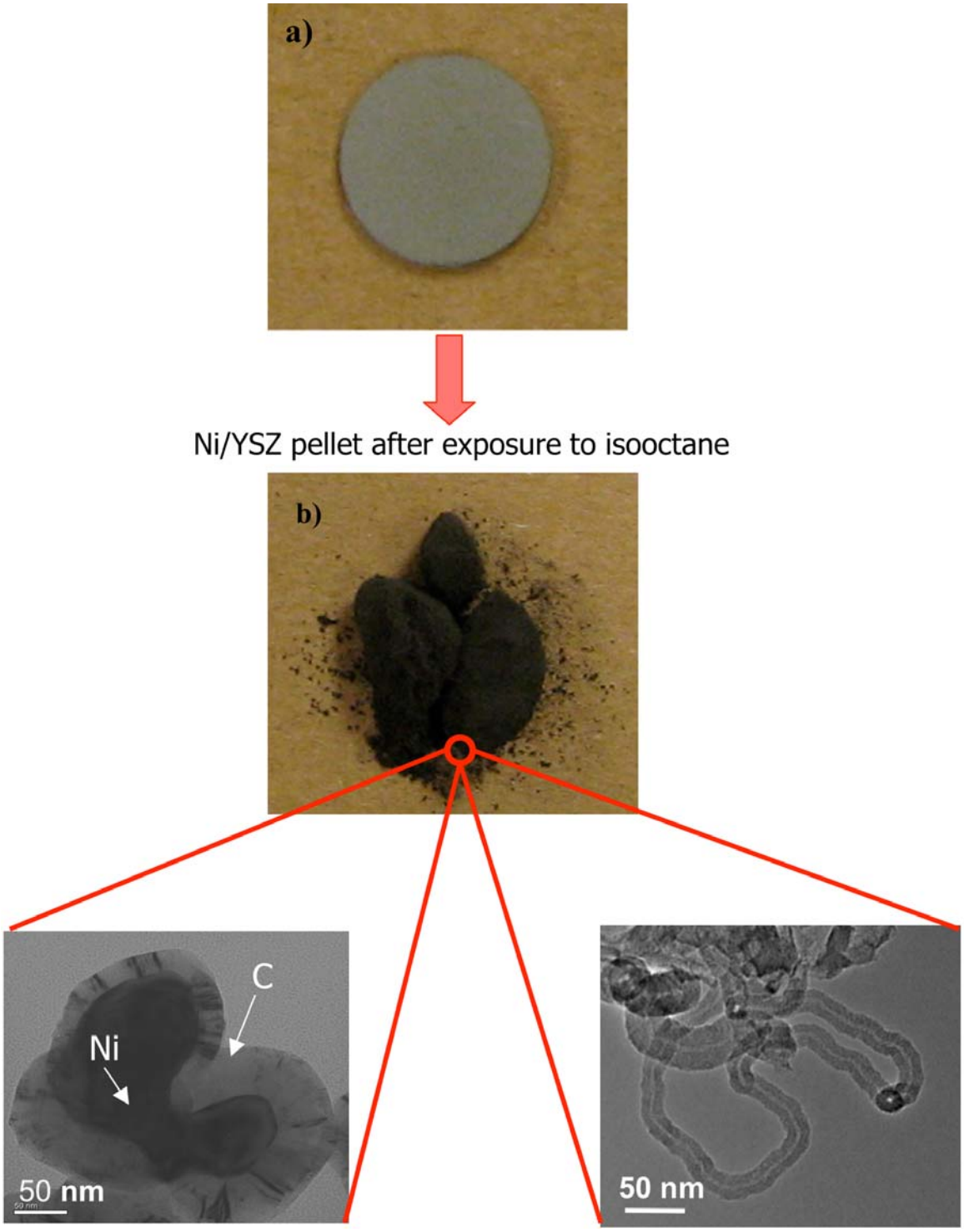

Figure 1.2. a) A fresh Ni/YSZ SOFC anode pellet b) The Ni/YSZ anode pellet after exposed to isooctane steam reforming c and d) transmission electron microscope (TEM) images of the carbon deposits of the catalysts covered by carbon deposits.

It is clear from Figure 1.2 b that the Ni/YSZ anode pellet has completely lost its structural integrity after exposure to isooctane due to the formation of carbon deposits. This is further supported by the transmission electron micrographs (TEM) of the carbon deposits formed on the Ni surface (see Figure 1.2 c and d). Carbon poisoning is a major problem in SOFCs because if the structural integrity of the anode is lost, then entire fuel cell is affected and the anode regeneration is not possible. This is even a problem in the case when an external reformer is coupled with a SOFCs. Any hydrocarbon fuel slippage (un-reformed fuel) from the reformer to the anode can lead to the deactivation of the anode due to carbon poisoning.

The problem of carbon poisoning has attracted a lot of attention over the years in both the steam reforming and solid oxide fuel cell arena. For example, Rostrup-Nielsen et al. have reported that steam reforming of various hydrocarbon liquid fuels on Ni leads to the formation of different carbon structures on the catalyst such as encapsulating, whisker-like, or pyrolytic carbon.[29, 33] The degradation of the Ni catalysts when exposed to hydrocarbon liquid fuels is rapid and in most cases leads to large pressure build-up in steam reforming reactors. The mechanism of the formation and growth of carbon deposits on Ni has also been investigated. For example, it has been demonstrated by *in-situ* TEM and DFT studies that during the decomposition of methane on $Ni/MgAl_2O_4$, carbon deposits are formed in a process that involves the diffusion of carbon atoms and fragments (created during fuel activation) on the Ni surface and their subsequent attachment to carbon nucleation centers.[35, 36] These studies also revealed that carbon nucleation commences on the under-coordinated surface sites of Ni.

Carbon-induced deactivation of Ni catalysts can be alleviated by increasing the concentration of steam in the feed stream.[29, 33] Steam enhances the rate of carbon oxidation thus leading to carbon removal in the form of CO or CO_2. However, the increase in the S/C (steam-to-carbon) ratio introduces a number of operational problems. For example, the addition of steam increases the flow rate through the reformer therefore escalating the size and capital cost of the equipment. In addition, substation energy is required to vaporize water and increase its temperature to the operating conditions of the reactor. Also, the need for additional steam lowers the flexibility to manipulate the CO/H_2 ratio in the effluent stream via the water gas-shift reaction. In SOFCs, the addition of steam lowers the energy density of the fuel stream.

Rather than increasing the operating S/C ratio, it is more beneficial to develop catalysts and SOFC anode (electro)catalysts that are inherently more carbon-tolerant than Ni. [14, 15, 22, 37-41] For example, it has been suggested that Ru and Rh might be promising steam reforming catalysts since they do not facilitate the formation of carbon deposits due to poor carbon solubility in these metals. However, Ru and Rh are prohibitively expensive. It has also been shown that the promotion of Ni steam reforming catalysts with alkaline earth metals such as Mg suppresses carbon-induced catalyst deactivation during steam reforming of heavy hydrocarbons.[29] There have also been reports that by selectively poisoning the low-coordinated Ni sites with small amounts of sulfur, the carbon-induced deactivation of Ni steam reforming catalysts can be suppressed. [8, 42]

Furthermore, Gorte and coworkers have shown that copper-ceria (electro)catalysts are promising carbon tolerant anodes for on-cell reforming SOFCs. In these systems,

copper primarily acts as an electron conductor since it has a poor capability to activate hydrocarbons.[22, 37, 43] In order to obtain reasonable performance for hydrocarbon electro-oxidation, ceria is incorporated. Ceria is know to be a good oxidation catalyst and has a good ionic conductivity. Bimetallic mixtures of Cu with Ni and Co were also considered in order to improve the reforming activity of copper and increase its meting temperature.[44] The main problem with the Cu-ceria systems is low thermal stability of copper and ceria. It has also been shown that by incorporating a catalyst layer of Ru-CeO_2 on top of the anode compartment (on the side that is exposed to the fuel) prevents carbon deactivation of the Ni SOFC anodes.[45-47] Barnett at al. found that Ru-CeO_2 catalyst layer acts as a reformer by breaking down the fuel to H_2 and CO prior to reaching the anode. The H_2 and CO is then electro-oxidized at the anode. This system has shown promising results when operating on isooctane but its thermal stability and fuel slippage to the anode still remains an issue.

Carbon poisoning in steam reforming processes and on-cell reforming SOFCs still remains a challenge. In this thesis, we have utilized "rational" catalyst designed based on the combination of experimental and theoretical tools to identify (electro)catalysts that are more carbon tolerant than Ni.

1.6 Scope of the thesis

The objective of this thesis is to obtain a fundamental understanding of the chemical transformations that govern the formation of extended carbon structures on Ni and to utilize this understanding to identify carbon tolerant catalysts and (electro)catalysts. We mainly focus on Ni alloys since they are fairly inexpensive, have good thermal properties and electrical conductivity. We have also utilized microscopic

and spectroscopic techniques in concert with DFT calculations to understand what governs the difference if any in the chemical performance between Ni and Ni alloys. We demonstrate how one can predict the chemical behavior or activity of these materials based on their experimentally measured electronic structure.

We employ a hybrid experimental/theoretical approach. In Chapter 2, a detailed description of the experimental and theoretical tools utilized to obtain the results presented in this thesis is provided. Density functional theory methodology was utilized to obtain reaction mechanisms and relevant steps that play a role in the formation of extended carbon structure that deactivate the catalyst. The relevance of the model systems utilized in these calculations is described in detail. On the experimental front, an arsenal of reactor studies, electrochemical testing techniques and microscopic and spectroscopic tools are utilized. A detailed description of each of these experimental techniques is included.

In Chapter 3, density functional theory calculations are utilized to study carbon chemistry on Ni surfaces and identify ways to prevent the formation of extended carbon structures. The DFT-calculated elementary step mechanism for steam reforming of methane on Ni (111) suggested that the two most thermodynamic stable states for the C on Ni are CO* and graphene (an extended carbon structure that leads to deactivates the catalyst). In order to prevent carbon poisoning, one has to identify materials that have lower rates of C-C bond formation and C-O bond formation and also hinder C nucleation on low coordinated sites. On Ni (111), the formation of CO and graphene are kinetically comparable so the rates of C-C bond formation are high. On the other hand, DFT calculations indicated that perturbing the Ni surface by alloying it with a foreign element

such as Sn favored C oxidation over C-C bond formation and also hinder nucleation of C on the low coordinated sites. We were able to synthesize a Sn/Ni surface alloy and show as predicted from DFT calculations, that it is a more carbon tolerant than monometallic Ni under steam reforming conditions.

In Chapter 4, performance tests for the Sn/Ni surface alloy versus monometallic Ni for various catalyst particle sizes and Ni loadings are reported. We show that the Sn/Ni surface alloy is a more carbon tolerant catalyst than monometallic Ni irrespective of the catalytic particle size or the Ni metal loading. This was established through extensive characterization of the catalysts before and after exposure to the steam reforming of various hydrocarbon fuels. A detailed characterization of the Sn/Ni surface alloy formation is also included.

In Chapter 5, a thorough electrochemical analysis of the potential of the Sn/Ni surface alloy as a SOFC anode is reported. The Sn/Ni anode and Ni anode solid oxide fuel cells were tested under constant voltage or constant current when operating on isooctane as a fuel. The results showed that the Ni anode SOFCs deactivated within a few hours of operation while the Sn/Ni anode SOFC was stable for as long as it was kept on stream. We also utilized scanning electron microscopy to characterize the fuel cell after operation. SEM showed that the Ni anode SOFCs were completely covered by carbon while no carbon deposits were detected on the Sn/Ni anode SOFCs. These results provide promising evidence that the Sn/Ni anode SOFCs can operate with hydrocarbon fuels without being deactivated.

In Chapter 7, electron loss near-edge spectroscopy (ELNES) and Auger electron spectroscopy (AES) were utilized to measure the electronic structure of the Ni surface

alloys. The measured electronic structure is related to the performance of these materials using the Hammer and Norskov d-band theory. We found that surface-alloying Ni with metals such as Sn broadened the d-band of the Ni atoms due to the hybridization of the Ni d states with the Sn s and p states, while preserving the total charge in the system. Broadening of the Ni d-band and the preservation of the charge resulted in the lowering of the d-band center of Ni. Since the chemistry occurs mainly on the Ni sites, due to the lowering of the d band center of Ni, we predicted based on the d-band theory that the Sn/Ni surface alloy would interact weaker with any adsorbates than the monometallic Ni catalyst. These predictions were supported by multiple experimental results that are outlined in detail in the chapter.

In Chapter 8, the approach utilized in the prior chapters to identify the Sn/Ni as a promising carbon tolerant catalyst was applied to other Ni surface alloys. We predicted based on DFT calculations that the Au/Ni and Ag/Ni surface alloys are also promising carbon tolerant catalysts. These predictions were supported by isooctane steam reforming studies on these various systems.

The major conclusions derived from the work presented in this thesis are stated in Chapter 9. An assessment of how this work has impacted the field of heterogeneous catalysis is included. Furthermore, a detailed description of the future direction of this work is also outlined.

1.7 References

1. Ertl, G., J. Knozinger, and J. Weitkamp, *Handbook of heterogeneous catalysis.* Vol. 5. 1997.

2. Chua, Y.T., P.C. Stair, and I.E. Wachs, *A comparison of ultraviolet and visible Raman spectra of supported metal oxide catalysts.* Journal of Physical Chemistry B, 2001. 105(36): p. 8600-8606.

3. Muller, D.A. and M.J. Mills, *Electron microscopy: probing the atomic structure and chemistry of grain boundaries, interfaces and defects.* Materials Science and Engineering A-Structural Materials Properties Microstructure and Processing, 1999. 260(1-2): p. 12-28.

4. Muller, D.A., P.E. Batson, and J. Silcox, *Measurement and models of electron-energy-loss spectroscopy core-level shifts in nickel aluminum intermetallics.* Physical Review B, 1998. 58(18): p. 11970-11981.

5. Teschner, D., Borsodi, J., Wootsch, A., Revay, Z ., Havecker, M., Knop-Gericke, A., Jackson, S.D., Schlogl, R., *The roles of subsurface carbon and hydrogen in palladium-catalyzed alkyne hydrogenation.* Science, 2008. 320(5872): p. 86-89.

6. Hohenberg, P. and W. Kohn, *Inhomogeneous Electron Gas.* Physical Review B, 1964. 136(3B).

7. Reuter, K. and M. Scheffler, *First-principles atomistic thermodynamics for oxidation catalysis: Surface phase diagrams and catalytically interesting regions.* Physical Review Letters, 2003. 90(4).

8. Abild-Pedersen, F., Lytken, O., Engbaek, J., Nielsen, G., Chorkendorff, I., Norskov, J. K., *Methane activation on Ni(111): Effects of poisons and step defects.* Surface Science, 2005. 590(2-3): p. 127-137.

9. Bengaard, H.S., Norskov, J. K., Sehested, J., Clausen, B. S., Nielsen, L. P., Molenbroek, A. M., Rostrup-Nielsen, J. R., *Steam reforming and graphite formation on Ni catalysts.* Journal of Catalysis, 2002. 209(2): p. 365-384.

10. Linic, S., J. Jankowiak, and M.A. Barteau, *Selectivity driven design of bimetallic ethylene epoxidation catalysts from first principles (vol 224, pg 489, 2004).* Journal of Catalysis, 2004. 226(1): p. 245-246.

11. Si, R. and M. Flytzani-Stephanopoulos, *Shape and crystal-plane effects of nanoscale ceria on the activity of Au-CeO_2 catalysts for the water-gas shift reaction.* Angew Chem Int Ed Engl, 2008. 47(15): p. 2884.

12. Sun, Y.G. and Y.N. Xia, *Shape-controlled synthesis of gold and silver nanoparticles.* Science, 2002. 298(5601): p. 2176-2179.

13. Sun, Y.G. and Y.N. Xia, *Large-scale synthesis of uniform silver nanowires through a soft, self-seeding, polyol process.* Advanced Materials, 2002. 14(11): p. 833-837.

14. Nikolla, E., Holewinski, A., Schwank, J., Linic, S., *Controlling carbon surface chemistry by alloying: Carbon tolerant reforming catalyst.* Journal of the American Chemical Society, 2006. 128(35): p. 11354-11355.

15. Besenbacher, F., Chorkendorff, I., Clausen, B. S., Hammer, B., Molenbroek, A. M., Norskov, J. K., Stensgaard, I., *Design of a surface alloy catalyst for steam reforming.* Science, 1998. 279(5358): p. 1913-1915.

16. Studt, F., Abild-Pedersen, F., Bligaard, T., Sorensen, R. Z., Christensen, C. H., Norskov, J. K., *Identification of non-precious metal alloy catalysts for selective hydrogenation of acetylene.* Science, 2008. 320(5881): p. 1320-1322.

17. Vang, R.T., Honkala, K., Dahl, S., Vestergaard, E. K., Schnadt, J., Laegsgaard, E., Clausen, B. S., Norskov, J. K., Besenbacher, F. *Controlling the catalytic bond-breaking selectivity of Ni surfaces by step blocking.* Nature Materials, 2005. 4(2): p. 160-162.

18. Linic, S. and M.A. Barteau, *On the mechanism of Cs promotion in ethylene epoxidation on Ag.* Journal of the American Chemical Society, 2004. 126(26): p. 8086-8087.

19. Linic, S. and M.A. Barteau, *Formation of a stable surface oxametallacycle that produces ethylene oxide.* Journal of the American Chemical Society, 2002. 124(2): p. 310-317.

20. Linic, S. and M.A. Barteau, *Control of ethylene epoxidation selectivity by surface oxametallacycles.* Journal of the American Chemical Society, 2003. 125(14): p. 4034-4035.

21. Linic, S., Piao, H., Adib, K., Barteau, M. A., *Ethylene epoxidation on Ag: Identification of the crucial surface intermediate by experimental and theoretical investigation of its electronic structure.* Angewandte Chemie-International Edition, 2004. 43(22): p. 2918-2921.

22. Atkinson, A., Barnett, S., Gorte, R. J., Irvine, J. T. S., Mcevoy, A. J., Mogensen, M., Singhal, S. C., Vohs, J., *Advanced anodes for high-temperature fuel cells.* Nature Materials, 2004. 3(1): p. 17-27.

23. Mogensen, M. and K. Kammer, *Conversion of hydrocarbons in solid oxide fuel cells.* Annual Review of Materials Research, 2003. 33: p. 321-331.

24. Timmermann, H., et al., *Internal reforming of methane at Ni/YSZ and Ni/CGO SOFC cermet anodes.* Fuel Cells, 2006. 6(3-4): p. 307-313.

25. Lashtabeg, A. and S.J. Skinner, *Solid oxide fuel cells - a challenge for materials chemists?* Journal of Materials Chemistry, 2006. 16(31): p. 3161-3170.

26. Finnerty, C.M., et al., *Carbon formation on and deactivation of nickel-based/zirconia anodes in solid oxide fuel cells running on methane.* Catalysis Today, 1998. 46(2-3): p. 137-145.

27. Triantafyllopoulos, N.C. and S.G. Neophytides, *The nature and binding strength of carbon adspecies formed during the equilibrium dissociative adsorption of CH_4 on Ni-YSZ cermet catalysts.* Journal of Catalysis, 2003. 217(2): p. 324-333.

28. Rostrup-Nielsen, J.R., *Catalytic Steam Reforming*, in *Catalysis - Science and Technology*. 1984, Springer: Berlin.

29. Rostrup-Nielsen, J.R., J. Sehested, and J.K. Norskov, *Hydrogen and synthesis gas by steam- and CO_2 reforming.* Advances in Catalysis, Vol 47, 2002. 47: p. 65-139.

30. Achenbach, E. and E. Riensche, *Methane Steam Reforming Kinetics for Solid Oxide Fuel-Cells.* Journal of Power Sources, 1994. 52(2): p. 283-288.

31. Watwe, R.M., et al., *Theoretical studies of stability and reactivity of CHx species on Ni(111).* Journal of Catalysis, 2000. 189(1): p. 16-30.

32. Wei, J.M. and E. Iglesia, *Isotopic and kinetic assessment of the mechanism of reactions of CH_4 with CO_2 or H_2O to form synthesis gas and carbon on nickel catalysts.* Journal of Catalysis, 2004. 224(2): p. 370-383.

33. Rostrup-Nielsen, J.R., T.S. Christensen, and I. Dybkjaer, *Steam reforming of liquid hydrocarbons.* Recent Advances in Basic and Applied Aspects of Industrial Catalysis, 1998. 113: p. 81-95.

34. Rostrup-Nielsen, J.R. and L.J. Christiansen, *Internal Steam Reforming in Fuel-Cells and Alkali Poisoning.* Applied Catalysis A-General, 1995. 126(2): p. 381-390.

35. Abild-Pedersen, F., et al., *Mechanisms for catalytic carbon nanofiber growth studied by ab initio density functional theory calculations.* Physical Review B, 2006. 73(11).

36. Helveg, S., et al., *Atomic-scale imaging of carbon nanofiber growth.* Nature, 2004. 427(6973): p. 426-429.

37. Gorte, R.J. and J.M. Vohs, *Novel SOFC anodes for the direct electrochemical oxidation of hydrocarbons.* Journal of Catalysis, 2003. 216(1-2): p. 477-486.

38. Nikolla, E., J. Schwank, and S. Linic, *Promotion of the long-term stability of reforming Ni catalysts by surface alloying.* Journal of Catalysis, 2007. 250(1): p. 85-93.

39. Trimm, D.L., *Coke formation and minimisation during steam reforming reactions.* Catalysis Today, 1997. 37(3): p. 233-238.

40. Trimm, D.L., *Catalysts for the control of coking during steam reforming.* Catalysis Today, 1999. 49(1-3): p. 3-10.

41. Ul-Haque, I. and D.L. Trimm, *Process for steam reforming of hydrocarbons*, in *Ostrolenk, Faber, Gerb & Soffen, LLP*. 1997, Haldor Topsoe.

42. Rostrup-Nielsen, J.R., *Sulfur-Passivated Nickel-Catalysts for Carbon-Free Steam Reforming of Methane.* Journal of Catalysis, 1984. 85(1): p. 31-43.

43. Kim, H., et al., *Cu-Ni cermet anodes for direct oxidation of methane in solid-oxide fuel cells.* Journal of the Electrochemical Society, 2002. 149(3): p. A247-A250.

44. Lee, S.I., Vohs J.M., and Gorte R.J., *A study of SOFC anodes based on Cu-Ni and Cu-Co bimetallics in CeO_2-YSZ.* Journal of the Electrochemical Society, 2004. 151(9): p. A1319-A1323.

45. Murray, E.P., et al., *Direct solid oxide fuel cell operation using isooctane.* Electrochemical and Solid State Letters, 2006. 9(6): p. A292-A294.

46. Zhan, Z.L. and S.A. Barnett, *An octane-fueled solid oxide fuel cell.* Science, 2005. 308(5723): p. 844-847.

47. Zhan, Z.L. and S.A. Barnett, *Use of a catalyst layer for propane partial oxidation in solid oxide fuel cells.* Solid State Ionics, 2005. 176(9-10): p. 871-879.

CHAPTER 2

EXPERIMENTAL AND THEORETICAL TECHNIQUES

2.1 Summary

A combined theoretical and experimental approach is employed throughout this thesis. In this chapter, a detailed description of the experimental (i.e. microscopies, spectroscopies, electrochemical and reactor testing) and theoretical techniques utilized in this work is provided. Aside from providing a detailed description of the experimental and theoretical procedure used, we also discuss the underlying principles that govern the operation of these techniques. Furthermore, we also describe the methods implemented to synthesize all the catalysts, electrocatalysts and solid oxide fuel cells (SOFCs).

2.2 Introduction

In this thesis, we have employed a combined experimental and theoretical approach. On the theoretical front, we have used density functional theory (DFT) calculations to study carbon chemistry on Ni and identify carbon tolerant catalysts and electrocatalysts. On the experimental side, an arsenal of microscopic and spectroscopic techniques along with reactor and electrochemical studies were employed to formulate, characterize, and test various catalysts, electrocatalysts, and solid oxide fuel cells.

Herein, we present experimental results obtained for various systems such as steam reforming catalysts, anode SOFC electrocatalysts and solid oxide button cells. All catalysts in these studies were composed of Ni and Ni alloys supported on 8 mol% yttria stabilized zirconia (YSZ). The main differences between the steam reforming catalysts and anode SOFC electrocatalysts were the Ni loading and particle size. SOFC anode electrocatalysts contained 44 wt% of Ni metal with respect to the total catalyst weight (Ni plus YSZ) and approximately 0.5 μm diameter Ni particles. The high Ni loading was necessary to obtain good electron conductivity. On the other hand, steam reforming catalysts contained ~15 wt% of Ni loading with respect to the total weight of the catalyst and an average Ni particle size from 30 to 50 nm. Furthermore, we have also synthesized and tested planar anode-supported solid oxide fuel cells (SOFCs). The anode-supported SOFCs are characterized by a thick anode compartment (0.5-1mm) that supports both the electrolyte and cathode.[1-3] A detailed description of the preparation procedure for the catalysts, electrocatalysts and solid oxide fuel cells is provided below. This is followed by the description of the experimental and theoretical techniques.

2.3 Synthesis Techniques

2.3.1 Catalyst Preparation

The support, yttria-stabilized zirconia (8 mol %) was prepared via a co-precipitation method. A mixture of yttrium nitrate ($Y(NO_3)_3*6H_2O$) and zirconyl chloride ($ZrOCl_2*2H_2O$) in deionized water was precipitated using a solution of ammonium hydroxide. After filtration and drying over night, the precipitate was calcined at 1073 K for 2 hours.

We have synthesized steam-reforming catalysts, SOFC anode electrocatalysts and anode supported SOFC composed of Ni and Ni alloys supported on YSZ as illustrated in Figure 2.1.

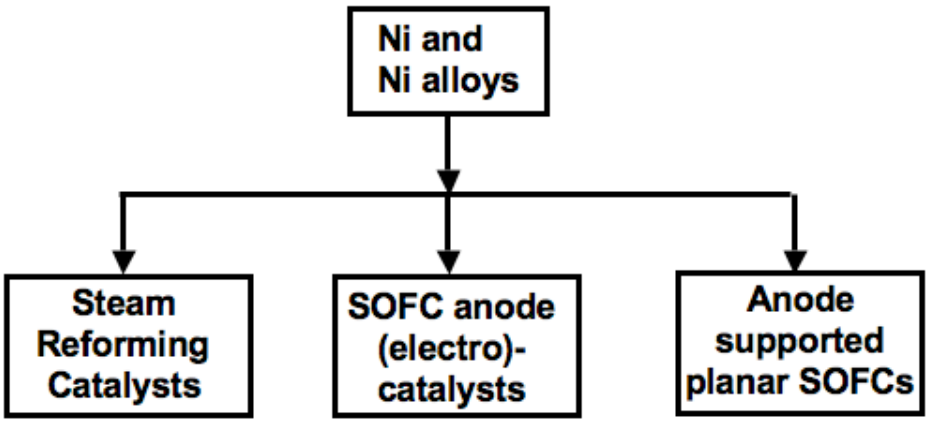

Figure 2.1 A schematic of the materials and fuel cells synthesized in this thesis

The steam reforming catalysts were prepared using the incipient wetness method.[4] This method involves the impregnation of the support with a metal-containing solution. This solution is prepared by dissolving a metal precursor in a solvent. Capillary action draws the metal containing solution into the pores of the support. The solvent is removed by heating the material after impregnations. This method results in metal

particles that are well dispersed onto the support. In our work, the metal containing solution was composed of an equivalent of ~ 15 %wt of Ni with respect to the total amount of catalyst (Ni plus YSZ) in the form of $Ni(NiO_3)_3$ dissolved in ethanol. The solution was sequentially impregnated onto the YSZ support. The material was heated to 373 K to remove the solvent after each impregnation step. After all the $Ni(NiO_3)_3$ in ethanol solution was exhausted the material was calcined in air at 873 K for 2 hours. This was followed by the reduction of the catalysts using a gas mixture of 30 % H_2/N_2 at 1073 K for 5 hours. This preparation procedure resulted in metal particles of 30 to 50 nm in diameter dispersed on the support. The Ni alloy/YSZ steam reforming catalysts were prepared by impregnating ~ 1-3 wt % of alloy element (Sn, Ag or Au), with respect to Ni on the calcined NiO/YSZ sample. The catalyst samples were then calcined at 873 K for 2 hours and reduced under a stream of 30 % H_2/N_2 for 5 hours at 1073 K.

SOFC anode electrocatalysts were prepared by ball milling a mixture of 50 wt% YSZ and 50 wt% of NiO in methanol for 24 hours. Once dried, the powder was pressed into 13 mm diameter pellets at 5000 psi. The pellets were sintered at 1673 K for 4 hours and further reduced at 1173 K for 5 hours in a gas mixture of 30 % H_2/N_2. This synthesis procedure yielded catalytic particles with ~ 0.5 μm diameter, as measured by TEM. The resulting catalysts had a Ni metal loading of 44 wt%. The Ni alloy/YSZ SOFC anode electrocatalysts was prepared by impregnating alloy metal precursors (~ 1 wt% of metal with respect to Ni) on the sintered NiO/YSZ pellets via the incipient wetness technique. The pellets were dried overnight at 473 K and then reduced under a stream of 30 % H_2/N_2 for 5 hours at 1173 K.

2.3.2 Solid Oxide Button Cell Preparation

The anode supported solid oxide button cells were approximately 1 inch in diameter and 1 mm thick. The anode was prepared by ball milling 50/50% by weight of NiO (Alfa Aesar), YSZ (co-precipitation), and the pore former (graphite) in ethanol for 24 hours.[5] The mixture was dried and pressed into 1-inch diameter pellets. This was followed by the annealing of the anode pellets at 1273 K for 5 hours. The electrolyte layer was prepared by drop coating YSZ dissolved in ethanol on one side of the anode pellet. The pellets were then sintered at 1773 K for 5 hours to obtain the desired density of the electrolyte. The cathode was prepared by ball milling 50:50 by weight of LSM ($La_{0.85}Sr_{0.15}MnO_3$)(Praxair) and YSZ in ethanol. The mixture was then applied on top of the electrolyte via paint coating. In order to obtain the appropriate microstructure of the cathode the fuel cells were annealed at 1423 K for 5 hours.

2.4 Microscopic and Spectroscopic Techniques

Multiple spectroscopic and microscopic techniques were implemented to characterize the catalysts, electrocatalysts and solid oxide fuel cells before and after exposure to reforming and electrochemical conditions. Table 2.1 shows a list of the various techniques used in this thesis and the characteristic features of each technique. This is followed by a detailed description of the unique features of each technique and the procedure followed to

Table 2.1. A list of various spectroscopic and microscopic techniques used for the work presented in this thesis.

Techniques	Features
X-ray Diffraction	Measures the bulk chemical composition and crystallite size of materials.
Scanning electron microscopy (SEM)	Measures the surface topography of a material.
X-ray Photoelectron spectroscopy (XPS)	Measures the surface elemental composition and chemical state of the elements of materials (1-10nm).
Auger electron microscopy (AES)	Measures the surface composition and electronic structure (below the Fermi Level) of materials.
Scanning transmission electron microscopy (STEM)	Provides high resolution images of materials.
Energy Dispersive X-ray Spectroscopy (EDS)	Measures the elemental composition of materials.
Electron Energy Loss Spectroscopy (EELS)	Measures the chemical composition and the electronic structure (above the Fermi level) of materials

2.4.1 X-Ray Diffraction (XRD)

X-ray diffraction is a technique utilized to determine the crystallographic structure and chemical composition of a material. In these experiments, x-rays are emitted from an x-ray source to the sample. Due to the interaction with the sample the x-rays undergo elastic scattering with a certain incident or scattering angle, which is unique for a particular crystallographic structure. In XRD experiments, a spectrum of the scattering intensity as a function of the incident or scattering angle is obtained. The XRD spectrum also contains information about the composition of materials. Since the x-rays undergo elastic scatterings, which have long-range order, XRD mainly probes the bulk of the sample. Furthermore, the XRD spectrum can also be utilized to obtain the mean crystallize size of the material via the Scherrer equation (eqn 1). This equation relates the crystallite size to the breadth peak of a specific phase of the material as shown in equation 1.[6]

$$d_c = \frac{0.9\lambda}{\beta \cos\theta} \qquad \text{eqn 1}$$

where d_c is the diameter of the crystallite, β is the breadth of the diffraction peak, λ is the wavelength of the incident x-rays, θ is the angle of the diffraction peak.

The XRD measurements were conducted with a Cu-Kα source using a Philips XRG5000 3 kW x-ray generator with crystal alignment stage and a Rigaku thin film camera. The spectrum was analyzed using Jade v.7 software, which allowed us to assign the measured spectra to concrete structures. For example Figure 2.2 shows a typical XRD spectrum that we obtain for our measurements. The peaks of the spectrum can be identified using the Jade program.

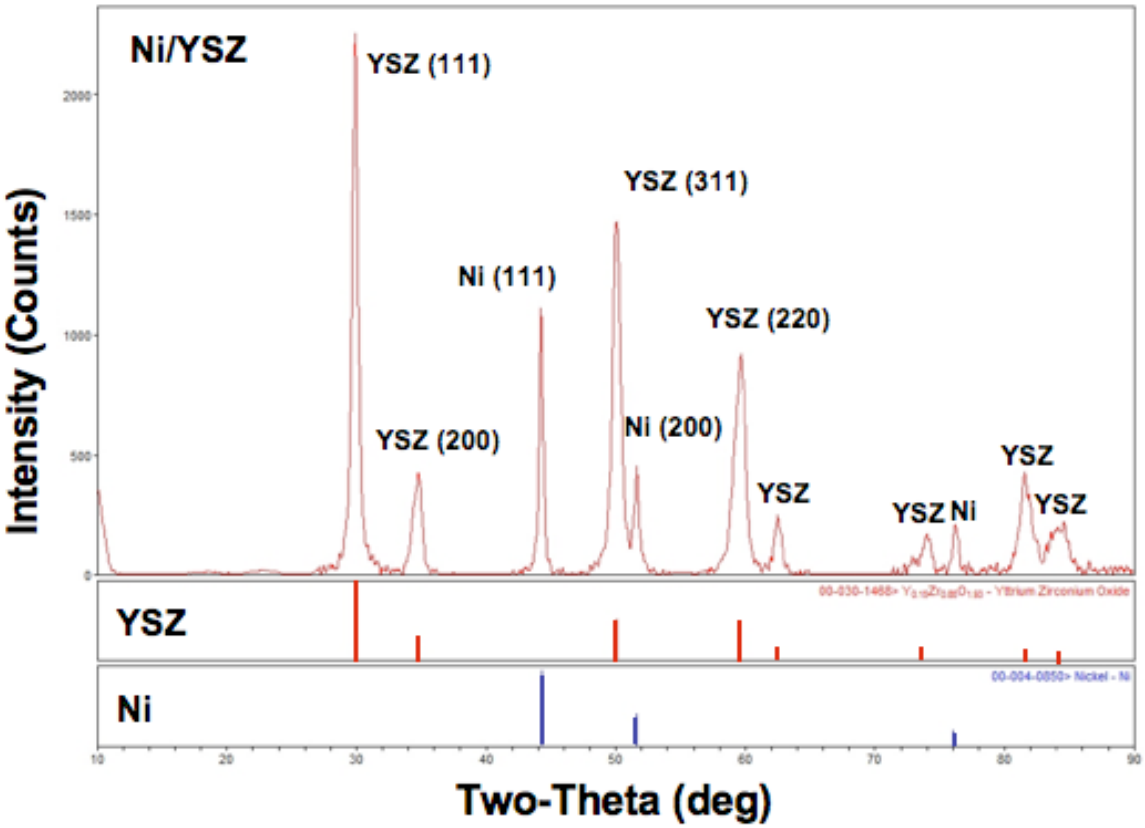

Figure 2.2. The upper graph shows the XRD spectrum obtained for a powder Ni/YSZ catalyst. The middle line graph shows the standard YSZ spectrum obtained from Jade. The bottom line graph shows the standard spectrum for Ni obtained from Jade.

Jade contains a large database of XRD spectra for various materials and matches the peaks in the unknown spectrum to the ones in its database. This is demonstrated by the two bottom line graphs in Figure 2.2. The peaks pertaining to YSZ and Ni are separately identified based on the matches that are found on the database.

2.4.2 Scanning electron microscopy (SEM)

SEM is a technique that utilizes a high electron beam to obtain the surface topography of materials. The electron beam interacts with the material generating various signals such as secondary electrons (electrons from the surface atoms of the material which get ejected due to the interaction with the electron beam), backscattered electrons (electrons from the beam that have undergone interaction with the nuclei of the atoms in the sample), characteristic x-rays and so on. In this work we have mainly utilized the secondary electron scattering signal to analyze the topography of the surface of the materials. The secondary electrons have low energies of around 50eV and provide a topographic contrast from the surface of the material.[7, 8]

In the studies presented herein, we have utilized the Philips XL30 Environmental Scanning Electron Microscope (SEM) to obtain images of the fresh and used reforming catalysts and solid oxide fuel cells.[8] This microscope has a special resolution of a few nanometers and it is also equipped with an energy dispersive x-ray spectrometer (EDS). A more detailed description of the EDS technique is provided below.

2.4.3 X-ray Photoelectron Spectroscopy (XPS)

XPS is a technique utilized to measure the elemental composition and the chemical state of the elements present in a material. In XPS, the x-rays from an x-ray source are ejected into a sample. The x-rays interact with the sample exciting the

electrons from the core levels of the atoms to vacuum (see Figure 2.3). The escape depth of the electrons is between 1-10 nm, therefore XPS is considered to be a surface sensitive technique.

In XPS experiments, a plot of the intensity as a function of the binding energy of electrons is obtained. The binding energy of the core electrons in the sample can be approximated using equation 2.[9]

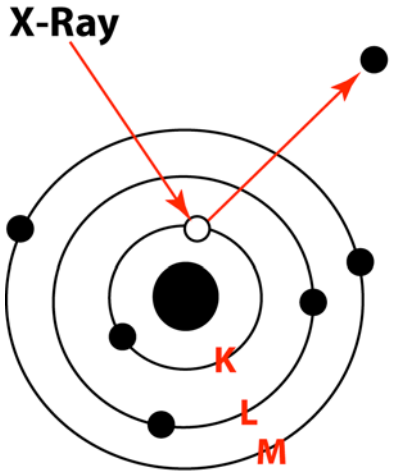

Figure 2.3. Schematic of the process that occurs in a x-ray photoelectron spectroscopy experiment

$$E_{binding} = E_{photon} - E_{kinetic} - \phi \qquad \text{eqn 2}$$

Where $E_{binding}$ is the binding energy of the excited electrons in the core levels of the atoms in the sample, E_{photon} is the energy of the x-ray photons from the x-ray source, $E_{kinetic}$ is the kinetic energy of the electrons that are ejected from the core levels of the atoms in the sample to the vacuum as measured by the spectrometer, and ϕ is the work function of the spectrometer. The binding energy of the core electrons provides a unique electronic fingerprint of each element in the periodic table. Furthermore, any shifts in the binding energy of core electrons can be associated with the change in the chemical state

of the elements in the sample.[10, 11] For example, for Ni metal, the main XP peaks are $Ni_{2p}{}^{1/2}$ and $Ni_{2p}{}^{3/2}$. Ni_{2p} peaks are associated with the binding energy of electrons in the 2p states of Ni. If Ni is oxidized, then the Ni_{2p} peaks shift to a higher binding energy due to the interaction of the nickel atoms with the oxygen atoms.

The XPS experiments presented in this thesis were conducted using Kratos Axis Ultra XPS with 150W Al (Mono) X-ray gun. The instrument is operated under a pressure of $5*10^{-9}$ torr. The samples were pre-reduced in a reaction chamber connected to the XPS to avoid any oxidation of the samples due to the exposure to air. The runs were conducted using pass energy of 20 eV and 10eV. The charge neutralizer was utilized to prevent sample charging. The instrument was calibrated with respect to Au $4f_{7/2}$ at 84 eV.

2.4.4 Auger Electron Spectroscopy (AES)

Auger electron spectroscopy is a surface sensitive technique utilized to determine the composition of the surface layers of a sample.[12, 13] This technique is based on the Auger effect. The Auger effect is a consequence of the creation of a hole in the core states of an atom in the sample due to interaction of the sample with x-ray or an electron beam, which ejects electrons from core states to vacuum. The empty core hole is filled by an electron from the valance energy levels of the atom. The transition of an electron from a higher energy level to a lower energy level results in the release of energy that is transferred to a second electron in the valance band, which gets ejected to the vacuum. The schematic of the Auger process is shown in Figure 2.4 below. The kinetic energy of the Auger electron (the second valance electron that is ejected from the valance state to the vacuum) can be approximated using equation 3.

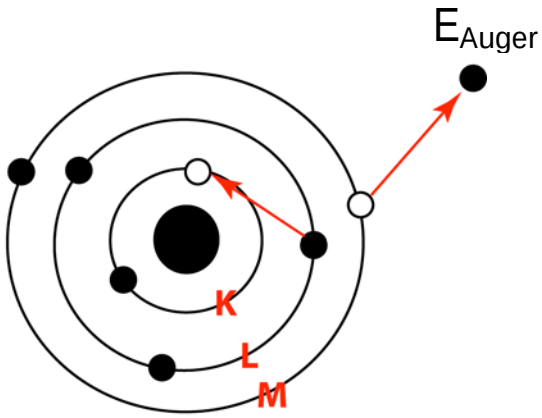

Figure 2.4. Schematic of Auger effect that occurs in the Auger Electron Spectroscopy (AES) experiment.

$$E_K = E_C - (E_{v1} + E_{v2}) - U \qquad \text{eqn 3}$$

where E_k is the measured kinetic energy of the Auger electron that is ejected from the valance levels to the vacuum, E_c is the binding energy associated with the core hole, E_{v1} is the binding energy associated with the first valance hole, E_{v2} is the binding energy associated with the second valance hole, and U is the interaction energy between the two holes created in the valance bands. The value U plays an important role in the shape of the Auger spectrum. For example, for large values of U (when U is much larger than the width of the valance band) the Auger spectrum looks like a localized atomic state due to the strong interaction between the holes.[13] On the other hand, when U is approximately the same or smaller in magnitude than the bandwidth, as in the case of Ni, the Auger spectrum looks very similar in shape to the valance band. In this case AES can be very useful in analyzing the valance electronic structure of materials.

In this thesis, the AES experiments were conducted in the XPS chamber. The experimental procedure is similar to the one described above for the XPS experiments.

2.4.5 Scanning Transmission Electron Microscopy (STEM) and Transmission Electron Microscopy (TEM)

The STEM and TEM are electron microscopes utilized to obtain high-resolution images of materials.[14, 15] The electron microscope works very similar to a light microscope but instead of the light, it uses electrons as a source. Since electrons have a much lower wavelength than light, the resolution of the electron microscope is much higher than that of a light microscope. An electron microscope is equipped with a number of electro-optical components, which focus and magnify the electron beam. In TEM, a broad electron beam is generated from an electron source consisting of a filament, which is typically tungsten or a ceramic material.[7] The electron beam is transmitted through the sample and is focused and magnified using an objective, projector lens respectively as shown in Figure 2.5. The electrons then hit a fluorescence screen which gives rise to a "shadow image" of the sample based on the density of these electrons. One of the differences between the TEM and STEM is the size of the electron beam. In TEM a broad electron beam is utilized, while in the STEM the electron beam is focused by electron optics in a small probe size and is allowed to move and scan the sample. Therefore in STEM a series of images of the samples are collected for each point that is probed with the electro beam. This technique is very useful when coupled with energy dispersive x-ray spectroscopy (EDS) and electron energy loss spectroscopy (EELS) since the focused beam allows for line scanning and provides very high spatial resolution.

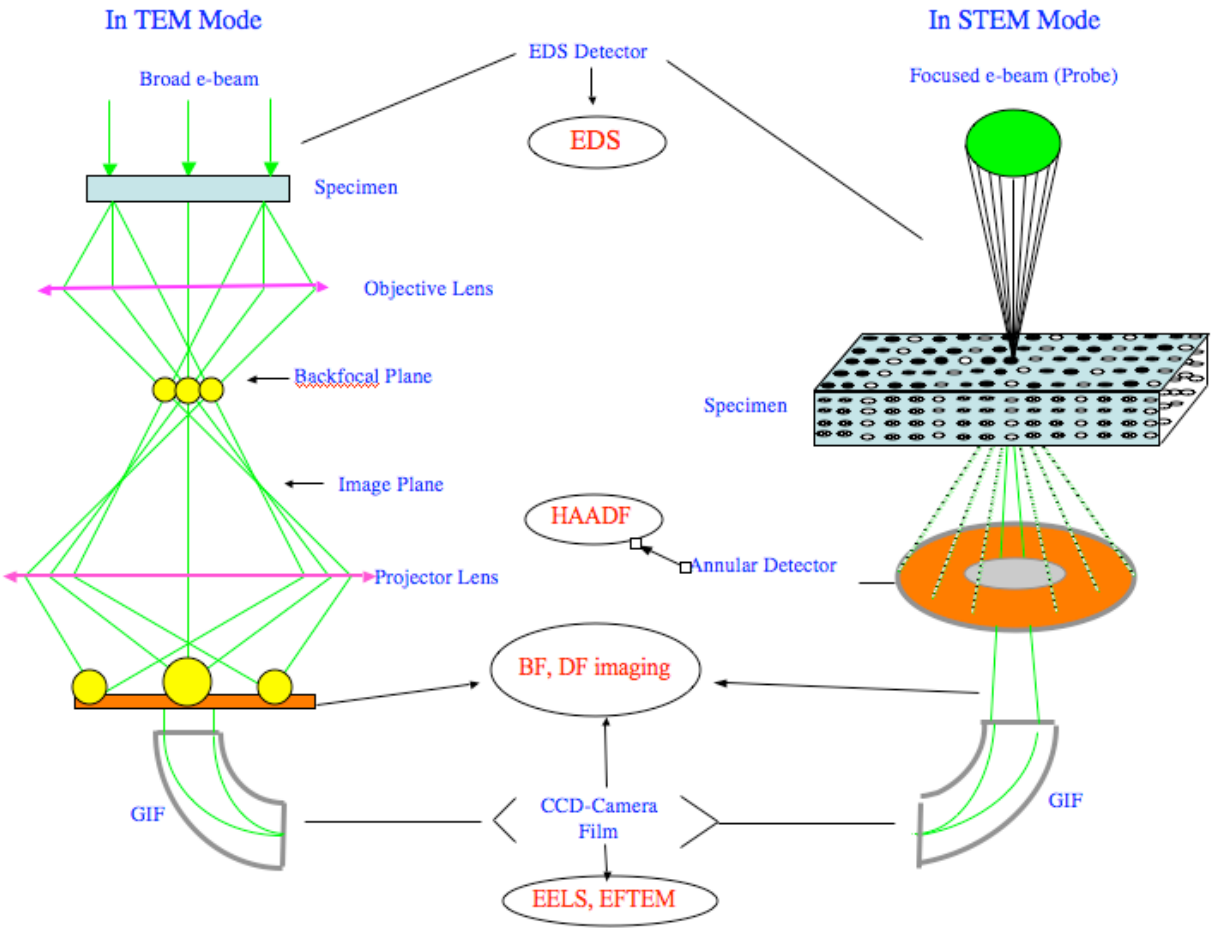

Figure 2.5. Schematic of the basic components in TEM and STEM [15].

The results reported in this thesis were obtained using the Joel 2010F electron microscope. This instrument can operate in both the STEM and TEM mode. It operates at 200 keV under a pressure of $1.5 * 10^{-7}$ torr. The instrument is equipped with a zirconated tungsten (100) thermal field emission tip filament. The samples utilized in the TEM and STEM studies were prepared by dispersing the powder catalyst on holey carbon-coated copper grids.

2.4.6 Energy Dispersive X-ray Spectroscopy (EDS)

EDS is a spectroscopic technique utilized to identify the elemental composition of a material. In the EDS experiments, a sample interacts with an electron beam resulting in the excitation of electrons from the core levels to empty energy levels or the vacuum.[7] This process results in an empty electron state or hole, which is filled by another electron from a higher energy level. When the electron drops from the higher energy level to the core state, an x-ray photon with an energy equal to the difference in energy between the two excited states involved in the process is emitted (see Figure 2.6). The energy of the x-ray photon emitted is characteristic for each element in the periodic table. This is the basis for the EDS, which measures the energy of the emitted x-ray photon and identifies the elements present in the material based on these energies.

The EDS measurements were performed with the Ametec EDAX system, integrated in the Joel 2010F microscope, in spot and scanning modes. To obtain a reasonable current, the lens was set for a probe size of 0.5 nm. The elemental scanning images were obtained using 512 x 512 pixels in a frame at a dwell time of 200 microseconds. To minimize the effect of specimen drift, a drift correction mode was used

during the elemental mapping. For each sample we have analyzed several particles from several different areas.

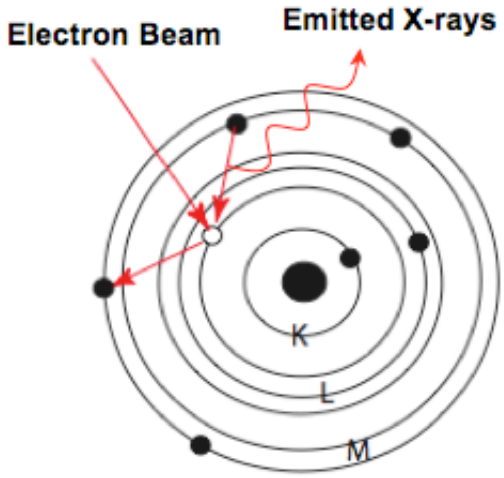

Figure 2.6. Schematic of process that occurs in energy dispersive x-ray spectroscopy (EDS)

2.4.7 Electron energy loss spectroscopy (EELS)

EELS is a technique utilized to analyze the electronic structure and chemical composition of materials.[7, 16-20] In EELS experiments, electrons from the inner or core shells of the atoms in the specimen are ejected from the core energy levels to the outer energy levels or the unoccupied states above the Fermi Level due to the interactions with the electron beam (see Figure 2.7). Ejection of the core electrons requires that these electrons receive an energy that is greater or equal to the ionization energy Ec that is uniquely defined for each specific atom and electron shell. This process generates characteristic signals mainly known as ionization edges that are unique for a specific atom and transition to specific shells. For example in the case of Ni, the electrons are ejected from the $2p^{1/2}$ and $2p^{3/2}$ core energy states to the 3d outer energy states, generating

L_2 and L_3 edges in the EELS spectrum respectively. The electronic information of the material is associated with small intensity fluctuations just above the ionization edge onset of the EELS spectra known as electron loss near edge structure (ELNES).[21] The technique utilized herein known as the electron energy loss near edge spectroscopy measures these near edge structures (ELNES). For metals, the ELNES can be directly associated with the unoccupied energy states above the Fermi Level of the exited atoms.

The EELS experiments were carried out in Joel 2010F field emission electron microscope. The instrument was operated at 200 kV under a pressure of $1.5 * 10^{-7}$ torr in scanning transmission electron mode (STEM). Gatan imaging filter (GIF) was utilized to collect the low-angle inelasticly scattered electrons to obtain the electron energy loss spectroscopy (EELS) spectra. EELS spectra was analyzed using Digital Micrograph. The lens conditions during operation were defined for a probe sized of about 0.2 nm, with a convergence angle of 13 mrad and a collection angle of 40 mrad. The energy resolution (defined by the full width at half maximum of the zero loss peak) of the energy loss spectra is 1.4 eV at a dispersion of 0.3eV per pixel.

The specimens for the electron microscope experiments were prepared by directly placing the pre-reduced catalyst powders on holey carbon-coated copper grids. Once inside of the electron microscope, the samples were heated to 773 K to eliminate any surface oxidation. Spectra were collected from the edge and the center of the several particles.

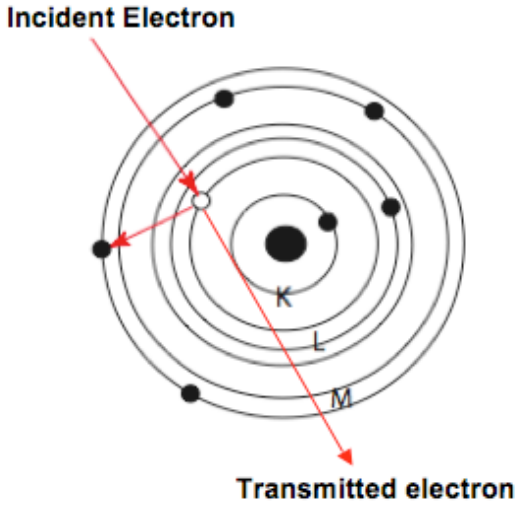

Figure 2.7. Schematic of process that occurs in electron energy loss spectroscopy (EELS)

2.4.8 Reactor Studies

2.4.8.1 Steam Reforming Stability Tests

Steam reforming stability tests were conducted isothermally at temperatures ranging from 923-1073 K in a packed bed reactor set-up.

The set-up included a set of mass flow controllers, a pair of thermocouples (inside in close contact with the catalyst bed and outside the reactor), and peristaltic pumps for liquid delivery (see Figure 2.8). Approximately 0.8 g of catalyst (metal plus support in form of powder and pellet) and a total inlet gas flow-rate of 1400 sccm were used, yielding a gas hourly space velocity (GHSV) of 50,000 hr^{-1}. The lines after the fuel pump inlet were heated to 473K to avoid condensation of the water and the liquid fuels. The reactor effluent was analyzed using a Varian gas chromatograph (Varian CP 3800) equipped with thermal conductivity detectors.

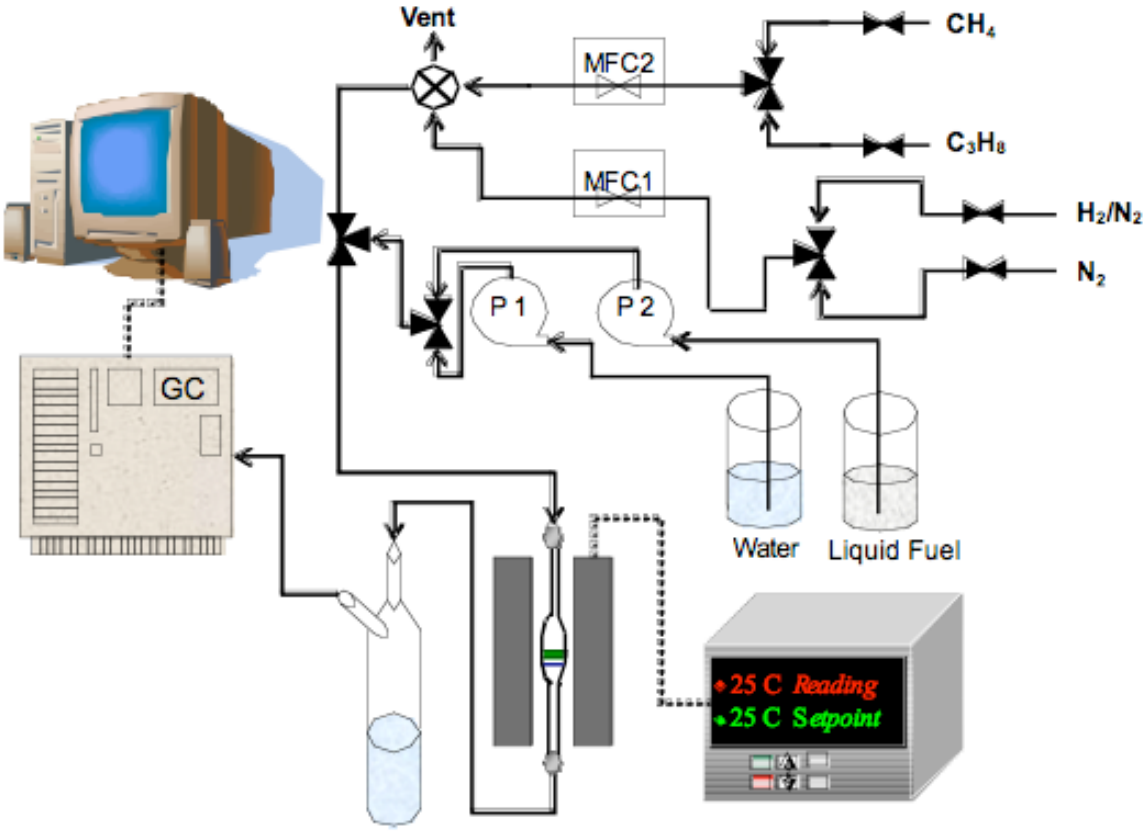

Figure 2.8. Schematic of reactor set-up utilized to run the steady state reactor experiments.

2.4.8.2 Kinetic Studies

The kinetic studies were employed to establish the mechanism of methane steam reforming reaction on Ni and Ni alloys. These experiments were conducted isothermally in a packed bed quartz reactor system. The diameter of the quartz reactor was 0.375 inches. Approximately 0.01 g of Ni/YSZ and Sn/Ni/YSZ catalysts with particles sizes of 150-200 μm were diluted in 0.5 g of quartz powder (250 - 400 μm) and loaded in the packed bed reactor. The amount of catalyst and the quartz powder was determined such that no diffusion or mass transport artifacts existed during the experiments. The catalysts were reduced at 1173 K under a stream of 30% H_2/N_2 for 3 hours prior to measuring reaction rates. The rates were measured as the temperature was varied from 923-1073 K. The absence of diffusion and mass transport limitations was confirmed by analyzing the rates as the total space velocity changed. The set-up included a set of mass flow controllers, a pair of thermocouples (inside and outside the reactor), and syringe pumps for water delivery (see Figure 2.8). The lines after the water inlet were heated to 473K to avoid water condensation. The reactor effluent was analyzed using a Varian gas chromatograph (Varian CP 3800) equipped with thermal conductivity detectors (TCD) and a flame ionization detector (FID).

2.4.9 Temperature Programmed Reduction (TPR)

TPR experiments were utilized to study the reduction of catalysts. TPR experiments entail the transformation of a metal oxide to a metal state under the presence of H_2 at elevated temperatures. The experiments were conducted with the ChemBet (3000). Approximately 0.1 g of a catalyst (Ni/YSZ, Sn/Ni/YSZ, or unsupported Sn) was loaded in a U-tube reactor. The temperature was ramped at 10 K/min from 298 K to 1173

K under 30 % H_2/N_2. The TCD signal was detected via the Quatachome data acquisition system.

2.4.10 Thermal gravimetric analysis (TGA)

TGA is a technique utilized to measure the change in the weight of a sample as a function of temperature under a gas environment. For example, we have used TGA experiments to obtain the activation barrier for methane on various catalysts. The catalysts were initially reduced inside the instrument. Once reduced, they were exposed to dry methane and the temperature was ramped to 800°C at a constant rate. We measured the increase in the weight of the catalysts as the temperature increased and the methane decomposed via rxn 1.

$$CH_4 + * \rightarrow C* + 2H_2 \qquad \text{rxn 1}$$

Once the data was obtained for various heating rates, the Redhead analysis [22] was applied to obtain the activation energy for methane dissociative adsorption on various catalysts. In its simplest form, the Readhead equation relates the peak temperature (i.e the temperature at which the adsorption curve peaks from TGA experiments) to the activation energy for dissociative adsorption of methane (see eqn 1).

$$A_a n[*]^{n-1} P_{CH4} \exp(\frac{-E_A}{RT_p}) = \frac{\beta E_A}{RT_p^2} \qquad \text{eqn 1}$$

Where A_a is the rate constant for adsorption of methane and was assumed to be around 10^5/sec [23], E_A is the activation energy for methane decomposition, R is the gas constant, β is the temperature heating rate, [*] is the concentration of free sites, n is the reaction order with respect to the fraction of free sites and P_{CH4} is the partial pressure of methane. A detailed description of this method is provided in Chapter 6.

The TGA was also utilized to analyze the oxidation-reduction behavior of the catalysts. These experiments were conducted to probe the strength of the oxygen-metal bond in these catalysts. The catalysts were reduced under a stream of 30% H_2/N_2 while the temperature was ramped from room temperature to 1073 K at a rate of 10 K/min and was kept isothermal for 2 hours. Once reduced the catalysts were cooled to room temperature using pure N_2. Following this procedure, the catalysts were re-oxidized in air while the temperature was increased from 298 K to 1073 K at 10 K/min and was kept isothermal at 1073 K for 2 hours to assure complete oxidation. Finally, the catalysts were cooled and re-reduced in a stream of 30% H_2/N_2 while the temperature was ramped from room temperature to 1073 K at a rate of 10 K/min.

2.4.11 SOFC electrochemical testing and Impedance Spectroscopy

The solid oxide button cells were assembled using an alumina tube as shown in Figure 2.9. After the button cells were synthesized (procedure described in detailed above), they were sealed on the anode side to an alumina tube using silver paste. The anode was confined inside of the alumina tube while the cathode was left exposed to air. Inside of the alumina tube, a quartz tube was utilized to deliver the fuel. Gold wires were utilized as current collectors. Two wires were attached to the anode and two at the cathode using gold mesh and silver paste.

The electrochemical measurements such as linear sweep voltammetry (I-V), constant voltage or constant current stability tests and electrochemical impedance spectrometry studies were performed using PARSTAT 2273 (Princeton Applied Research).

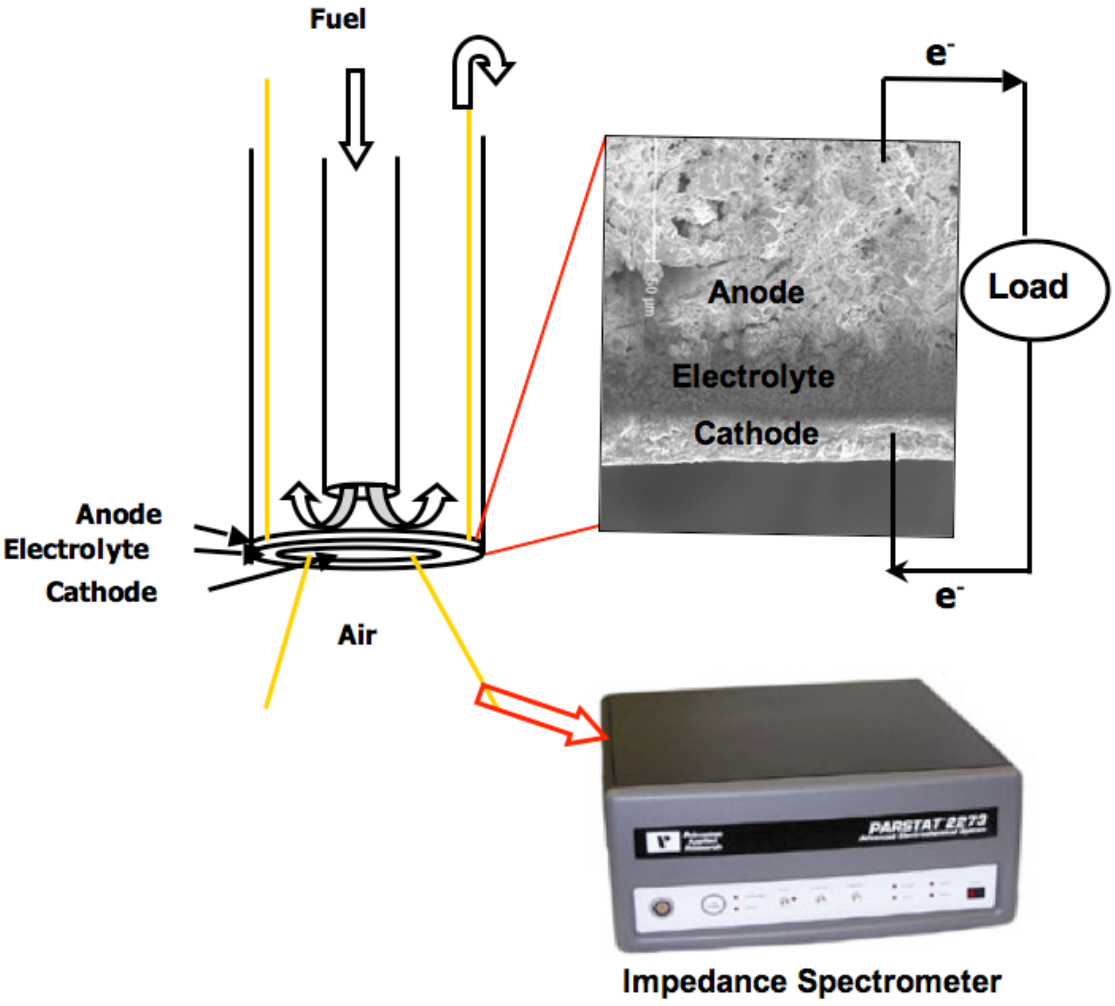

Figure 2.9. Schematic of solid oxide button cell test assembly

In linear sweep voltammetry experiments, a voltage range (from the open circuit voltage (OCV) value to 0.1 V) with a set ramp rate (10-50mV/s) is applied between the working and the reference electrode. In our measurements the working electrode is connected to the anode while the reference electrode is connected to the cathode of the fuel cell. In these measurements, I-V curves were generated as the voltage was varied at a set rate over time. The I-V curves can be utilized to identify the losses or overpotentials in the fuel cell generated due various factors such as the activation of the electrochemical reactions, the ohmic resistance created from the ion conductivity through the electrolyte or mass transfer losses due to gas diffusion as shown in Figure 2.10.

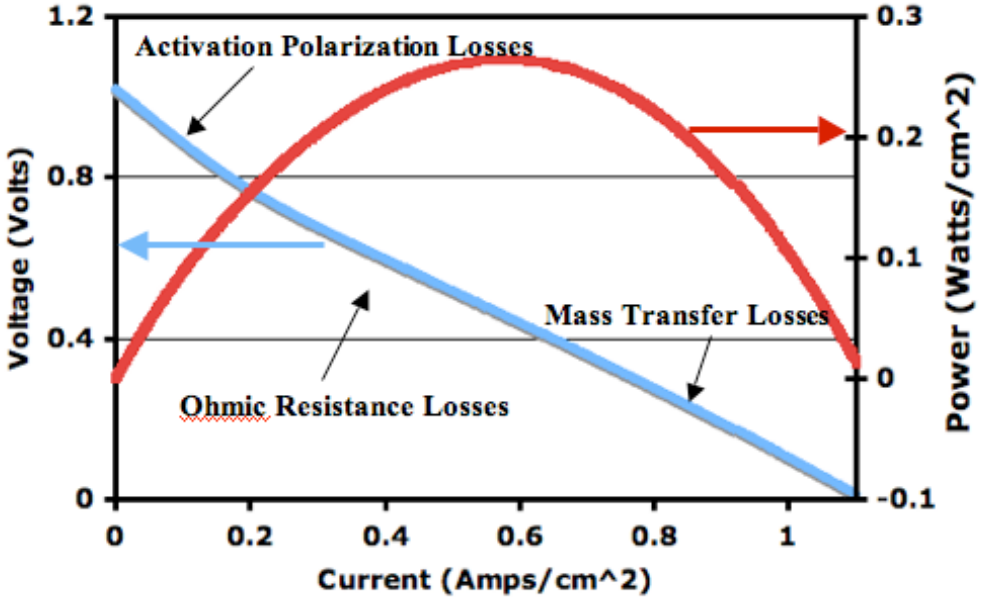

Figure 2.10. I-V and power curves generated for a SOFC at 750°C under 50 sccm of H_2.

Constant voltage or current tests were utilized to measure the performance of the fuel cells as they were exposed to various hydrocarbon fuels. For example, in the constant voltage experiments, the current was measured over time as hydrocarbon fuels

such as methane or isooctane were fed into the anode. The set value for the voltage was varied in order to affect the oxygen flux through the electrolyte. For example, as the voltage increases, the oxygen flux through the electrolyte should decrease which results in a decrease of the oxygen to carbon (determined by the amount of carbon in the hydrocarbon fuel) ratio on the anode.

In the impedance spectroscopy experiments, a small amplitude AC voltage (E) is applied between the working and the reference electrode.[24, 25] The frequency (ω) of the input voltage signal is varied from 1 MHz to 0.01 Hz. The impedance (Z) is obtained by dividing the applied voltage (E) by the current response (I) as shown in eqn 4. The impedance generally has two components: a real component (real Z) and an imaginary component (imag Z). The impedance spectra can be plotted in a Nyquist plot where the negative imaginary component of the impedance is plotted versus the real component of the impedance (see Figure 2.11). From a Nyquist plot one can obtain the polarization (R_p) and the electrolyte resistance (R_e). The polarization resistance is attributed to the ohmic losses between the working and the reference electrode. In our case the working electrode was attached to the anode while the reference to the cathode.

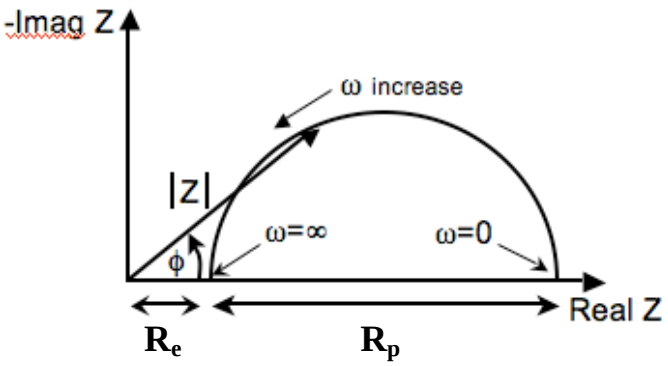

$$Z = \frac{E}{I} = Z_0(\cos\phi + j\sin\phi) \qquad \text{eqn. 4}$$

where

$$E(t) = E_0 \exp(j\omega t)$$

$$I(t) = I_0 \exp(j\omega t - j\phi)$$

Figure 2.11. A schematic Nyquist plot for a SOFC fuel cell. Z refers to the impedance, ω to the frequency, Re to the electrolyte resistance and Rp to the polarization resistance.

In this contribution the impedance spectroscopy experiments were utilized to characterized the fuel cells and compare the resistances across a Ni anode fuel cell and Sn/Ni anode fuel cell. For example Figure 2.12 shows a Nyquist plot obtained for a Ni anode SOFC. The measurement was conducted while the anode was exposed to 50 sccm of humidified H_2 at 1013 K and under open circuit voltage conditions (OCV). Figure 2.12 shows that the resistance across the electrolyte is approximately 0.1 Ωcm^2. The shape of the impedance curve indicates that there are two different resistances across the cell due to the electrodes. Contributions of others have related the resistance at the lower frequency to the anode while the one at the higher frequency to the cathode.[26, 27] Therefore the Nyquist plot indicates that the resistance created across the anode is higher than the one created by the cathode. This is consistent with the findings of others on similar systems.[5, 27] In this thesis, impedance measurements were also used to identify any changes that occurred in the fuel cells due to the exposure to various hydrocarbon fuels.

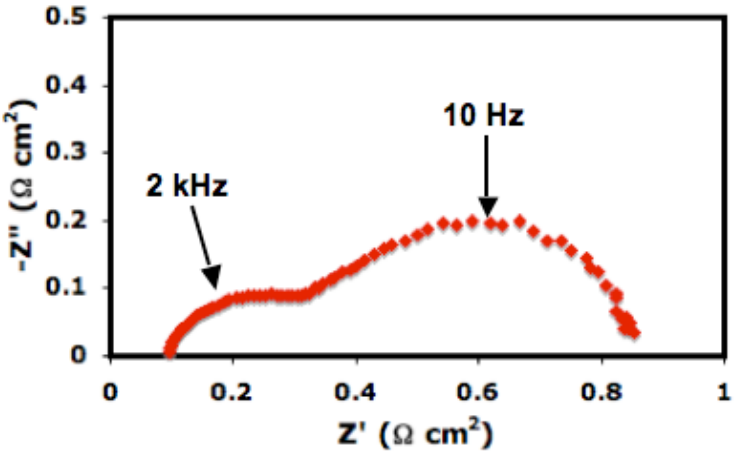

Figure 2.12. Nyquist plot obtained for a Ni/YSZ|YSZ|LSM/YSZ SOFC at open circuit voltage (OCV), 1013 K while operating under a stream of 50 sccm of humidified H_2.

2.5 **Theoretical Techniques**

2.5.1 Density Functional Theory (DFT)

Density functional theory is used to calculate geometries and energies of various species (reactants, products and transition states) participating in chemical transformations. Furthermore it allows us to compute the electron structure of relevant adsorbates and substrates. The main characteristic of DFT methodology is that it utilizes the electron density to describe an interacting system of particles as opposed to the many-body electron wavefunction, which is traditionally used in other methodologies. Employing electron density to describe the many-body system reduces the number of variable from 3N, where N is the number of electrons in the system, to only three spatial variables. The foundation of DFT is based on the contributions from Hohenberg and Kohn that nicely demonstrated for the first time that the total energy of a system of interacting electrons moving under the influence of an external potential is a unique functional of the electron density, see equation 5.[28]

$$E[\rho(r)] = \int \rho(r) v_{ext}(r) dr + F[\rho(r)] \qquad \text{eqn 5}$$

where $E[\rho(r)]$ is the energy functional, $\rho(r)$ is the electron density, v_{ext} is the external potential and $F[\rho(r)]$ is an unknown functional of the electron density. They also showed that the density that minimizes the total energy (E_0) is the exact groundstate density (ρ_0). The only problem with the Hohenberg-Kohn theorem is that $F[\rho(r)]$ was not defined. About a year later, Kohn and Sham demonstrated how to divide $F[\rho(r)]$ into three terms: $T_{KS}[\rho(r)]$ which is the kinetic energy of non-interacting electron gas, $E_H[\rho(r)]$ which is the electrostatic energy of electrons and $E_{XC}[\rho(r)]$ which is the exchange correlation energy that accounts for electron interaction (see eqn 6).[29]

$$F[\rho(r)] = T_{KS}[\rho(r)] + E_H[\rho(r)] + E_{XC}[\rho(r)] \qquad \text{eqn 6}$$

The first two terms can be calculated while the exchange correlation term is unknown. In order to solve for the $E_{XC}[\rho(r)]$ several approximation schemes have been implemented. One of them is the local density approximation (LDA), which computes the exchange and correlation energy from the uniform electron gas. This method assumes that the exchange correlation energy is only a function of the electron density. Another approximation scheme is the generalized gradient approximation (GGA).[30, 31] In this method, the exchange correlation energy is computed based on the electron density and its gradient. GGA is the method utilized in this work.

Slabs and Calculations Details

In this contribution, the Dacapo pseudo-potentials plane wave code (http://www.camp.dtu.dk) was employed for all density functional theory calculations. The metal surfaces were constructed using supercells (see Figure 2.13). A supercell is composed of slabs of atoms separated from each other using vacuum layers. The interface between the slab and the vacuum represents the surface. The surface termination of the slabs was varied in order to model different surface sites such as terraces and steps. For example, (111) surface termination was utilized to represent terrace surface sites and (211) surface termination was utilized to represent the step-edge surface sites. The thickness of the slabs was determined based on a compromise between accuracy and feasibility of the calculations. The slabs were separated using six vacuum layers and a dipole-correction scheme was employed to electro-statically decouple the slabs in the z-direction.

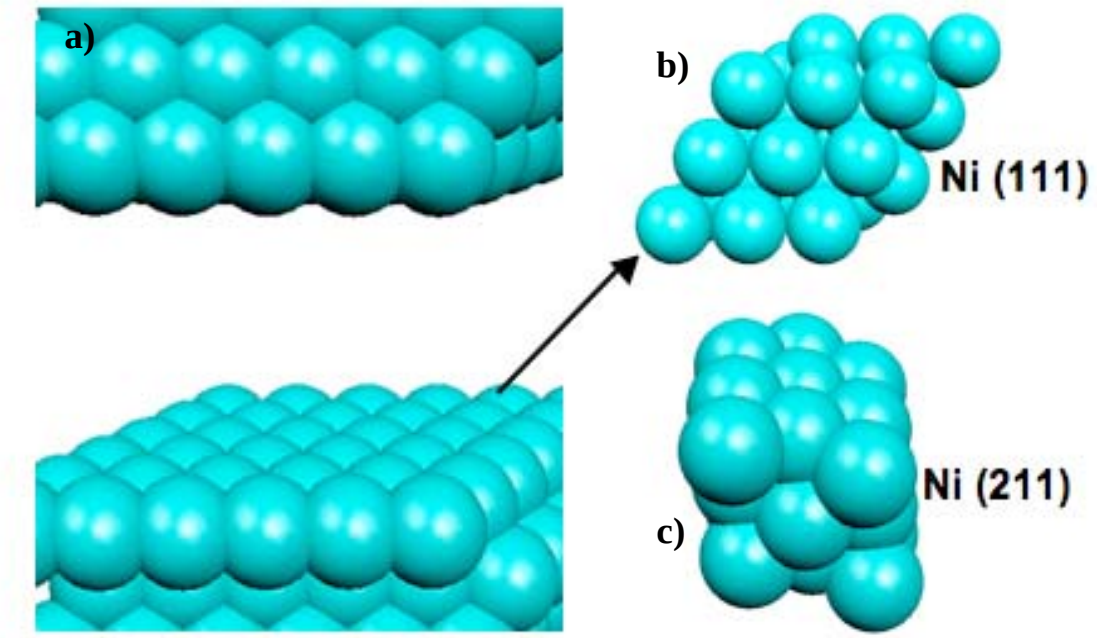

Figure 2.13. Images of a) Ni (111) slabs separated by the vacuum space. b) Ni (111) unit cell utilized to represent the Ni terrace sites (well-coordinated) and c) Ni (211) unit cell utilized to represent the Ni step/edge sites (under-coordinated).

The GGA-PW91 functional was employed for self-consistent spin-polarized electronic structure calculations. Vanderbilt pseudo-potentials were employed to describe core electrons. The density of valence electrons was determined self-consistently by iterative diagonalization of Kohn-Sham Hamiltonian using Pulay mixing of densities. The plane wave basis set used to describe the one-electron states was cut off at 350 eV. An electronic temperature (k_bT) of 0.1 was utilized during calculations with the final results extrapolated to 0 K.

The first order transition states for a one-atom diffusion on a surface were identified by probing the high-symmetry sites between reactant and product states. The diffusing atom was fixed in the x-y plane on these sites and it was allowed to relax in the z direction. Energies were calculated for all high symmetry sites (hollow, bridge, and on-top) and the potential energy surfaces were constructed. The identity of the first order transition states was validated by making sure that the forces acting on the system vanish at the transition state and that the force on the diffusing atom changes sign as it moves through the transition state from the reactant to the product state. We have further validated the transition states by slightly changing the geometry of the transition state along the reaction coordinate towards the product or reactant geometry and allowing the system to fully relax into the respective product and reactant states. This procedure established that the transition state energies are maximum along the reaction coordinate and minimum with respect to other degrees of freedom.

The Climbing Nudged Elastic (cNEB) band method was employed to obtain the reaction pathways and transition states for methane activation on various surfaces. CNEB is a modified version of the Nudged Elastic Band (NEB).[32] In the NEB method, the

minimum energy path (MEP) is identified between a known initial and final state. This is achieved by linearly extrapolating a set of images between the known initial and final states and minimizing their energy. Each image represents a specific geometry of atoms along the reaction pathway. In order to insure the continuity of the reaction pathway (also referred to as the band), the NEB incorporates a spring force between the adjacent images. Therefore the total force acting on an image is composed of the spring force along the local tangent and the true force perpendicular to the local tangent. NEB searches the configuration space for images between the initial and final states with the lowest energies (i.e. the lowest perpendicular force) which combine to form the MEP. The main drawback with this method is that in most cases none of the images in the MEP land exactly at the saddle point. Therefore, a method such as the cNEB is necessary to determine the saddle points. In cNEB, the shape of the MEP is the same as the one obtained from the NEB but a rigorous convergence at the saddle point is also conducted. CNEB identifies the highest energy image from the NEB and converges it to the saddle point by climbing the image up the potential energy surface along the band and down the potential energy surface in the direction perpendicular to the band till it finds the saddle point. Figure 2.14 shows an example of the MEP that we have obtained using cNEB for methane activation on Ni (211). Ni (211) represents a stepped Ni surface. The MEP is composed of the initial, final and transitions states along with other images in between them. The lowest energy initial and final states were determined prior to running the cNEB.

In conclusion, herein we described the theoretical and experimental techniques implemented in this thesis. As we are going to demonstrate in the following chapters,

these techniques are very useful in understanding the chemical transformations that occur on the catalyst surface. This molecular understanding can be very instrumental in identifying new or improved catalytic materials that would maximize the outcome of that particular catalytic process.

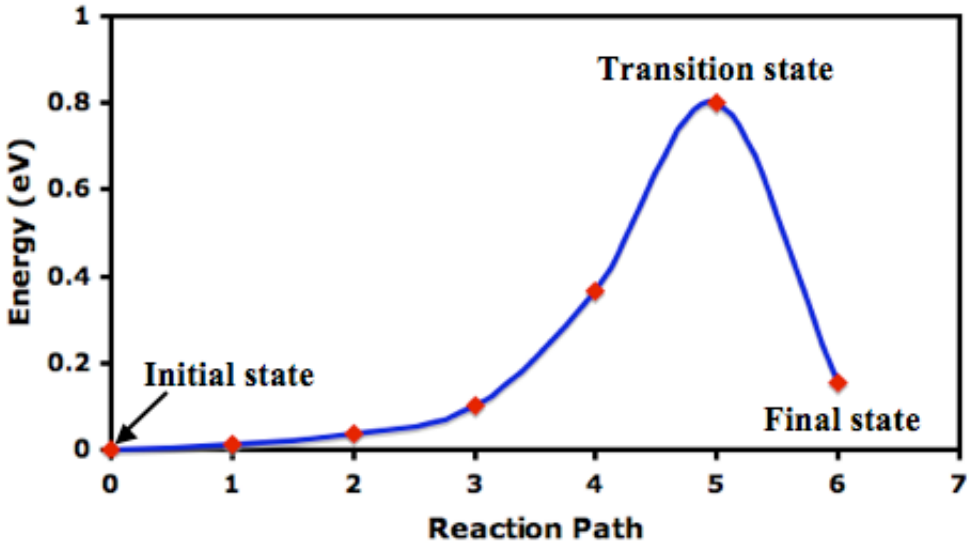

Figure 2.14. The minimum energy path for dissociation of methane (CH_4) to CH_3 and H on Ni(211) (stepped Ni surface) as a function of the reaction path. The energies are computed relative to the energy of the initial state.

2.6 Reference

1. Zhao, F. and A.V. Virkar, *Dependence of polarization in anode-supported solid oxide fuel cells on various cell parameters.* Journal of Power Sources, 2005. 141(1): p. 79-95.

2. Jiang, Y., A.V. Virkar, and F. Zhao, *The effect of testing geometry on the measurement of cell performance in anode-supported solid oxide fuel cells - The effect of cathode area.* Journal of the Electrochemical Society, 2001. 148(10): p. A1091-A1099.

3. Lin, Y.B., et al., *Direct operation of solid oxide fuel cells with methane fuel.* Solid State Ionics, 2005. 176(23-24): p. 1827-1835.

4. Hagen, J., *Industrial Catalysis.* Second ed, ed. J. Hagen. 2006: Wiley-VCH Verlag GmbH & Co. KGaA.

5. Wilson, J.R. and S.A. Barnett, *Solid oxide fuel cell Ni-YSZ anodes: Effect of composition on microstructure and performance.* Electrochemical and Solid State Letters, 2008. 11(10): p. B181-B185.

6. Delannay, F., *Characterization of Heterogenous Catalysts.* 1984, Ney York: Marcel Dekker, Inc.

7. Brydson, R., *Electron Energy Loss Spectroscopy*. 2001: BIOS Scientific Publishers Limited.

8. http://www.emal.engin.umich.edu/instruments/xl30esem.html,

9. Linic, S., *From fundamental studies to rational catalyst design: hybrid experimental/theoretical investigation of ethylene epoxidation*. 2003, University of Delaware.

10. Hillebrecht, F.U., Fuggle, J. C., Bennett, P. A., Zolnierek, Z., Freiburg, C., *Electronic-Structure of Ni and Pd Alloys.2. X-Ray Photoelectron Core-Level Spectra.* Physical Review B, 1983. 27(4): p. 2179-2193.

11. Fuggle, J.C., Hillebrecht, F. U., Zeller, R., Zolnierek, Z., Bennett, P. A., Freiburg, C., *Electronic-Structure of Ni and Pd Alloys.1. X-Ray Photoelectron-Spectroscopy of the Valence Bands.* Physical Review B, 1983. 27(4): p. 2145-2178.

12. Diplas, S., Lehrmann, J., Jorgensen, S., Valand, T., Watts, J. F., Tafto, J., *Characterization of Ni-B amorphous alloys with x-ray photoelectron and secondary ion mass spectroscopy.* Surface and Interface Analysis, 2005. 37(5): p. 459-465.

13. Bennett, P.A., Fuggle, J. C., Hillebrecht, F. U., Lenselink, A., Sawatzky, G. A., *Electronic-Structure of Ni and Pd Alloys.3. Correlation-Effects in the Auger-Spectra of Ni-Alloys.* Physical Review B, 1983. 27(4): p. 2194-2209.

14. Williams, D.B. and C.B. Carter, *Transmission Electron Microscopy*. Vol. 3. 1996: Springer Science & Business Media, Inc.

15. http://www.emal.engin.umich.edu/instruments/2010f.html,

16. Muller, D.A., P.E. Batson, and J. Silcox, *Measurement and models of electron-energy-loss spectroscopy core-level shifts in nickel aluminum intermetallics.* Physical Review B, 1998. 58(18): p. 11970-11981.

17. Muller, D.A. and M.J. Mills, *Electron microscopy: probing the atomic structure and chemistry of grain boundaries, interfaces and defects.* Materials Science and Engineering A-Structural Materials Properties Microstructure and Processing, 1999. 260(1-2): p. 12-28.

18. Muller, D.A., D.J. Singh, and J. Silcox, *Connections between the electron-energy-loss spectra, the local electronic structure, and the physical properties of a material: A study of nickel aluminum alloys.* Physical Review B, 1998. 57(14): p. 8181-8202.

19. Muller, D.A., *Simple model for relating EELS and XAS spectra of metals to changes in cohesive energy*. Physical Review B, 1998. 58(10): p. 5989-5995.

20. Muller, J.E. and J.W. Wilkins, *Band-Structure Approach to the X-Ray-Spectra of Metals.* Physical Review B, 1984. 29(8): p. 4331-4348.

21. Keast, V.J., Scott, A. J., Brydson, R., Williams, D. B., Bruley, J., *Electron energy-loss near-edge structure - a tool for the investigation of electronic structure on the nanometre scale.* Journal of Microscopy-Oxford, 2001. 203: p. 135-175.

22. Masel, R.I., *Principles of adsorption and reaction on solid surfaces*. 1996, Canada: John Wiley & Sons, Inc.

23. Wei, J.M. and E. Iglesia, *Isotopic and kinetic assessment of the mechanism of reactions of CH_4 with CO_2 or H_2O to form synthesis gas and carbon on nickel catalysts.* Journal of Catalysis, 2004. 224(2): p. 370-383.

24. Bieberle, A., *The Electrochemistry of Solid Oxide Fuel Cell Anodes: Experiments, Modeling, and Simulation*. 2000, SWISS FEDERAL INSTITUTE OF TECHNOLOGY: ZÜRICH.

25. Barsoukov, E. and J.R. Macdonald, *Impedance Spectroscopy: Theory, experiment, applications.* second ed, ed. E. Barsoukov and J.R. Macdonald. 2005: Wiley-Interscience.

26. McIntosh, S., J.M. Vohs, and R.J. Gorte, *Impedance spectroscopy for the characterization of Cu-Ceria-YSZ anodes for SOFCs.* Journal of the Electrochemical Society, 2003. 150(10): p. A1305-A1312.

27. Lee, S.I., J.M. Vohs, and R.J. Gorte, *A study of SOFC anodes based on Cu-Ni and Cu-Co bimetallics in CeO2-YSZ.* Journal of the Electrochemical Society, 2004. 151(9): p. A1319-A1323.

28. Hohenberg, P. and W. Kohn, *Inhomogeneous Electron Gas.* Physical Review B, 1964. 136(3B): p. B864

29. Kohn, W. and L.J. Sham, *Self-Consistent Equations Including Exchange and Correlation Effects.* Physical Review, 1965. 140(4A): p. 1133

30. Perdew, J.P., K. Burke, and M. Ernzerhof, *Generalized gradient approximation made simple.* Physical Review Letters, 1996. 77(18): p. 3865-3868.

31. Perdew, J.P., K. Burke, and M. Ernzerhof, *Local and gradient-corrected density functionals.* Chemical Applications of Density-Functional Theory, 1996. 629: p. 453-462.

32. Henkelman, G., B.P. Uberuaga, and H. Jonsson, *A climbing image nudged elastic band method for finding saddle points and minimum energy paths.* Journal of Chemical Physics, 2000. 113(22): p. 9901-9904.

CHAPTER 3

CONTROLLING CARBON CHEMISTRY ON NI BY SURFACE ALLOYING

3.1 Summary

Carbon-induced catalyst deactivation is one of the main problems associated with the electro-catalytic and catalytic reforming of hydrocarbons over supported Ni catalysts. In this chapter, we have utilized DFT calculations to study various aspects of carbon chemistry on Ni surfaces. We demonstrate that the carbon-tolerance of Ni can be improved by synthesizing Ni-containing surface alloys that, compared to monometallic Ni, preferentially oxidize C atoms rather than form C-C bonds and that have a lower thermodynamics driving force associated with the nucleation of carbon atoms on the low-coordinated Ni sites. By utilizing the molecular insights obtained in the DFT calculations we have identified Sn/Ni surface alloy as a potential carbon-tolerant reforming catalyst. The predictions of the DFT calculations were supported by our reactor and catalyst characterization studies, which showed that Sn/Ni is much more resistant to carbon poisoning than monometallic Ni in the steam reforming of methane, propane and isooctane at moderate steam to carbon ratios.

3.2 Introduction

Steam reforming (rxn1) is an endothermic catalytic process that involves the conversion of hydrocarbons and water into hydrogen and oxidized carbon. The reaction is usually accompanied by a slightly exothermic water gas shift process (rxn2).

$C_nH_m + nH_2O \rightarrow nCO + (n+m/2)\ H_2$ (rxn1)

$CO + H_2O \rightarrow CO_2 + H_2$ (rxn2)

Aside from being a crucial process for the catalytic hydrogen production, steam reforming is also an important component of direct electrochemical hydrocarbon reforming over Solid Oxide Fuel Cells (SOFCs) [1, 2]. SOFCs are devices that generate electricity by electrochemically oxidizing various fuels such as hydrogen, CO, and different hydrocarbons. One of the main issues associated with the electro-catalytic and catalytic reforming of hydrocarbons is that commonly used catalysts, such as Ni supported on oxides, deactivate due to the formation of carbon deposits [3-6]. The carbon-induced catalyst deactivation can be suppressed by increasing the feed steam concentration [3]. However, this approach is not optimal for SOFCs since a higher inlet steam concentration results in a lower energy density [7].

There have been several attempts to identify carbon tolerant steam reforming catalysts [5, 6, 8-11]. For example, it has been suggested that Ru and Rh do not facilitate the formation of carbon deposits due to poor carbon solubility in these metals [12, 13]. However, Ru and Rh are prohibitively expensive. It has also been shown that small amounts of sulfur can suppress carbon poisoning by blocking carbon nucleation sites [14, 15]. Similarly, quantum chemical DFT calculations have predicted that Au/Ni surface alloys should exhibit an improved carbon tolerance compared to monometallic Ni. These predications have been verified experimentally [6, 16, 17]. In addition, it has also been

shown that Cu supported on ceria is a stable electro-oxidation catalyst for the internal reforming of hydrocarbons [18-20]. These materials operate at lower temperatures compared to the Ni-based electro-catalysts due to an inferior thermal stability of Cu, thermal incompatibility of ceria and YSZ, and the poor thermal stability of ceria. [21-24]

In this chapter, we have utilized Density Functional Theory (DFT) calculations to study the factors that govern the stability of Ni-based reforming catalysts. We demonstrate that monometallic Ni deactivates due to the high rates of C-C bond formation and a high thermodynamic driving force associated with the nucleation and growth of extended sp2 carbon structures. DFT calculations also show that Sn/Ni surface alloys, with small amount of Sn alloyed into the Ni surface layers, should be more carbon tolerant than monometallic Ni. Furthermore, our DFT calculations illustrate that, in the limit of low Sn concentrations, the formation energy of the Sn/Ni surface alloy is lower than the formation energy associated with the bulk mixing of Sn and Ni and with the separate Sn and Ni phases. The predictions of the DFT calculations are supported by reactor tests, performed under the conditions similar to those associated with the internal on-cell reforming over SOFC anodes. We have also performed various catalyst characterization studies, including scanning electron microscopy (SEM), transmission electron microscopy (TEM), scanning transmission electron microscopy (STEM), energy dispersive x-ray spectroscopy (EDS), x-ray diffraction (XRD), and x-ray photoelectron spectroscopy (XPS), supporting our conclusions.

3.3 Theoretical Details

The Dacapo pseudo-potentials plane wave code (http://www.camp.dtu.dk) was employed for all density functional theory calculations. For the Ni(111) model system,

we utilize 3x3 supercells with 4-layer slabs and 18 special Chadi-Cohen *k*-points. The calculations for the (211) termination surfaces were performed using 1x3 supercells with 9-layer slabs and 3x3x1 Monkhorst-Pack *k*-points. Six layers of vacuum separated the slabs, and a dipole-correction scheme was employed to electro-statically decouple the slabs. The GGA-PW91 functional was employed for self-consistent spin-polarized electronic structure calculations. Vanderbilt pseudo-potentials were employed to describe core electrons. The density of valence electrons was determined self-consistently by iterative diagonalization of Kohn-Sham Hamiltonian using Pulay mixing of densities. The plane wave basis set used to describe the one-electron states was cut off at 350 eV. An electronic temperature (k_bT) of 0.1 was utilized during calculations with the final results extrapolated to 0 K. In the geometry optimization calculations on the (111) surface termination, the two top substrate layers and adsorbates were allowed to fully relax. On the (211) termination, the three top substrate layers were alloyed to relax in the x (normal to the direction if the step-edge) and z directions. The forces were minimized to 0.05eV/A.

The first order transition states for one-atom diffusion were identified by probing the high-symmetry sites between reactant and product states. The diffusing atom was fixed in the x-y plane on these sites and it was allowed to relax in the z direction. Energies were calculated for all high symmetry sites (hollow, bridge, and on-top) and the potential energy surfaces were constructed. The identity of the first order transition states was validated by making sure that the forces acting on the system vanish at the transition state and that the force on the diffusing atom changes sign as it moves through the transition state from the reactant to the product state. We have further validated the

transition states by slightly changing the geometry of the transition state along the reaction coordinate towards the product or reactant geometry and allowing the system to fully relax into the respective product and reactant states [25]. This procedure established that the transition state energies are maximum along the reaction coordinate and minimum with respect to other degrees of freedom. The forces in these calculations were minimized to 0.05 eV/Å. Transition states for the C-O and C-C bond formation were identified using Climbing Nudged Elastic Band method [26-28].

3.4 Experimental Details

3.4.1 Synthesis

Yttria-stabilized zirconia (8 mol %) was prepared via a co-precipitation method [29]. A mixture of yttrium nitrate ($Y(NO_3)_3*6H_2O$) and zirconyl chloride ($ZrOCl_2*2H_2O$) in deionized water was precipitated using a solution of ammonium hydroxide. After filtration and drying over night, the precipitate was calcined at 1073 K for 2 hours. The Ni supported on YSZ catalyst was synthesized by ball milling a mixture of NiO (Alfa Aesar) and 8 mol % YSZ in methanol for 24 hours. Once dried, the powder was pressed into 13mm diameter pellets at 5000 psi. The pellets were then sintered at 1673 K for 4 hours at a ramping rate of 2 K/min. The catalyst was reduced at 1173 K for 5 hours using 30 % H_2/N_2 to insure the full reducibility of the pellets.

Sn was introduced to the sintered pellets via the wet incipient technique using $SnCl_2*4H_2O$ to obtain the desired Sn loading. The pellets were dried over night at 473 K and then reduced under 400 sccm stream of 30 % H_2/N_2 for 5 hours at 1173K.

3.4.2 BET Surface Area Measurements

Single point BET analysis was utilized to measure the surface area of the YSZ support via N_2 adsorption. The surface area of the Ni/YSZ and Sn/Ni/YSZ catalysts was measured using N_2 physisorption at 77 K and H_2 chemisorption at 373 K. The physisorption and chemisorption experiments were conducted using Quatachome's ChemBet 3000 equipped with thermal conductivity detectors (TCD). The catalyst was first reduced at a heating rate of 10 K/min under 30% H_2/N_2 at 1173 K for 5 hours. These experiments yielded almost identical surface areas for the Ni/YSZ and Sn/Ni/YSZ alloy catalysts for a given metal loading.

3.4.3 Temperature Programmed Reduction (TPR).

The TPR experiments were conducted with the ChemBet (3000). Approximately 0.1 g of a catalyst (Ni/YSZ, Sn/Ni/YSZ, or unsupported Sn) was loaded in a U-tube reactor. The temperature was ramped at 10 K/min from 298 K to 1173 K under 30 % H_2/N_2. The TCD signal was detected via the Quatachome data acquisition system.

3.4.4 X-Ray Diffraction (XRD).

The XRD measurements were conducted with a Cu-Kα source using a Philips XRG5000 3 kW x-ray generator with crystal alignment stage and a Rigaku thin film camera. The spectrum was analyzed using Jade v.7 software.

3.4.5 X-ray Photoelectron Spectroscopy (XPS).

The XPS experiments were conducted using Kratos Axis Ultra XPS with 150W Al (Mono) X-ray gun. This instrument was operated ex-situ under a pressure of $5 * 10^{-9}$ torr. Fresh and used samples were pressed on an indium foil and left under vacuum over night. The runs were conducted using pass energy of 40 eV and 20 eV. The charge

neutralizer was utilized to prevent sample charging. The instrument was calibrated with respect to Au $4f_{7/2}$ at 84 eV.

3.4.6 Scanning Transmission Electron Microscopy (STEM), Transmission Electron Microscopy (TEM) and Energy Dispersive X-ray Spectroscopy (EDS).

Joel 2010F electron microscope was used for STEM, TEM and EDS studies. The instrument was operated at 200 kV under a pressure of $1.5 * 10^{-7}$ torr. The instrument is equipped with a zirconated tungsten (100) thermal field emission tip filament. The EDS measurements were performed with the Ametec EDAX system, integrated in the microscope, in spot and scanning modes. To obtain a reasonable current, the lens was set for a probe size of 0.5 nm. The elemental scanning images were obtained using 512 x 512 pixels in a frame at a dwell time of 200 microseconds. To minimize the effect of specimen drift, a drift correction mode was used during the elemental mapping. For each sample we have analyzed several particles from several different areas.

3.4.7 Reactor Testing

The reactor experiments were conducted isothermally at 1073 K in a packed bed reactor set-up. The set-up includes a set of mass flow controllers, a pair of thermocouples (inside and outside the reactor), and peristaltic pumps for liquid delivery. Approximately 0.8 g of catalyst (active material plus support in both powder and pellet form) and a total inlet gas flow-rate of 1400 sccm were used, yielding a gas hourly space velocity (GHSV) of 50,000 hr^{-1}. Gas feeds were delivered with mass flow controllers while liquid fuels and water were supplied via peristaltic pumps. The reactor effluent was analyzed using a Varian gas chromatograph (Varian CP 3800) equipped with thermal conductivity detectors

3.5 Results and Discussions

3.5.1 DFT Studies

The elementary-step mechanism of hydrocarbon steam reforming on Ni has been studied by many investigations.[3, 30, 31] It is generally believed that a hydrocarbon decomposes over Ni, forming carbon and hydrogen adsorbates.[14, 30, 32] Carbon is removed from the catalyst surface in oxidation reactions – oxidizing agents (O and OH) are formed on Ni in the process of steam activation – resulting in the formation of CO and CO_2. In addition to reacting to form CO and CO_2, the C atoms and fragments also react with each other forming extended sp2 carbon networks such as graphene sheets or nanotubes, which deactivate the catalyst. This is illustrated in Figure 3.1(a) where it is shown that a catalytic particle of Ni is completely covered by carbon deposits after the steam reforming of propane at a steam-to-carbon ratio of 1.5. Figure 3.1(b) shows the DFT-calculated reaction energies for various elementary steps involved in methane steam reforming on Ni(111). Similar results were obtained by others. [14, 30] The DFT calculations in Figure 3.1(b) show that there are two thermodynamically stable states of carbon: (i) CO, which is formed in the process of the C atoms oxidation and, (ii) sp2 carbon network (graphene) formed in the process of the C-C bond formation. The formation of the sp2 carbon structures on Ni has received significant attention. [6, 33, 34] For example, recent in-situ transmission electron microscopy (TEM) studies have demonstrated that the carbon structures are formed in the process of the C atom diffusion over the surface of Ni particles and subsequent attachment to a carbon nucleation center[33]. It has been shown that the carbon nucleation centers reside on the under-coordinated sites of Ni. [33]

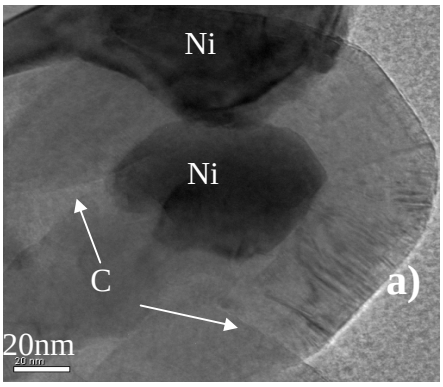

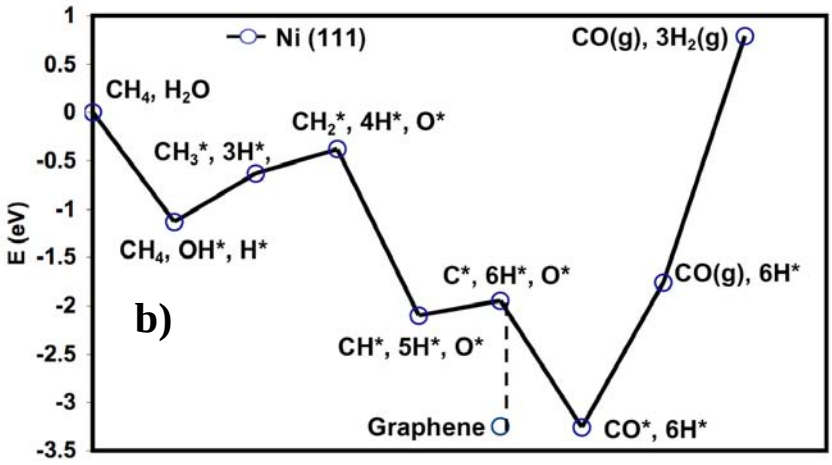

Figure 3.1. a) Transmission Electron Micrographs of the Ni particles covered by carbon deposits. The carbon deposits are formed in the process of propane steam reforming at 1073 K and a steam-to-carbon ratio of 1.5. b) Reaction energies for various elementary steam reforming of methane on Ni(111).

The analysis of Figure 3.1 suggests that any carbon-tolerant catalyst should be able to efficiently oxidize C atoms, while preventing the formation of C-C bonds, i.e., the oxidation of C atoms is a prerequisite for their removal from the surface via either CO desorption or the water gas shift reaction to form CO_2(g) [29]. It has been shown previously that the formation of carbon deposits can be suppressed by modifying the Ni catalyst surface (surface alloying), so that the rate of the C-C bond formation is adversely affected. These molecular insights have led to the identification of Au/Ni surface alloy, which exhibited improved carbon tolerance in the steam reforming of various hydrocarbons. [16, 29]

The problem of carbon poisoning can also be formulated in terms of the selectivity associated with the formation of C-C versus C-O bonds. We have employed this rationalization to identify Sn/Ni surface alloy as a possible carbon-tolerant alternative to monometallic Ni [29]. We note that Sn/Ni catalysts have been previously used in various aqueous and gas phase reforming of hydrocarbon fuels and have shown significant tolerance toward carbon poisoning [5, 8, 35-39]. In Figure 3.2 we show the DFT-calculated potential energy surface associated with the oxidation of a C atom and the potential energy surface for the attachment of a C atom to a carbon nucleation center (the nucleation center is modeled as a sp2 carbon fragment) on the (111) surface termination of Ni and the Sn/Ni surface alloy. The Sn/Ni surface alloy is characterized by the Sn atoms displacing the Ni atoms from the top Ni(111) layer.

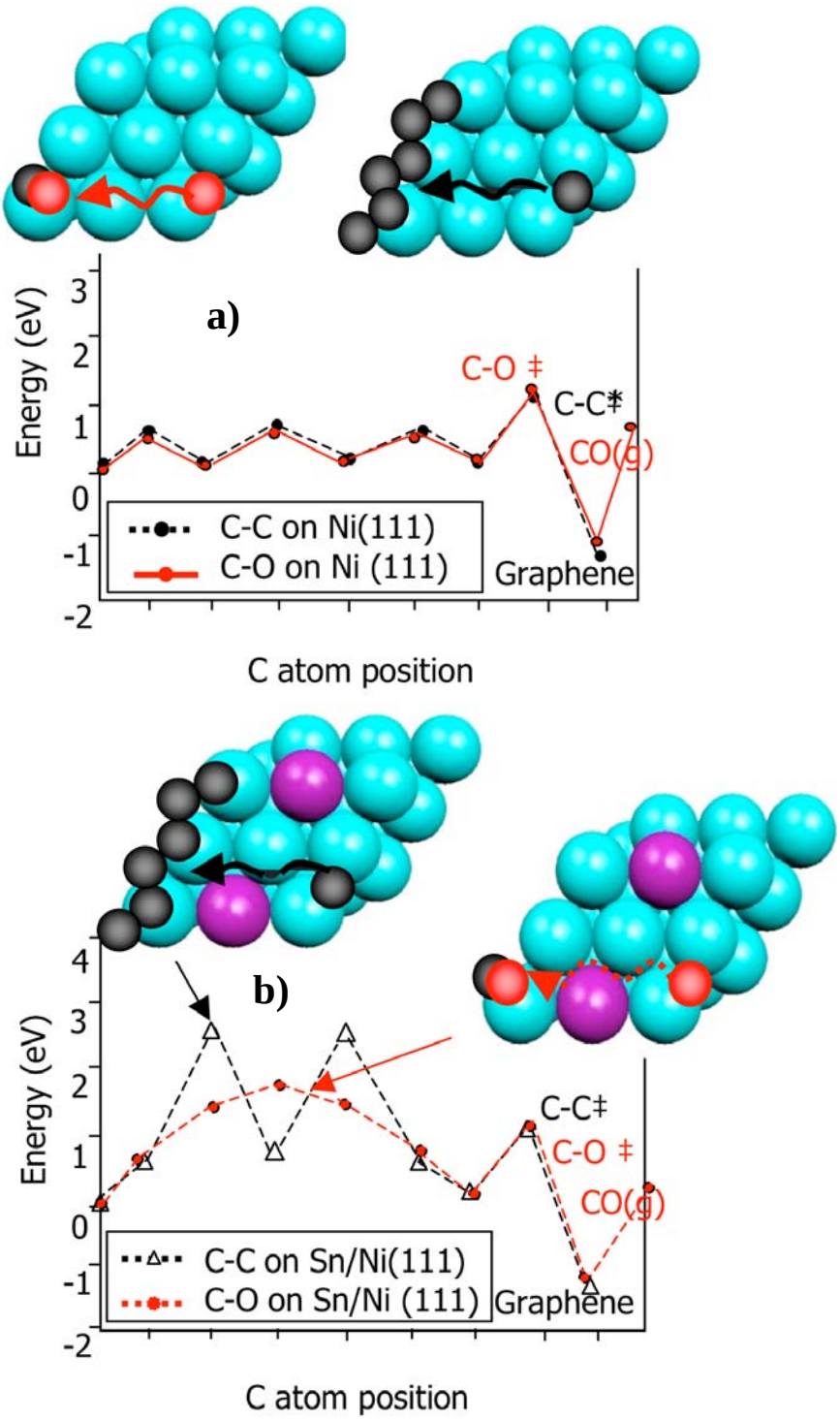

Figure 3.2 DFT-calculated potential energy surfaces for C-C and C-O bond formation on a) Ni (111) and b) a Sn/Ni (111) alloy model system. Inserts show the lowest energy pathways for the reactions on the two model systems. Ni is depicted as large blue (light), Sn is large magenta, C is small black (dark), and O is small red (light).

Figure 3.2 suggests that while on Ni(111), the potential energy surfaces associated with the C-C and C-O bond formation are very similar to each other, on the Sn/Ni surface alloy the activation barrier for the C atom oxidation is much lower than the activation barrier associated with the C-C bond formation. This indicates that the Sn/Ni surface alloy should, compared to Ni, preferentially oxidize C atoms rather than form C-C bonds and therefore it should have a higher resistance toward the formation of the extended sp2 carbon networks.

Another mechanism by which the growth of the carbon networks can be suppressed is to identify those materials that have a low propensity to form carbon nucleation centers. It has been demonstrated previously that carbon nucleation takes place at the under-coordinated Ni sites, and that it requires a number of connected sites [33]. By disrupting the connectivity of the under-coordinated Ni sites, the tendency of a material to form carbon nucleation centers can be suppressed. Since the studies presented in Figure 3.2 demonstrated that the Sn/Ni surface alloy, compared to pure Ni, favors the C atom oxidation as opposed to the C-C bond formation, [29] the question becomes whether the alloying would also have an effect on the carbon nucleation.

In an attempt to answer this question we have utilized the DFT calculations to study the adsorption of various sp2 carbon structures on under-coordinated Ni and Sn/Ni sites. The sp2 carbon networks were modeled in our DFT calculations as a cluster of the sp2 carbon atoms and a graphene chain adsorbed on Ni(211) and Sn/Ni(211). We choose the (211) surface termination since it is a good model for the under-coordinated surface sites [40-42].

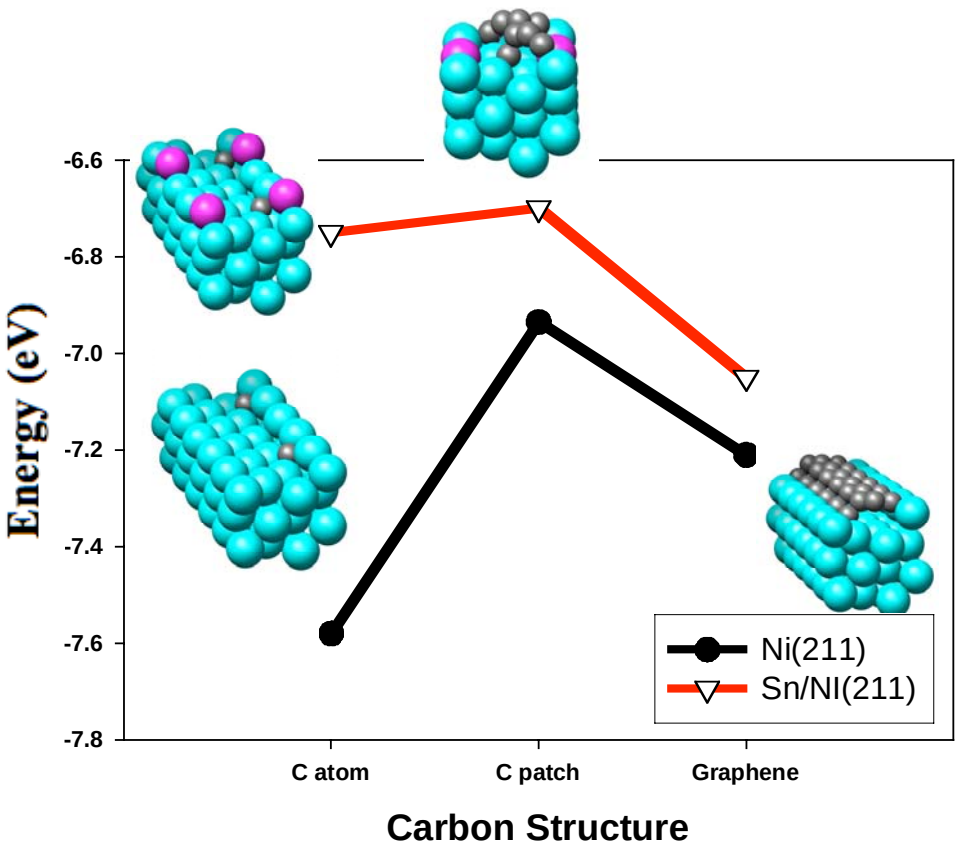

Figure 3.3. The DFT calculated adsorption energies per carbon atom for a C atom, C8 cluster, and a graphene chain adsorbed on Ni(211) and Sn/Ni(211). Ni is depicted as a large blue (light), Sn as large magenta and C as small black (dark) atom. The surface alloy is characterized by replacing every third Ni atom on the edge by the Sn atoms.

In the Sn/Ni model system, the Sn atoms displace the Ni edge atoms as shown in Figure 3.3. We comment on the appropriateness of the model system further below. The DFT calculated adsorption energy for various carbon structures of Ni and Sn/Ni are shown in Figure 3.3. We find that for all carbon structures, the under-coordinated sites on Ni(211) bind carbon more strongly than the under-coordinated sites on Sn/Ni(211). For example, the DFT calculated adsorption energies for a C_8 carbon cluster (8 sp2 carbon atoms) and a graphene chain on Ni(211) are by 0.23 eV and 0.15 eV per carbon atom respectively more exothermic than for Sn/Ni(211), see Figure 3.3. These results suggest that the under-coordinated sites of Sn/Ni bind sp2 carbon structures less strongly than the identical sites on Ni(211), i.e., the thermodynamic driving force to form the sp2 carbon structures on Sn/Ni is much smaller than on Ni. The main reason for this is that Sn breaks the ensembles (ensemble effect) of the low-coordinated Ni atoms, which bind carbon very strongly, therefore lowering the propensity of Ni to nucleate the carbon networks. It is important to note that while the thermodynamic driving force to form the sp2 carbon nucleation centers is affected significantly with the introduction of Sn, the thermodynamic driving force to form CO is changed only slightly. The reason for this is that CO, unlike the sp2 carbon networks, does not require large ensembles of connected Ni sites.

The DFT studies suggest that a checkerboard Sn/Ni surface alloy, with Sn breaking the connectivity of the Ni surface sites, should concurrently enhance the C atom oxidation and decrease the driving force for the formation of the extended sp2 carbon networks. Both mechanisms would affect favorably the carbon tolerance of the Ni-based reforming catalysts.

In our DFT calculations we have employed the model systems with Sn displacing Ni from the top layer of a Ni slab. It is important to verify whether this model system is thermodynamically feasible. We have utilized DFT to calculate the formation energies associated with various Sn/Ni alloy structures. The aim of this study was to identify thermodynamically the most stable Sn/Ni configurations for a given Sn and Ni concentration. Since we are interested in only slightly perturbing Ni, we have explored only the structures in the limit of low Sn concentrations. The formation energy for various Sn/Ni alloy configurations was calculated with respect to pure Ni slab using the following expression.

$$E = E\,(Sn/Ni_{slab}) - N(Sn)\,\mu(Sn) - N(Ni)\,\mu(Ni) - E_{formation}\,(Ni_{slab})$$

$$E_{formation}\,(Ni_{slab}) = E\,(Ni_{slab}) - N\,(Ni_P)\,\mu(Ni)$$

$E(Ni/Sn_{slab})$ and $E(Ni_{slab})$ are the DFT calculated energies of an Sn/Ni alloy and a pure Ni slab respectively, N(Sn) and N(Ni) correspond to the number of the Sn and Ni atoms in the alloy slab, $N\,(Ni_P)$ is the number of Ni atoms in the pure Ni slab, while $\mu(Sn)$ and $\mu(Ni)$ are the respective chemical potentials of Sn and Ni atoms. The chemical potential of Sn and Ni is a function of the concentration of these atoms in a catalytic particle. In this formulation, the formation energy of zero (E = 0) corresponds to the pure Ni slab.

The calculated formation energies (E) for various Sn/Ni structures are plotted in Figure 3.4. The energies were calculated for (911) fcc surface terminations in a (1x3) unit cell. We have utilized this model system since it contains well-coordinated terrace sites and under-coordinated step edge sites. Furthermore, due to the fact that the unit cell is fairly large, certain terrace and step sites are sufficiently far away from each other so that

they are effectively decoupled. This allows us to probe the thermodynamic stability of the structures where Sn is close to the under-coordinated step edge sites and also those structures where Sn is further away from these sites. The values for μ(Sn) and μ(Ni) in Figure 3.4(a) were calculated in the DFT calculations as atomic energies associated with the bulk cubic Sn and fcc Ni lattices respectively. The identical data is plotted in Figure 3.4(b), however, instead of the fixed μ(Sn), we have calculated the formation energies E for a range of Sn chemical potentials. The structure with the lowest formation energy at a given Sn chemical potential is considered thermodynamically the most stable structure.

Figures 3.4(a) and 3.4(b) show that for very low Sn concentrations (low Sn chemical potential), Sn preferentially displaces the under-coordinated Ni atoms from the Ni edge. Note that not every Ni edge atom is displaced by Sn. For example in the unit cell that we use in our calculations, the energetically preferred structure has every third Ni edge atom displaced by Sn. The reason for this is that the introduction of a larger number of Sn atoms in the step edge sites would cause a strain along the step edge, which would increase the energy of the structure. As the concentration of Sn is increased (higher Sn chemical potential), Sn starts displacing the Ni terrace atoms far away from the edge sites. Further increase in the Sn concentration results in the further Ni displacement closer to the edge sites. We also calculate that the formation energy associated with the Sn-induced displacement of the bulk Ni atoms is very high, and this structure is not stable with respect to the separation of Sn and Ni. In addition, the structures where the Sn atoms are adsorbed on the Ni surface are energetically less favorable than the above-discussed surface alloys.

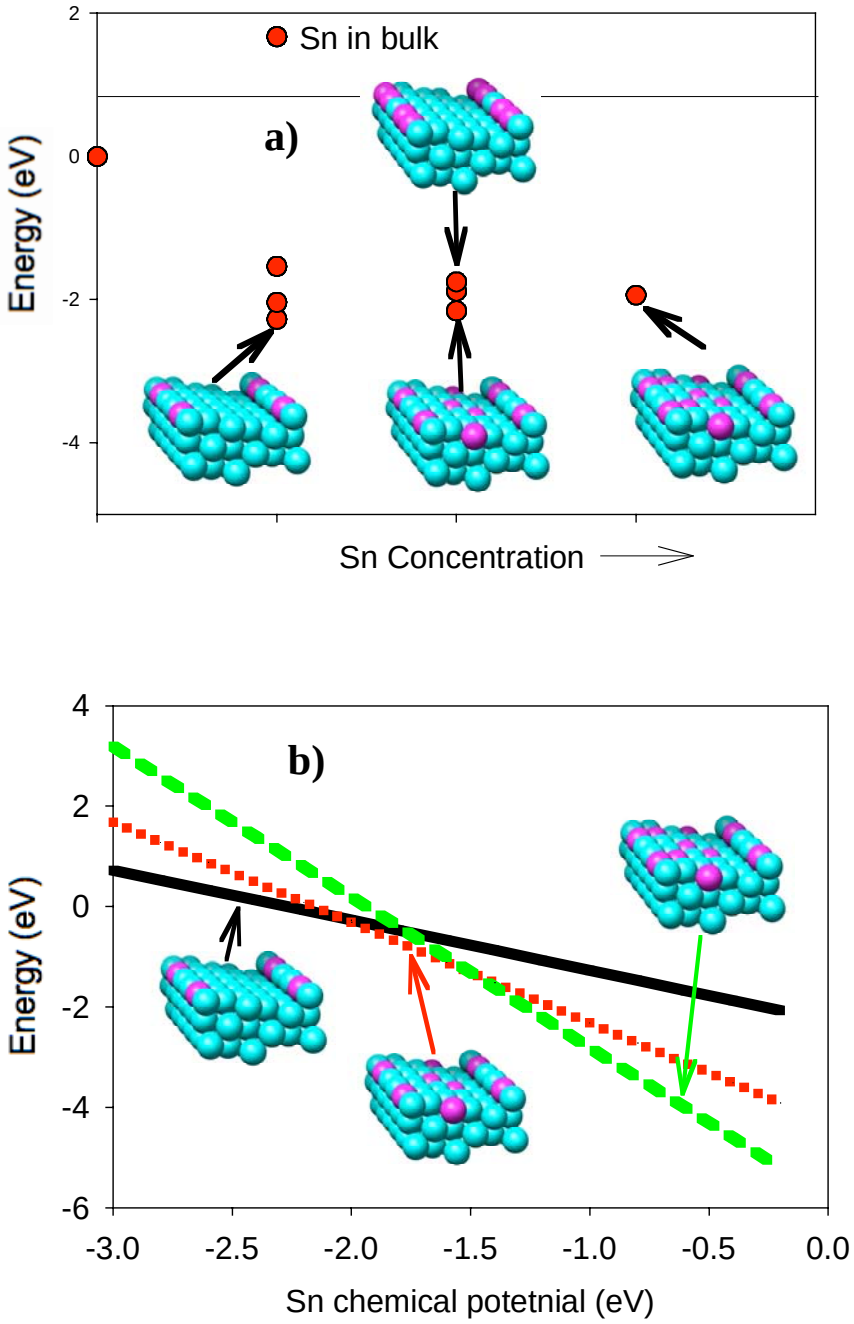

Figure 3.4. a) Formation energy (see text) for various Sn/Ni configurations is plotted as a function of Sn concentration. The structure with the lowest energy is the thermodynamically most stable structure for a given Sn concentration. b) The formation energy of the Sn/Ni configurations is calculated as function of the Sn chemical potential.

These results shown in Figure 3.4 suggest that for low Sn concentrations, the Sn/Ni surface alloy is energetically preferred, and that Sn and Ni preferentially assemble in a checkerboard structure, with Sn first displacing the under-coordinated Ni atoms, followed by the displacement of the Ni terrace atoms. This assembly of Sn and Ni is consistent with the model systems that were utilized in the DFT studies presented above.

3.5.2 Catalysts synthesis and characterization

To test the predictions of the DFT calculations, we have synthesized and characterized Ni/YSZ and Sn/Ni/YSZ catalysts. We have tested these catalysts in the steam reforming of methane, propane, and isooctane at different steam-to-carbon ratios.

The Sn/Ni alloy was synthesized using the wet incipient technique described in the previous chapter. The catalyst was reduced under a 400 sccm stream of 30 % H_2/N_2 at 1173 K for 5 hours. In Figure 3.5(a) we show a Scanning Transmission Electron Micrograph (STEM) of Sn/Ni particles. The elemental mapping of the Sn/Ni particle with Energy Dispersive X-ray Spectroscopy (EDS) shows that at low Sn loadings, less than 1%wt with respect to Ni (1%wt Sn/Ni), the Sn concentration is the highest at the boundaries of the particle. This is most obvious in Figure 3.5(c) where the ratio of Sn to Ni was measured along a line which extends from the edge towards the center of the particle. The EDS line-scan shows that the Sn/Ni ratio is the highest close to the surface of the particle and that it decreases as the probe moves closer to the center of the particle. This is an indication that Sn is mainly located in the surface layers of the particle.

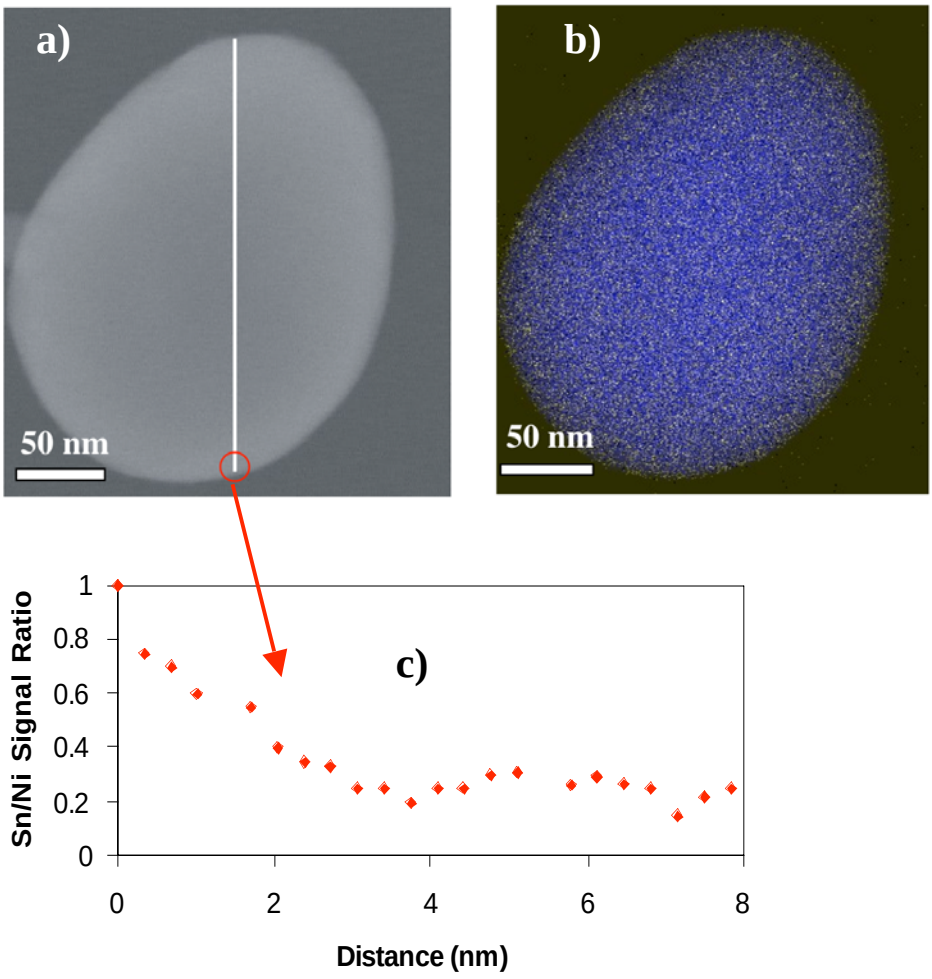

Figure 3.5. a) A Scanning Transmission Electron Micrograph of a 1%wt Sn/Ni particle. b) Energy Dispersive X-ray elemental mapping (EDS) of the Sn/Ni particle showing the distribution of Sn and Ni. Ni is depicted by blue (dark) and Sn by yellow (light) pixels. c) Normalized Sn/Ni ratio (calculated as the ratio divided by the highest measured ratio) as a function of the distance from the lowest edge of the particle.

Furthermore, we have utilized X-ray Photoelectron Spectroscopy (XPS) to characterize the catalysts. The quantified Sn and Ni XP spectra for the 1%wt Sn/Ni/YSZ catalysts established that the concentration of Sn in the surface layers of the alloy was ~25%. The XPS results suggest that Sn preferentially segregates to the surface of the Sn/Ni alloy and further support the model system used in our DFT calculations. The conclusions of the XPS and EDS studies are consistent with the results of the DFT calculations that suggested that in the limit of low Sn concentration, the Sn/Ni surface alloy is thermodynamically the preferred structure.

We have also performed temperature programmed reduction (TPR) studies, shown in Figure 3.6. The TPR was conducted in a stream of 30 % H_2/N_2 and at a heating rate of 10 K/min. The measured reduction temperature for the 1%wt Sn/Ni/YSZ catalyst was lower than the reduction temperatures for Ni/YSZ and unsupported Sn. We note that similar results were obtained by others.[43] These observations suggest that in the alloy, the Sn and Ni atoms are mixed and that the sites that bind oxygen with lower adsorption energy, compared to monometallic Sn and Ni, are created. While it is impossible to ascertain that these results are solely due to the surface alloying, our DFT calculations show that the Sn/Ni surface alloy binds oxygen less strongly than pure Ni or Sn. For example, we find that the oxygen atom binding energy for oxygen adsorbed in the fcc three-fold hollow sites of Ni(111), is by ~1.6 eV more exothermic than for oxygen adsorbed in the hollow sites on of the Sn/Ni(111) surface alloy. Consequently, one would expect that the Sn/Ni surface alloy should reduce at a lower temperature than the Ni.

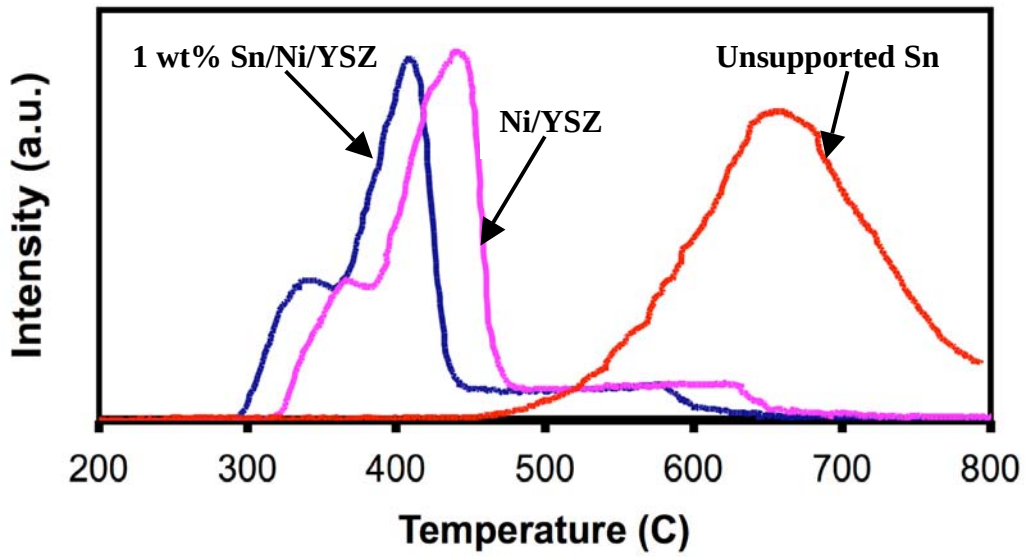

Figure 3.6. Temperature Programmed Reduction (TPR) spectra for 1%wt Sn/Ni/YSZ, Ni/YSZ, and unsupported Sn catalysts. Approximately 0.1g of a catalyst in powder form was used. The catalyst was reduced with a heating rate of 10 K/min and 30 % H_2/N_2.

3.5.3 Reactor Studies

The synthesized catalysts, monometallic Ni supported on YSZ and 1%wt Sn/Ni alloy supported on YSZ, were tested in the steam reforming of methane, propane and isooctane.

In Figure 3.7, we show the normalized conversion of methane (measured conversion divided by the highest measured conversion) over the 1%wt Sn/Ni/YSZ and Ni/YSZ catalysts at a steam-to-carbon ratio of 0.5 and an operating temperature of 1073 K. Figure 3.7 shows that the Ni/YSZ catalyst lost ~ 45 % of its activity after two hours of operations while the 1%wt Sn/Ni/YSZ was stable for as long as it was kept on stream (in this case 15 hr). XRD experiments demonstrated that the Ni/YSZ catalyst deactivated due to the formation of graphitic carbon. The formation of graphitic carbon was not observed for the Sn/Ni alloy catalyst. We also tested the effect of Sn loading on the catalyst performance. It was found that as the Sn loading was increased from 1%wt to 5%wt, the methane conversion was reduced by ~25%, indicating that an increased Sn concentration has a negative effect on the C-H bond activation. Furthermore, we have tested the catalysts in the steam reforming of propane and isooctane at a steam-to-carbon ratio of 1.5 and an operating temperature of 1073 K.

The conversions of propane and isooctane as a function of the time on stream are shown in Figures 3.8 and 3.9(a) respectively. We observe that for both hydrocarbons, the monometallic Ni catalyst deactivated rapidly under these conditions. The deactivation of Ni was accompanied by a large pressure build-up in the reactor bed, which resulted in the disintegration of the bed as corroborated by the visual inspection of the catalyst pellet.

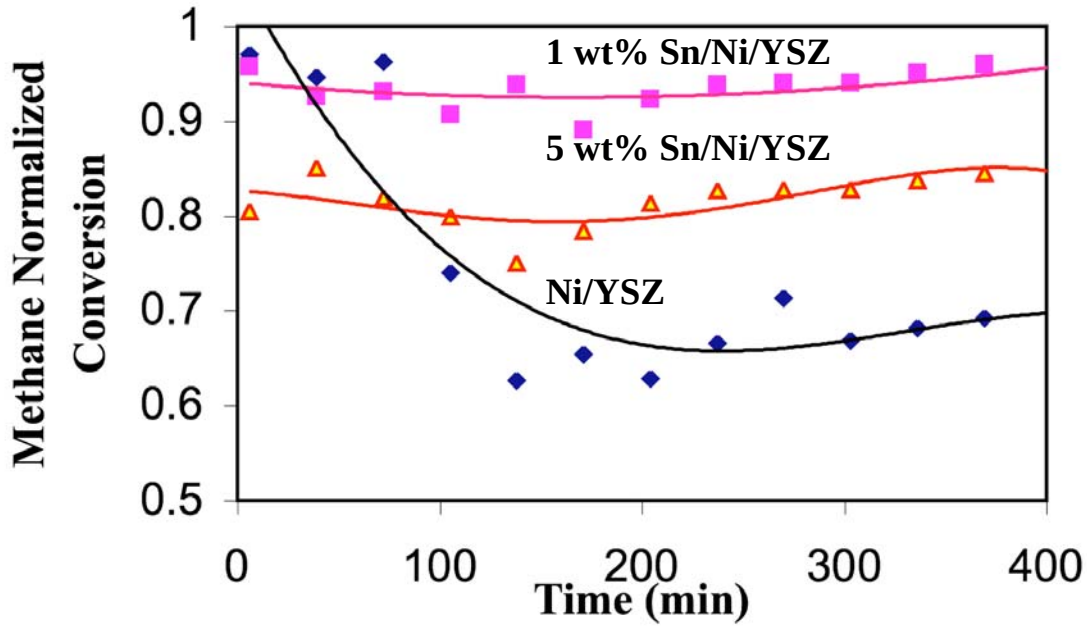

Figure 3.7. Normalized methane conversion (Methane conversion divided by the highest obtained conversion) as a function of the time on stream for 1%wt Sn/Ni/YSZ, 5%wt Sn/Ni/YSZ and Ni/YSZ catalysts measured at the steam-to-carbon ratio of 0.5 and at 1073 K.

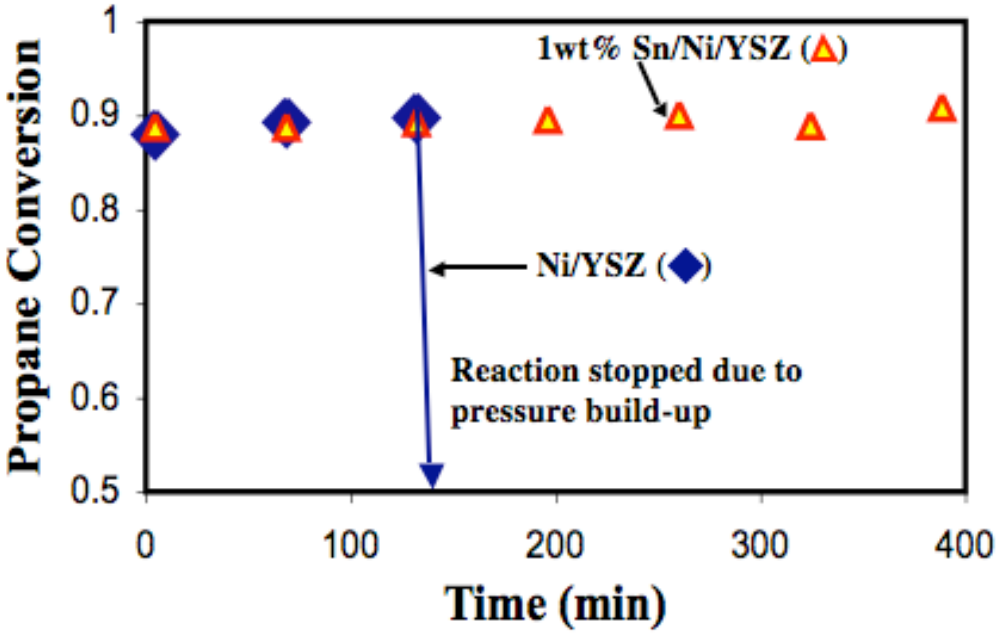

Figure 3.8. Propane conversion as a function of the time on stream at a steam-to-carbon ratio of 1.5 and at 1173 K. The arrow indicates the point in time when carbon build-up resulted in the reactor bed disintegration.

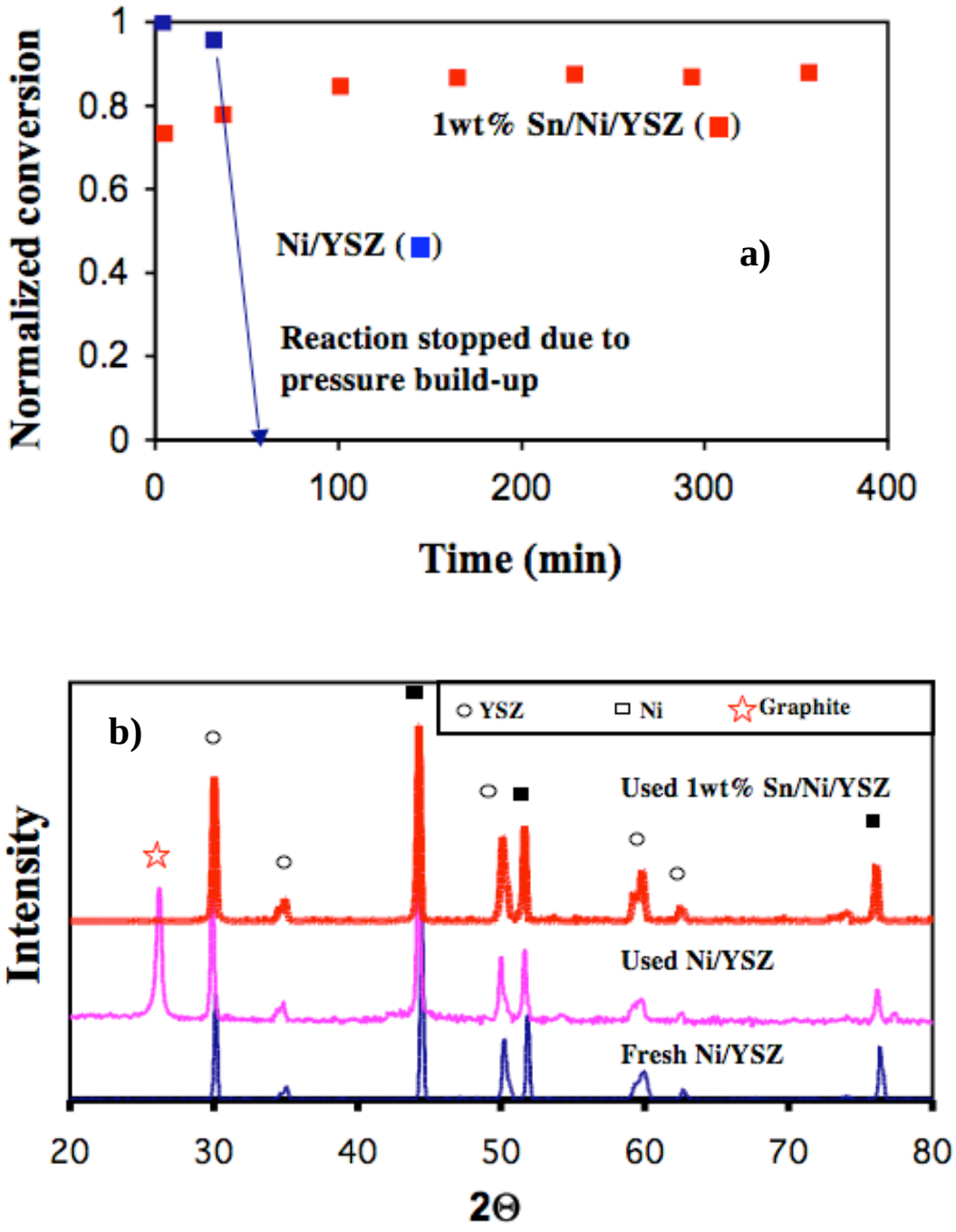

Figure 3.9. a) Normalized conversion of isooctane (measured isooctane conversion divided by the highest measured conversion) for Ni/YSZ and 1%wt Sn/Ni/YSZ catalysts at a steam-to-carbon ratio of 1.5 and at 1073 K. b) XRD spectra for the fresh Ni/YSZ catalyst, used Ni/YSZ and used 1wt% Sn/Ni/YSZ.

We have also observed that the 1%wt Sn/Ni alloy was stable for as long as it was kept on stream, approximately 15 hours. The XRD experiments showed that while the graphitic carbon accumulated on the Ni catalyst, no graphitic carbon was detected on the 1%wt Sn/Ni alloy catalyst, see Figure 3.9(b). Similar results were obtained for steam reforming of propane.

The Ni/YSZ and 1%wt Sn/Ni/YSZ catalysts, utilized in the steam reforming of isooctane at the steam-to-carbon ratio of 1.5, were also analyzed with XPS. We have accounted for any contamination carbon by subtracting the C spectra obtained for a fresh catalyst from the measured spectra associated with the used catalysts. The C1s XP spectrum for the used Ni/YSZ catalyst indicates that there are two distinguishable carbon peaks, one at 284.5 eV associated with the sp2 carbon, and one at 283.1 eV, assigned to metal carbide. [44, 45] The C1s XP spectrum for 1%wt Sn/Ni/YSZ, shown in Figure 10(a), shows no carbon accumulation. It is interesting to note that the amount of carbon deposited on the Ni/YSZ catalyst was so extensive that no Ni signal was detected, i.e., Ni was completely covered by the carbon deposits, see Figure 3.10(b). On the other hand, the Ni XP spectrum associated with the 1%wt Sn/Ni/YSZ catalyst was identical before and after the reaction.

In addition, we have also characterized fresh and used Ni/YSZ and 1%wt Sn/Ni/YSZ catalysts with Scanning Electron Microscopy (SEM) and Transmission Electron Microscopy (TEM). The SEM and TEM experiments show that carbon filaments completely cover the used Ni/YSZ catalyst, see Figure 3.11(a). On the other hand, the SEM and TEM images of the used 1%wt Sn/Ni/YSZ catalysts, shown in Figure 3.11(b), demonstrate that no filaments of carbon are formed on Sn/Ni/YSZ.

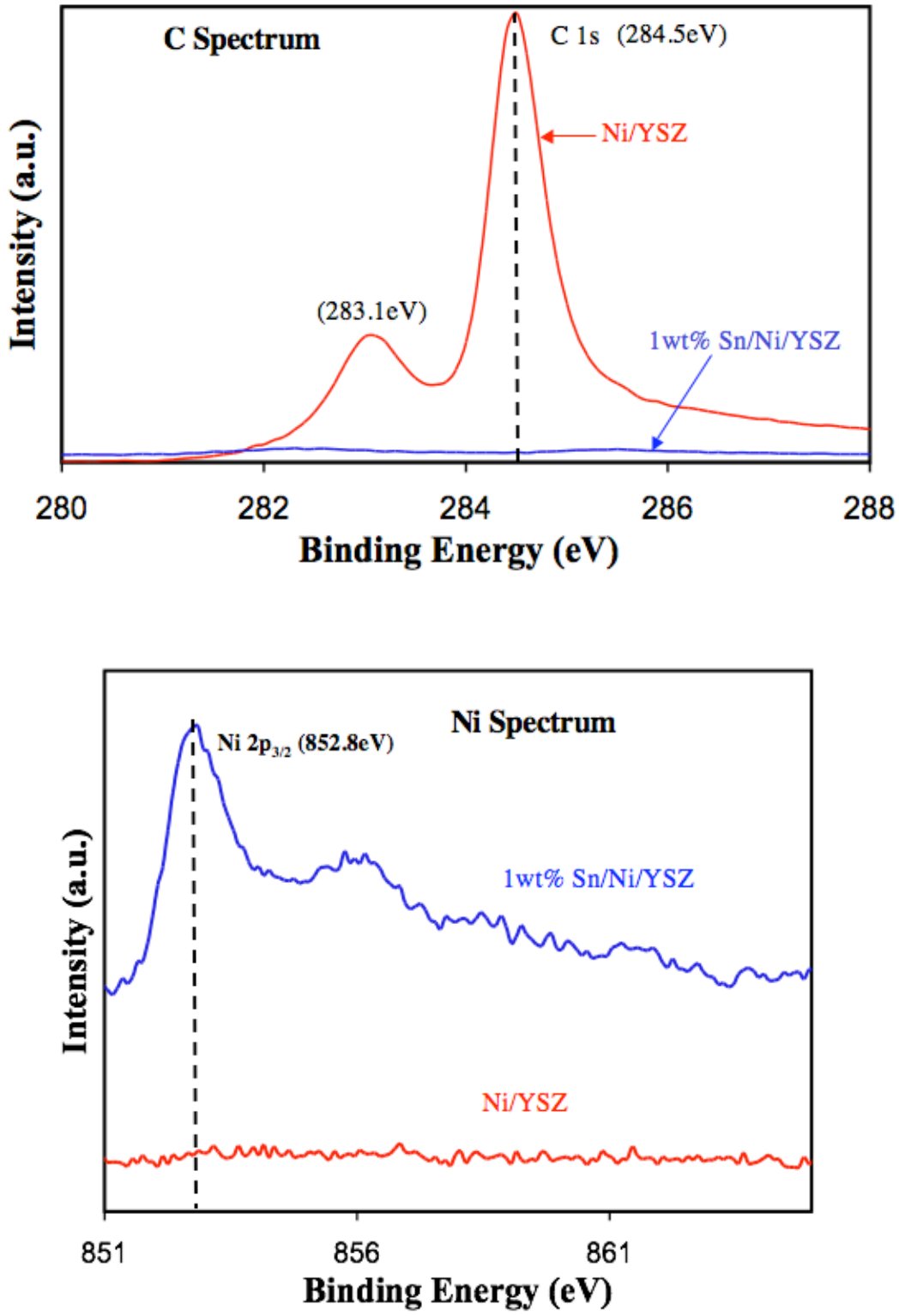

Figure 3.10. The C 1s and Ni ($2p_{3/2}$) XP spectra for the Ni/YSZ and 1wt% Sn/Ni/YSZ catalysts after isooctane steam reforming at a steam-to-carbon ratio of 1.5 and at 1073 K.

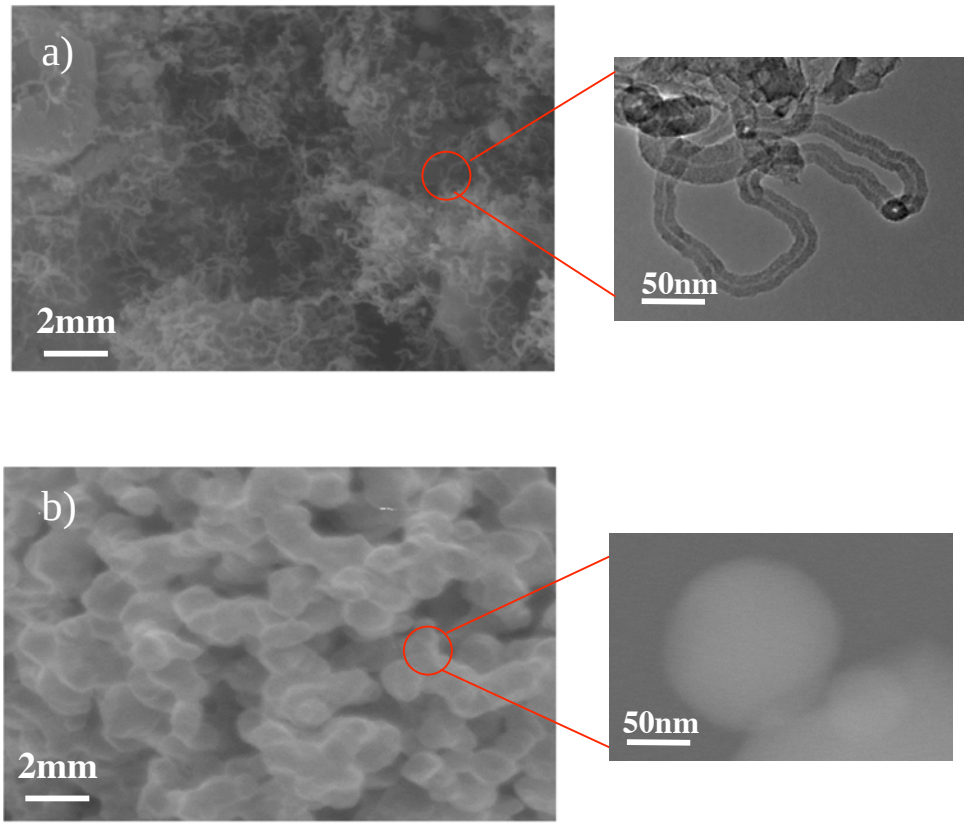

Figure 3.11. a) The SEM and TEM images of Ni/YSZ after isooctane steam reforming at a steam-to-carbon ratio of 1.5 and at 1073 K. The catalyst is completely covert by carbon nanotubes. b) The SEM and TEM images of 1wt% Sn/Ni/YSZ after isooctane steam reforming preformed under the identical conditions as in A. No carbon was detected on the catalyst.

3.6 Conclusions

We have utilized DFT to obtain molecular insights associated with the formation of sp2 carbon structures on Ni reforming catalysts. We have demonstrated that the carbon-tolerance of Ni can be improved by formulated Ni-containing surface alloys that, compared to Ni, preferentially oxidize C atoms rather than form C-C bonds and/or that have lower thermodynamics driving force associated with carbon nucleation on the low-coordinated sites. By utilizing the molecular insights we have identified Sn/Ni surface alloy as a potential carbon-tolerant reforming catalyst. These predictions were supported by our reactor studies, which showed that Sn/Ni is much more carbon tolerant than monometallic Ni in steam reforming of methane, propane and isooctane at moderate steam to carbon ratios.

3.7 **References**

1. Achenbach, E. and E. Riensche, *Methane Steam Reforming Kinetics for Solid Oxide Fuel-Cells.* Journal of Power Sources, 1994. 52(2): p. 283-288.

2. Rostrup-Nielsen, J.R., et al., *Sites for catalysis and electrochemistry in solid oxide fuel cell (SOFC) anode.* Applied Physics A-Materials Science & Processing, 2006. 85(4): p. 427-430.

3. Rostrup-Nielsen, J.R., *Catalytic Steam Reforming,* in *Catalysis - Science and Technology*. 1984, Springer: Berlin.

4. Finnerty, C.M., et al., *Carbon formation on and deactivation of nickel-based/zirconia anodes in solid oxide fuel cells running on methane.* Catalysis Today, 1998. 46(2-3): p. 137-145.

5. Trimm, D.L., *Catalysts for the control of coking during steam reforming.* Catalysis Today, 1999. 49(1-3): p. 3-10.

6. Triantafyllopoulos, N.C. and S.G. Neophytides, *The nature and binding strength of carbon adspecies formed during the equilibrium dissociative adsorption of CH_4 on Ni-YSZ cermet catalysts.* Journal of Catalysis, 2003. 217(2): p. 324-333.

7. Mogensen, M. and K. Kammer, *Conversion of hydrocarbons in solid oxide fuel cells.* Annual Review of Materials Research, 2003. 33: p. 321-331.

8. Trimm, D.L., *Coke formation and minimisation during steam reforming reactions.* Catalysis Today, 1997. 37(3): p. 233-238.

9. Xu, J. and M. Saeys, *Improving the coking resistance of Ni-based catalysts by promotion with subsurface boron.* Journal of Catalysis, 2006. 242(1): p. 217-226.

10. Rostrupnielsen, J.R. and L.J. Christiansen, *Internal Steam Reforming in Fuel-Cells and Alkali Poisoning.* Applied Catalysis A-General, 1995. 126(2): p. 381-390.

11. Takeguchi, T., et al., *Study on steam reforming of CH4 and C-2 hydrocarbons and carbon deposition on Ni-YSZ cermets.* Journal of Power Sources, 2002. 112(2): p. 588-595.

12. Rostrup-Nielsen, J.R., T.S. Christensen, and I. Dybkjaer, *Steam reforming of liquid hydrocarbons.* Recent Advances in Basic and Applied Aspects of Industrial Catalysis, 1998. 113: p. 81-95.

13. Strohm, J.J., J. Zheng, and C.S. Song, *Low-temperature steam reforming of jet fuel in the absence and presence of sulfur over Rh and Rh-Ni catalysts for fuel cells.* Journal of Catalysis, 2006. 238(2): p. 309-320.

14. Abild-Pedersen, F., et al., *Methane activation on Ni(111): Effects of poisons and step defects.* Surface Science, 2005. 590(2-3): p. 127-137.

15. Rostrup-Nielsen, J.R., *Sulfur-Passivated Nickel-Catalysts for Carbon-Free Steam Reforming of Methane.* Journal of Catalysis, 1984. 85(1): p. 31-43.

16. Besenbacher, F., et al., *Design of a surface alloy catalyst for steam reforming.* Science, 1998. 279(5358): p. 1913-1915.

17. Molenbroek, A.M., J.K. Norskov, and B.S. Clausen, *Structure and reactivity of Ni-Au nanoparticle catalysts.* Journal of Physical Chemistry B, 2001. 105(23): p. 5450-5458.

18. Gorte, R.J. and J.M. Vohs, *Novel SOFC anodes for the direct electrochemical oxidation of hydrocarbons.* Journal of Catalysis, 2003. 216(1-2): p. 477-486.

19. Kim, H., et al., *Cu-Ni cermet anodes for direct oxidation of methane in solid-oxide fuel cells.* Journal of the Electrochemical Society, 2002. 149(3): p. A247-A250.

20. Atkinson, A., et al., *Advanced anodes for high-temperature fuel cells.* Nature Materials, 2004. 3(1): p. 17-27.

21. Mogensen, M., N.M. Sammes, and G.A. Tompsett, *Physical, chemical and electrochemical properties of pure and doped ceria.* Solid State Ionics, 2000. 129(1-4): p. 63-94.

22. Atkinson, A., *Chemically-induced stresses in gadolinium-doped ceria solid oxide fuel cell electrolytes.* Solid State Ionics, 1997. 95(3-4): p. 249-258.

23. Lashtabeg, A. and S.J. Skinner, *Solid oxide fuel cells - a challenge for materials chemists?* Journal of Materials Chemistry, 2006. 16(31): p. 3161-3170.

24. Kharton, V.V., et al., *Ceria-based materials for solid oxide fuel cells.* Journal of Materials Science, 2001. 36(5): p. 1105-1117.

25. Linic, S. and M.A. Barteau, *Construction of a reaction coordinate and a microkinetic model for ethylene epoxidation on silver from DFT calculations and surface science experiments.* Journal of Catalysis, 2003. 214(2): p. 200-212.

26. Henkelman, G., B.P. Uberuaga, and H. Jonsson, *A climbing image nudged elastic band method for finding saddle points and minimum energy paths.* Journal of Chemical Physics, 2000. 113(22): p. 9901-9904.

27. Mills, G., H. Jonsson, and G.K. Schenter, *Reversible Work Transition-State Theory - Application to Dissociative Adsorption of Hydrogen.* Surface Science, 1995. 324(2-3): p. 305-337.

28. Linic, S. and M.A. Barteau, *On the mechanism of Cs promotion in ethylene epoxidation on Ag.* Journal of the American Chemical Society, 2004. 126(26): p. 8086-8087.

29. Nikolla, E., et al., *Controlling carbon surface chemistry by alloying: Carbon tolerant reforming catalyst.* Journal of the American Chemical Society, 2006. 128(35): p. 11354-11355.

30. Bengaard, H.S., et al., *Steam reforming and graphite formation on Ni catalysts.* Journal of Catalysis, 2002. 209(2): p. 365-384.

31. Watwe, R.M., et al., *Theoretical studies of stability and reactivity of CHx species on Ni(111).* Journal of Catalysis, 2000. 189(1): p. 16-30.

32. Wei, J.M. and E. Iglesia, *Isotopic and kinetic assessment of the mechanism of reactions of CH_4 with CO_2 or H_2O to form synthesis gas and carbon on nickel catalysts.* Journal of Catalysis, 2004. 224(2): p. 370-383.

33. Helveg, S., et al., *Atomic-scale imaging of carbon nanofibre growth.* Nature, 2004. 427(6973): p. 426-429.

34. Abild-Pedersen, F., et al., *Mechanisms for catalytic carbon nanofiber growth studied by ab initio density functional theory calculations.* Physical Review B, 2006. 73(11).

35. Shabaker, J.W., et al., *Sn-modified Ni catalysts for aqueous-phase reforming: Characterization and deactivation studies.* Journal of Catalysis, 2005. 231(1): p. 67-76.

36. Shabaker, J.W., G.W. Huber, and J.A. Dumesic, *Aqueous-phase reforming of oxygenated hydrocarbons over Sn-modified Ni catalysts.* Journal of Catalysis, 2004. 222(1): p. 180-191.

37. Huber, G.W., J.W. Shabaker, and J.A. Dumesic, *Raney Ni-Sn catalyst for H-2 production from biomass-derived hydrocarbons.* Science, 2003. 300(5628): p. 2075-2077.

38. Padeste, C., D.L. Trimm, and R.N. Lamb, *Characterization of Sn Doped Ni/Al_2O_3 Steam Reforming Catalysts by XPS.* Catalysis Letters, 1993. 17(3-4): p. 333-339.

39. Hou, Z.Y., et al., *Surface properties of a coke-free Sn doped nickel catalyst for the CO_2 reforming of methane.* Applied Surface Science, 2004. 233(1-4): p. 58-68.

40. Hammer, B. and J.K. Norskov, *Adsorbate reorganization at steps: NO on Pd(211).* Physical Review Letters, 1997. 79(22): p. 4441-4444.

41. Mavrikakis, M., et al., *Structure sensitivity of CO dissociation on Rh surfaces.* Catalysis Letters, 2002. 81(3-4): p. 153-156.

42. Pallassana, V., et al., *First principles analysis of hydrogen chemisorption on Pd-Re alloyed overlayers and alloyed surfaces.* Journal of Chemical Physics, 2000. 112(12): p. 5435-5439.

43. Nichio, N., et al., *Stability promotion of Ni/alpha-Al_2O_3 catalysts by tin added via surface organometallic chemistry on metals - Application in methane reforming processes.* Catalysis Today, 2000. 62(2-3): p. 231-240.

44. Wiltner, A. and C. Linsmeier, *Formation of endothermic carbides on iron and nickel.* Physica Status Solidi A-Applied Research, 2004. 201(5): p. 881-887.

45. Tabet, N., I. Allam, and R.C. Yin, *X-ray photoelectron spectroscopy study of the carburization of the nickel-based alloy Haynes 214.* Applied Surface Science, 2002. 195(1-4): p. 166-174.

CHAPTER 4

HYDROCARBON STEAM REFORMING ON NI ALLOYS AT SOLID OXIDE FUEL CELL OPERATING CONDITIONS

4.1 Summary

We demonstrate that supported Sn/Ni alloy catalyst particles are more resistant to deactivation via carbon deposition than supported monometallic Ni particles in steam reforming of isooctane at moderate steam to carbon ratios, irrespective of the average size of metal particles and the metal loading. The steam reforming reactions were performed at conditions that are consistent with typical Solid Oxide Fuel Cell (SOFC) operating conditions. DFT calculations show that the reasons for the enhanced carbon-tolerance of Sn/Ni compared to monometallic Ni are high propensity of Sn/Ni to oxidize carbon and lower driving force to form carbon deposits on low-coordinated metal sites.

4.2 Introduction

In the previous chapter we demonstrated how we have employed DFT calculations in concert with numerous experimental techniques to identify Sn/Ni surface alloy as a carbon tolerant electrocatalyst. We have reported that the Sn/Ni surface alloy exhibits improved carbon tolerance with respect to monometallic Ni in steam reforming of multiple fuels at moderate S/C ratios.[1, 2] These studies were performed at reaction conditions that were consistent with the operation of SOFCs. Furthermore, the metal loading was ~ 45 wt % with respect to the total catalyst (metal plus support) and the average particle diameter was ~ 0.5 μm.

In this contribution we have expanded on the previous studies demonstrating that Sn/Ni surface alloy is much more resistant to carbon deposition than monometallic Ni for a wide range of metal loadings and particle sizes. We have synthesized both steam reforming and SOFC anode electrocatalysts. We have utilized packed bed reactor studies combined with electron microscopy to test and characterize the catalysts.

4.3 Experimental Section

4.3.1 Catalyst Synthesis

8 mol % Yttria-stabilized zirconia (YSZ) was prepared via a standard co-precipitation method [1]. A mixture of yttrium nitrate ($Y(NO_3)_3*6H_2O$) and zirconyl chloride ($ZrOCl_2*2H_2O$) dissolved in deionized water was precipitated using a solution of ammonium hydroxide. After filtration and drying over night, the precipitate was calcined in air at 1073 K for 2 hours.

We have used two different strategies, incipient wetness and ball milling, to introduce Ni on the YSZ support. The main difference between these synthesis strategies

is that they yielded metal particles with significantly different diameters. These two approaches are generally utilized in the synthesis of steam reforming catalysts (incipient wetness) and anode electro-catalysts for SOFCs (ball milling). Therefore, we refer to catalysts synthesized with these two techniques as steam reforming and SOFC anode catalysts, respectively.

The Ni/YSZ steam reforming catalyst was prepared by the incipient wetness technique. An equivalent of ~ 15 %wt of Ni with respect to the total amount of catalyst (Ni plus YSZ) in the form of $Ni(NiO_3)_3$ was dissolved in ethanol and sequentially impregnated on the YSZ support. The catalyst was calcined in air at 873 K for 2 hours and then reduced using a gas mixture of 30 % H_2/N_2 at 1073 K for 5 hours. This procedure resulted in metal particles of ~ 30 nm in diameter anchored on the support. The Sn/Ni/YSZ steam reforming catalyst was prepared by impregnating ~ 3 wt % of Sn, with respect to Ni, in the form of $SnCl_2*4H_2O$ on the calcined NiO/YSZ sample. The catalyst samples were then calcined again at 873 K for 2 hours and reduced under a stream of 30 % H_2/N_2 for 5 hours at 1073 K.

SOFC anode catalyst was prepared by ball milling a mixture of 50 wt% YSZ and 50 wt% of NiO in methanol for 24 hours. Once dried, the powder was pressed into 13 mm diameter pellets at 5000 psi. The pellets were then sintered by ramping the temperature at 2 K/min to 1673 K and keeping them at this temperature for 4 hours. The catalyst was further reduced at 1173 K for 5 hours in a gas mixture of 30 % H_2/N_2 to insure the full reducibility of the pellets. This synthesis procedure yielded catalytic particles with ~ 0.5 μm diameter, as measured by TEM. The resulting catalysts had a nominal Ni loading of 44wt%. The Sn/Ni/YSZ SOFC anode catalyst was prepared by

impregnating $SnCl_2*4H_2O$ (~ 1 wt% with respect to Ni) on the sintered NiO/YSZ pellets via the wet incipient technique. The pellets were dried over night at 473 K and then reduced under a stream of 30 % H_2/N_2 for 5 hours at 1173 K. In our reactor studies we have tested these catalysts in the powder and pellet form. The powder was produced by mechanically crushing the pellets.

4.3.2 Reactor Studies

The reactor experiments were conducted isothermally at 1073 K in a packed bed quartz reactor. The set-up included a set of mass flow controllers for gas delivery, a pair of thermocouples (inside and outside the reactor), as well as peristaltic and syringe pumps for liquid delivery. The reactor effluent was analyzed using a Varian gas chromatograph (Varian CP 3800) equipped with thermal conductivity detectors (TCD) and a flame ionization detector (FID). The mass of the catalysts and the total flowrates were varied to obtain a gas hourly space velocity (GHSV) of 50,000 hr^{-1}.

4.3.3 Temperature Programmed Reduction (TPR)

The TPR experiments were conducted with the ChemBet (3000). Approximately 0.1 g of a catalyst (Ni/YSZ, Sn/Ni/YSZ, or unsupported Sn) was loaded in a U-tube reactor. The temperature was ramped at 10 K/min from 298 K to 1173 K under 30 % H_2/N_2. The TCD signal was detected via the Quatachome data acquisition system.

4.3.4 Scanning Transmission Electron Microscopy (STEM), Transmission Electron Microscopy (TEM), Energy Dispersive X-ray Spectroscopy (EDS) and Electron Energy Loss Spectroscopy (EELS).

Joel 2010F electron microscope was used for STEM, TEM, EDS and EELS studies. The instrument was operated at 200 kV under a pressure of 1.5 * 10-7 torr. The

instrument is equipped with a zirconated tungsten (100) thermal field emission tip filament and a Gatan Imaging Filter (GIF) for electron energy loss spectroscopy (EELS) experiments. The lens conditions during operation were defined for a probe size of about 0.2 nm, with a convergence angle of 13 mrad and a collection angle of 40 mrad. The energy resolution (defined by the full width at half maximum of the zero loss peak) of the energy loss spectra is 1.5 eV at a dispersion of 0.3eV per pixel.

The EDS measurements were performed with the Ametec EDAX system, integrated in the microscope, in spot and scanning modes. To obtain a reasonable current, the lens was set for a probe size of 0.5 nm. The elemental scanning images were obtained using 512 x 512 pixels in a frame at a dwell time of 200 microseconds. To minimize the effect of specimen drift, a drift correction mode was used during the elemental mapping. For each sample we have analyzed many particles from several different areas.

4.3.5 Density Functional Theory (DFT)

The Dacapo pseudo-potentials plane wave code (http://www.camp.dtu.dk) was employed for all calculations. Our approach was to find a set of parameters that ensured the relative convergence, i.e., the convergence of the respective energies of various structures. With this set of parameters we have been able to reproduce various properties such as carbon atom adsorption energies, oxygen adsorption energies, graphene sheet adsorption energy on Ni(111), activation barrier for the attachment of a C atom to the graphene sheet over Ni(111) reported previously by others [3-5]. For the Ni(111) model system, we utilize 3x3 supercells with 4-layer slabs and 18 special Chadi-Cohen k-points. The calculations for the (211) termination surfaces were performed using 1x3 supercells

with 9-layer slabs and 3x3x1 Monkhorst-Pack k-points. Six layers of vacuum separated the slabs, and a dipole-correction scheme was employed to electro-statically decouple the slabs. The GGA-PW91 functional was employed for self-consistent spin-polarized electronic structure calculations. Vanderbilt pseudo-potentials were employed to describe core electrons. The density of valence electrons was determined self-consistently by iterative diagonalization of Kohn-Sham Hamiltonian using Pulay mixing of densities. The plane wave basis set used to describe the one-electron states was cut off at 350 eV. An electronic temperature (kbT) of 0.1 was utilized during calculations with the final results extrapolated to 0 K. In the geometry optimization calculations on the (111) surface termination, the two top substrate layers and adsorbates were allowed to fully relax. On the (211) termination, the three top substrate layers were alloyed to relax in the x (normal to the direction if the step-edge) and z directions. The forces were minimized to 0.05eV/A.

4.4 Results

We have previously performed a number of experimental and theoretical studies to characterize the Sn/Ni/YSZ catalyst.[2] These characterization studies indicated that an impregnation of a small amount of Sn on Ni results in the formation of a Sn/Ni surface alloy. The surface alloy is characterized by Sn mixing with Ni in the surface layers of the Ni particles. For example, DFT calculations showed that the free energy of formation of the Sn/Ni surface alloy, with Sn displacing the under-coordinated Ni atoms at the surface layer of Ni, is lower than the formation energy of other Sn/Ni structures, including bulk alloys and separated Sn and Ni phases.[2] The predictions of DFT calculations have been verified experimentally.[2] For instance, we have utilized x-ray photoelectron

spectroscopy (XPS) to determine that the atomic concentration of Sn in the surface layers of the reduced Sn/Ni catalysts was ~ 25 % for the Sn/Ni particles that contained ~1 wt % of Sn with respect to Ni.[1, 2, 6] Furthermore, we have performed scanning electron energy loss spectroscopy (EELS). Figure 4.1a shows the STEM image of a representative Sn/Ni particle. Figures 4.1b and 4.1c show the EELS spectrum of the Sn M-edge and Ni L-edge respectively for an electron beam focused on a region close to the boundary of Sn/Ni particles and a region close to the center of the particles. Figure 4.1b and 1c demonstrate that the ratio of the Sn M-edge to Ni L-edge is the highest at the boundary of the particle and it decreases as the electron bean is moved closer to the center of the particle. These results provide further evidence that there is an enrichment of Sn close at the surface of the particles of Sn/Ni. Furthermore, our energy dispersive x-ray spectroscopy (EDS) and temperature programmed reduction (TPR) measurements also corroborated the results above suggesting the formation of Sn/Ni surface alloy.[1, 2]

Figure 4.2 shows the conversion of isooctane in steam reforming of isooctane at a steam to carbon (S/C) ratio of 1.5 and an operating temperature of 1073 K for four different catalysts: (1) 15 wt% Ni/YSZ (15 wt % Ni loading with respect to the total catalyst (Ni and YSZ) and average particle diameter of 30 nm), (2) 3 wt% Sn/15 wt% Ni/YSZ (15 wt % Ni loading with respect to the total catalyst, 3 wt% Sn with respect to Ni, and average particle diameter of 30 nm), (3) 44 wt% Ni/YSZ (44 wt% Ni with respect to the catalyst mass and an average particle diameter of 0.5 μm), and (4) 1 wt% Sn/44 wt% Ni/YSZ (44 wt % Ni with respect to Ni plus YSZ, 1 wt % of Sn with respect to Ni, and an average particle diameter of 0.5 μm).

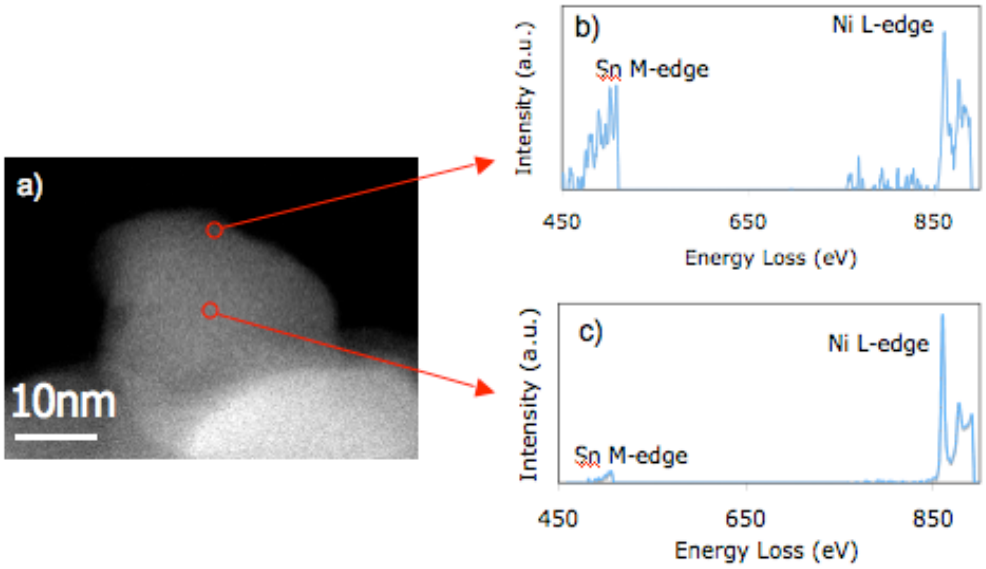

Figure 4.1. a) Scanning Transmission Electron Micrograph (STEM) of a 3Sn/15Ni/YSZ (3 wt% of Sn with respect to Ni, 15 wt% of Ni with respect to the total catalyst) particle. Electron energy loss spectrum (EELS) of the Sn M-edge and Ni L-edge for an electron beam focused on (b) a region close to the boundary of the particle and (c) a region close to the center of the particle.

The procedures used to synthesize these catalysts are described in section 4.3.1. Figure 4.2 shows that the conversion of isooctane for both Sn/Ni/YSZ catalysts, irrespective of metal loading and average particle diameter, was stable for as long as the catalyst was kept on stream. The longest tests lasted for ~ 5 days.

In contrast to the Sn/Ni/YSZ catalysts, the conversion of isooctane on monometallic Ni supported on YSZ deteriorated rapidly for both Ni/YSZ catalysts. The reactor tests also showed that the Ni/YSZ catalyst with smaller Ni particles was more resistant to carbon than the Ni/YSZ catalyst with larger metal particles for identical operation conditions. These observations have also been made by others and are generally attributed to the high energy of carbon deposits, mainly carbon nano-tubes, which form in the process of the deactivation of the Ni particles with small diameter.[7-10] This high energy of carbon deposits results in lower driving force to form these deposits on smaller metal particles.

Electron microscopy studies performed on used Ni/YSZ catalysts showed that the deactivation of Ni/YSZ was the consequence of the formation of carbon deposits which led to the disintegration of Ni particles, resulting in a large pressure drop in the reactor. Figure 4.3a shows a scanning transmission micrograph (SEM) of a used Ni/YSZ catalyst. It is clear that the catalytic particles were completely covered by carbon. Figure 4.3b shows SEM and TEM images of used Sn/Ni/YSZ. Unlike for Ni/YSZ, no carbon deposits were detected on Sn/Ni/YSZ. We have also utilized XPS to characterize the used Ni/YSZ and Sn/Ni/YSZ catalysts.[1, 2] These measurements showed that a substantial amount of graphitic carbon was formed on Ni/YSZ during isooctane steam reforming. On the other hand no appreciable carbon was detected in the case of the Sn/Ni/YSZ catalyst.

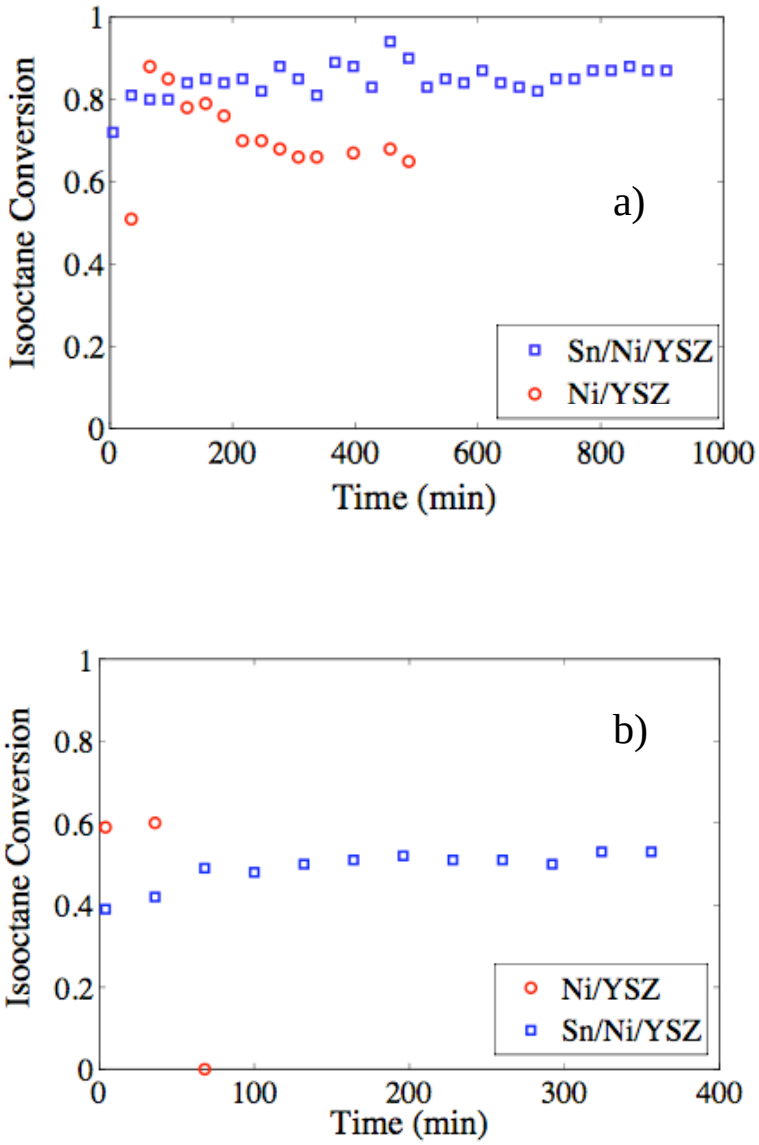

Figure 4.2. a) Isooctane conversion in steam reforming of isooctane at S/C ratio of 1.5 and 1073 K for: a) 15Ni/YSZ catalyst (15 wt% of Ni with respect to the total catalyst) and a 3Sn/15Ni/YSZ catalyst (3 wt% of Sn with respect to Ni, 15 wt% of Ni with respect to the total catalyst). Both catalysts had an average metal particle diameter ~30 nm, b) 44Ni/YSZ catalyst (44 wt% of Ni with respect to the total catalyst) and a 1Sn/44Ni/YSZ catalyst (1 wt% Sn with respect to Ni). Both catalysts had an average metal particle diameter ~ 0.5 μm.

These measurements showed that a substantial amount of graphitic carbon was formed on Ni/YSZ during isooctane steam reforming. On the other hand no appreciable carbon was detected in the case of the Sn/Ni/YSZ catalyst.

4.5 Discussion

Our results presented above show that, irrespective of the size of the catalytic particles or the metal loading, the Sn/Ni is more carbon-tolerant than Ni in steam reforming of isooctane at moderate S/C ratios. These observations suggest that Sn/Ni could be a carbon-resistant alternative to Ni for catalytic hydrogen production from hydrocarbons and for the direct utilization of hydrocarbon fuels in SOFCs. In the next paragraphs, we will identify the underlying molecular principles, grounded in first principles DFT calculations that could explain the improved carbon tolerance of Sn/Ni as compared to monometallic Ni.

It is generally accepted that at high operating temperature (~ 800°C) a hydrocarbon rapidly decomposes on Ni forming adsorbed carbon fragments and hydrogen atoms.[11] In addition, steam activation results in the formation of adsorbed O* and OH*. For example, in Figure 4.4 we show the reaction energies, calculated using DFT, for various elementary steps involved in steam reforming of methane on Ni(111). The Figure shows that on Ni(111) the C fragments with the lowest energy are C* and CH*. Our DFT calculations also indicate that there exists a strong thermodynamic diving force for C* and CH* to further react with O* or OH* to form adsorbed CO*, or to react with each other to form graphitic carbon deposits. It is important to recognize that the formation of CO on Ni provides a pathway for the removal of the C atoms from the catalyst surface in the process of further CO-oxidation of CO to form gas phase CO2.

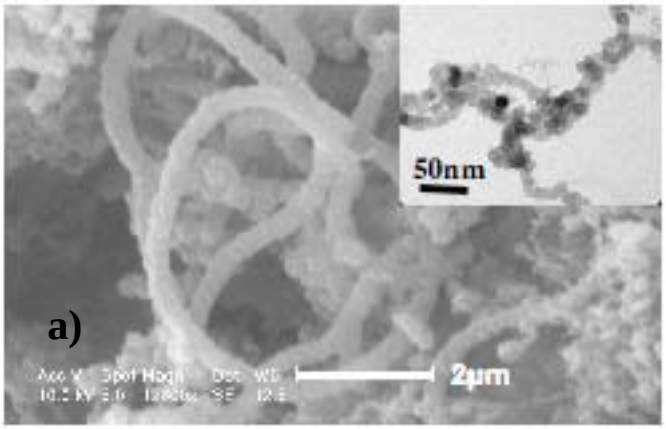

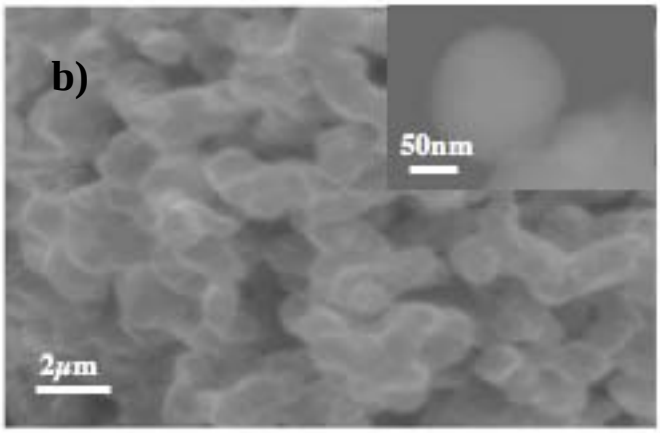

Figure 4.3. a) SEM and TEM images of a 44Ni/YSZ catalyst after steam reforming of isooctane. This process resulted in the formation of carbon filaments. b) SEM and TEM images for a 1Sn/44Ni/YSZ catalyst after steam reforming of isooctane. No carbon was detected on the catalyst.

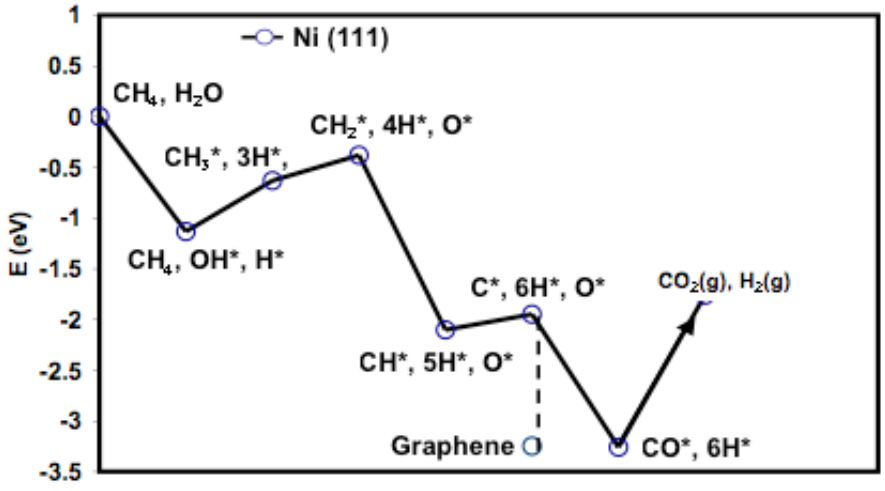

Figure 4.4. a) DFT- calculated reaction energies for elementary steps in steam reforming of methane on Ni(111).

On the other hand the formation of carbon deposits on Ni results in the deactivation of the Ni catalyst. These observations are fairly consistent for different hydrocarbons and also for different surface terminations of Ni with one exception that on the low-coordinated sites of Ni, for example Ni(211), the CH* would be less thermodynamically stable than separated C* and H*.

The mechanism of elementary steps shown in Figure 4.4 suggests that one can formulate the problem of carbon deactivation in terms of the selectivity associated with the formation of C-O versus C-C bonds on Ni. In order to prevent the carbon-induced deactivation, a catalyst should be able to selectively oxidize C atoms rather than form C-C bonds. Figure 4.5 shows the DFT-calculated potential energy surfaces for the oxidation of a C atom and for the attachment of a C atom to a carbon nucleation center (C-C bond formation) on the (111) surface of Ni and the Sn/Ni surface alloy. The carbon nucleation center was modeled as a collection of carbon atoms on Ni organized in the geometry corresponding to the lowest energy. The DFT calculations indicate that on Ni(111) the potential energy surfaces associated with the C-C and C-O bond formation are very similar to each other.

On the other hand, on the Sn/Ni surface alloy the overall activation barrier for the C atom oxidation is much lower than the overall activation barrier for the C-C bond formation. The change in the overall activation barrier is a consequence of the increased barrier for the diffusion of C atoms on the Sn/Ni surface alloy. Similar conclusions were obtained for the diffusion of CH* fragment on these surfaces. The DFT-calculated potential energy surface for the diffusion of CH* and O* on Ni (111) and Sn/Ni alloy (111) are shown in Figure 4.6. It is clear that, in contrast to Ni(111), the barrier for the

diffusion of CH* on Sn/Ni surface alloy is significantly larger that the barrier for the diffusion of O*. These DFT studies indicated that on the Sn/Ni surface alloy, as opposed to monometallic Ni, the oxidation of carbon is kinetically preferred compared to the formation of C-C bonds.

DFT calculations have also demonstrated that in addition to the enhanced capacity to oxidize C atoms, the Sn/Ni surface alloy also lowers the thermodynamic driving force associated with the formation of carbon nucleation centers at the low-coordinated Ni sites. We note that recent in-situ TEM studies and DFT calculations have demonstrated that carbon nucleates on low-coordinated Ni sites.[12] DFT calculated adsorption energies for various carbon nucleation centers (a carbon atom, a cluster of 8 carbon atoms, and a graphene chain) on monometallic Ni and Sn/Ni surface alloy are shown in Figure 4.7. The Figure shows that for all carbon structures, the under-coordinated sites on Ni (to model these sites, the Ni(211) surface was used) bind carbon more strongly than the under-coordinated sites on Sn/Ni(211). The reason for this is that Sn atoms break the ensembles of low-coordinated Ni sites, which interact strongly with carbon, therefore lowering the propensity of these sites to nucleate extended carbon networks.

4.6 Conclusion

We showed that Sn/Ni/YSZ catalyst is more carbon tolerant than Ni/YSZ in steam reforming of isooctane at moderate S/C ratios, irrespective of the average size of metal particles and the metal loading. Our DFT calculations have suggested that the reasons for the enhanced carbon-tolerance of Sn/Ni compared to monometallic Ni are: (i) high propensity of Sn/Ni to oxidize carbon and (ii) lower driving force to from carbon deposits on low-coordinated metal sites.

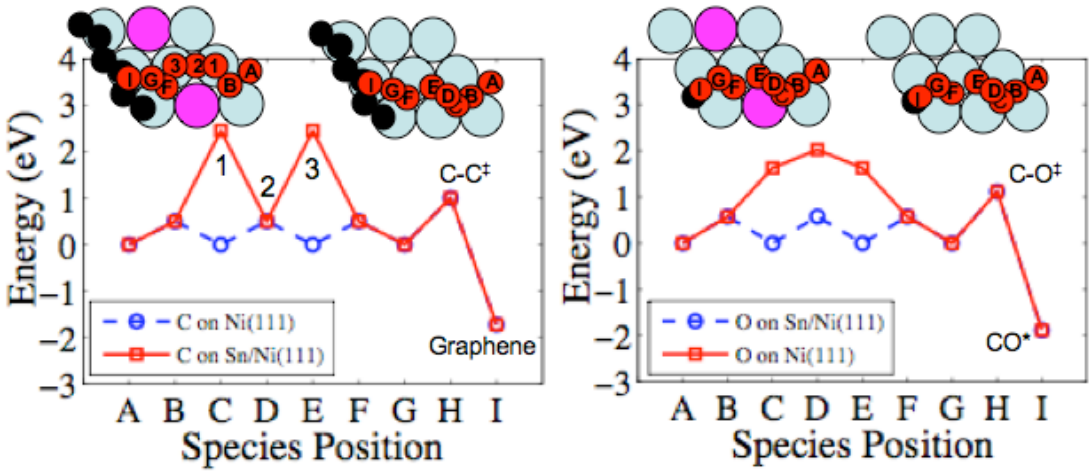

Figure 4.5. a) DFT-calculated potential energy surfaces for C-C bond formation on Ni (111) and Sn/Ni (111). Inserts show the lowest energy pathways for the attachment a C atom to a carbon nucleation center (modeled as a carbon chain) on the two surfaces and b) C-O bond formation on Ni (111) and Sn/Ni (111). Inserts show the lowest energy pathways. Ni is depicted as large blue (light) atom, Sn as a large purple atom, carbon chain as a chain of small black atoms.

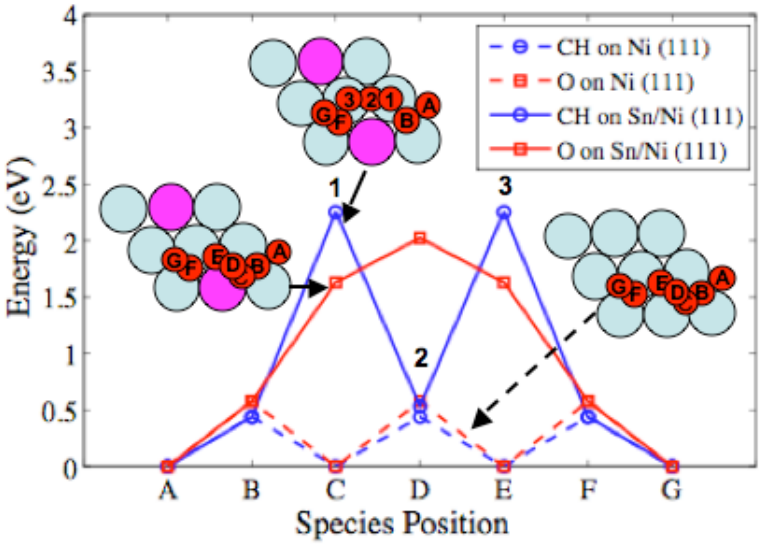

Figure 4.6. DFT-calculated diffusion pathways for O and CH on Ni (111) and Sn/Ni (111). Inserts show the lowest energy pathways. On Ni (111) both O and CH follow pathway ABCDEFG path. On Sn/Ni (111), O follows pathway ABCDEFG while CH follows pathway AB123FG. Ni is depicted as a large blue (light) atom and Sn is depicted as a large purple atom.

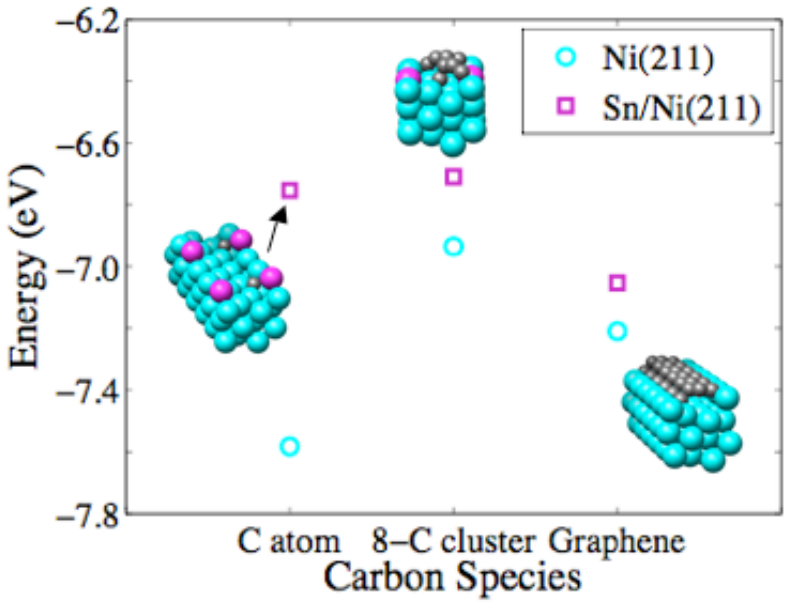

Figure 4.7. DFT-calculated adsorption energies per carbon atom for a C atom, 8-C cluster, and a graphene chain adsorbed on Ni(211) and Sn/Ni(211).

4.7 References

1. Nikolla, E., Holewinski, A., Schwank, J., Linic, S., *Controlling carbon surface chemistry by alloying: Carbon tolerant reforming catalyst.* Journal of the American Chemical Society, 2006. 128(35): p. 11354-11355.

2. Nikolla, E., J. Schwank, and S. Linic, *Promotion of the long-term stability of reforming Ni catalysts by surface alloying.* Journal of Catalysis, 2007. 250(1): p. 85-93.

3. Abild-Pedersen, F., Norskov, J. K., Rostrup-Nielsen, J. R., Sehested, J., Helveg, S., *Mechanisms for catalytic carbon nanofiber growth studied by ab initio density functional theory calculations.* Physical Review B, 2006. 73(11).

4. Abild-Pedersen, F., Lytken, O., Engbaek, J., Nielsen, G., Chorkendorff, I., Norskov, J. K., *Methane activation on Ni(111): Effects of poisons and step defects.* Surface Science, 2005. 590(2-3): p. 127-137.

5. Watwe, R.M., et al., *Theoretical studies of stability and reactivity of CHx species on Ni(111).* Journal of Catalysis, 2000. 189(1): p. 16-30.

6. Enever, M., Linic, S., Uffalussy, K., Vohs, J. M., Barteau, M. A., *Synthesis, structure, and reactions of stable oxametallacycles from styrene oxide on Ag(111).* Journal of Physical Chemistry B, 2005. 109(6): p. 2227-2233.

7. Rostrup-Nielsen, J.R., J. Sehested, and J.K. Norskov, *Hydrogen and synthesis gas by steam- and CO_2 reforming.* Advances in Catalysis, Vol 47, 2002. 47: p. 65-139.

8. Rostrup-Nielsen, J. and J.K. Norskov, *Step sites in syngas catalysis.* Topics in Catalysis, 2006. 40(1-4): p. 45-48.

9. Chen, X.Y., A.R. Tadd, and J.W. Schwank, *Carbon deposited on Ni/Ce-Zr-O isooctane autothermal reforming catalysts.* Journal of Catalysis, 2007. 251(2): p. 374-387.

10. Gould, B.D., X.Y. Chen, and J.W. Schwank, *Dodecane reforming over nickel-based monolith catalysts.* Journal of Catalysis, 2007. 250(2): p. 209-221.

11. Bengaard, H.S., Norskov, J. K., Sehested, J., Clausen, B. S., Nielsen, L. P., Molenbroek, A. M., Rostrup-Nielsen, J. R., *Steam reforming and graphite formation on Ni catalysts.* Journal of Catalysis, 2002. 209(2): p. 365-384.

12. Helveg, S., Lopez-Cartes, C., Sehested, J., Hansen, P. L., Clausen, B. S., Rostrup-Nielsen, J. R., Abild-Pedersen, F., Norskov, J. K., *Atomic-scale imaging of carbon nanofibre growth.* Nature, 2004. 427(6973): p. 426-429.

CHAPTER 5

NI ALLOYS AS PROMISING CARBON TOLERANT SOFC ANODES

5.1 Summary

Solid oxide fuel cells (SOFCs) are solid-state electrochemical devices that in principle can directly convert the chemical energy of hydrocarbons into electrical energy. One of the challenges with this process is the deactivation of the conventional Ni based SOFC anodes due to carbon poisoning. We have shown previously using DFT calculations and reactor studies that Sn/Ni surface alloy catalysts are more carbon tolerant than monometallic Ni catalysts in steam reforming reaction at close to stoichiometric steam-to-carbon ratios. In this chapter, we show that Sn/Ni surface alloy is also a more carbon tolerant anode electrocatalyst than Ni in the electro-chemical oxidation of hydrocarbons on SOFCs.

5.2 Introduction

It is well established that conventional Ni/YSZ SOFC anodes are poisoned by carbon deposits when exposed to hydrocarbons.[1-11] Although there have been many attempts in the literature to prevent carbon poisoning of the SOFC anodes,[1-3, 6, 12-18] carbon poisoning of the anodes still remains an issue. For example, Gorte and coworkers have shown that one can prevent carbon poisoning by replacing the Ni anodes with Cu/ceria.[1, 2, 13] In these systems, Cu acts mainly as an electron conductor, while ceria catalyzes the electrochemical oxidation reactions. Cu/ceria anodes have been shown to operate on various hydrocarbon fuels including jet fuels and Pennsylvania crude oil without significant deactivation due to carbon poisoning.[19] Even though Cu/ceria anodes show promise, there are a number of operational problems associated with these materials. For example these anodes undergo thermal degradation at high temperatures. Furthermore fuel utilization in these anodes is fairly low which compromises the SOFC efficiency. Zhan et al. have shown that incorporating a catalyst layer of Ru-CeO before the Ni anode compartment is another way of preventing carbon poisoning of the Ni anode when operating with hydrocarbon fuels such as isooctane and propane.[17, 18] They demonstrated that the layer of Ru-CeO prevented carbon poisoning of the anode by reforming the hydrocarbons before reaching the Ni anode.

In previous chapters, we have described our effort in utilizing density function theory (DFT) calculations to identify the mechanisms that govern carbon-induced deactivation of Ni catalysts. These studies have suggested that Sn/Ni surface alloy might be a more carbon tolerant catalyst than monometallic Ni.[20-22] In this chapter, we test the Sn/Ni surface alloys in direct electro-chemical oxidation of hydrocarbons on SOFCs.

We have performed various electrochemical tests to measure the performance and stability of Sn/Ni and Ni anodes. Scanning electron microscopy (SEM) and energy dispersive x-ray spectroscopy (EDS) are used to characterize the SOFCs anodes.

5.2.1 Experimental methods

5.2.1.1 SOFCs Preparation and Electrochemical Testing

We have synthesized planar, anode-supported solid oxide fuel cells (SOFCs). Anode-supported SOFCs are characterized by a thick anode (0.5-1 mm), which supports both the electrolyte and the cathode. The fuel cells were approximately 1 inch in diameter and 1 mm thick. The anode was prepared by ball milling NiO (Alfa Aesar), YSZ (co-precipitation), and the pore former (graphite) in deionized water for 24 hours. The mixture was dried and pressed into 1-inch diameter pellets. The anode pellets were then annealed at 1273 K for 6 hours. The electrolyte layer was prepared by drop coating YSZ dissolved in ethanol on one side of the anode pellet. This was followed by sintering of the pellets at 1723 K for 5 hours to obtain the desired density of the electrolyte. The cathode was prepared by ball milling equal amounts of LSM ($La_{0.85}Sr_{0.15}MnO_3$)(Praxair) and YSZ in ethanol. The mixture was then applied on top of the electrolyte. Finally, the fuel cell was annealed at 1373 K for 5 hours to obtain the appropriate microstructure of the cathode. Gold wires were used as current collectors. Two wires were attached to the anode and two at the cathode using gold mesh and silver paste. The fuel cells were sealed on the anode side to an alumina tube using silver paste. The entire cell was placed inside of a furnace and the temperature was ramped at 2 K/min to 973 K. In this process, the anode was exposed to pure hydrogen while the cathode was left open to air. The open circuit voltage (OCV) was monitored to assure the full reduction of the anode. The

electrochemical measurements including linear sweep voltammetry (I-V), constant voltage or constant current stability tests, and electrochemical impedance spectrometry were performed using PARSTAT 2273 (Princeton Applied Research).

5.2.2 Scanning Electron Microscopy (SEM) and Energy Dispersive X-ray Spectroscopy (EDS)

We have utilized the Philips XL30 Environmental Scanning Electron Microscope (SEM) to obtain images of the fresh and used solid oxide fuel cells. This microscope has a resolution of a few nanometers and is equipped with an energy dispersive x-ray spectrometer (EDS) in an Ametec EDAX system.

5.3 Results

To demonstrate the viability of the Sn/Ni anodes, we have tested the performance of SOFCs with Sn/Ni and monometallic Ni anodes in direct electrochemical oxidation of hydrogen and hydrocarbons. Figure 5.1 shows the measured cell voltage and power density as a function of current density for Sn/Ni anode and Ni anode SOFCs when exposed to humidified (3% H_2O) H_2 at 1013 K. Figure 5.1 shows that the performance of both the Sn/Ni and Ni anode SOFCs was very similar when operating on humidified hydrogen. The slight changes on the I-V curves at high current density between the two fuel cells can be attributed to differences in the microstructure of the fuel cells. We would also like to note that the open circuit voltage (OCV) in both cases was very close to the calculated OCV value of 1.1V, indicating no significant fuel crossover.

We have also utilized impedance spectroscopy to measure the losses in the SOFCs. In these experiments, the cell was operated at 1013 K under OCV conditions with hydrogen flowing at the anode and air at the cathode.

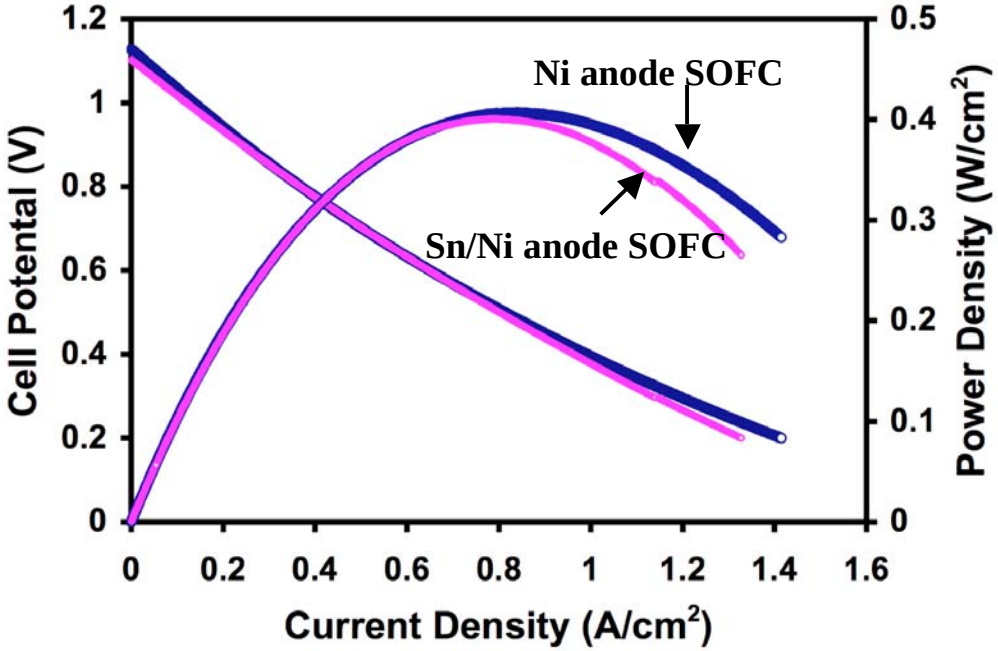

Figure 5.1. A plot of cell potential and power density as a function current density for a Sn/Ni and a Ni anode SOFC when operating on 50sccm H_2/3%H_2O at 740°C.

The frequency of the input voltage signal was varied from 1 MHz to 0.01 Hz. A detailed description of the impedance spectroscopy is provided in Chapter 2. Figure 5.2 shows a Nyquist plot for a Sn/Ni anode and a Ni anode SOFC. The Nyquist plots for both SOFCs show two broad resistance peaks. The resistance peak at lower frequency can be attribute to the anode and the one at the higher frequency to the cathode losses. The resistance across the electrolyte is related to the intercept of the impedance curve with the x-axis at ~ 0.1 Ω/cm^2. Figure 5.2 shows that the electrolyte and the cathode resistance are respectively similar to each other for both the Sn/Ni and Ni anode SOFCs. Figure 5.2 also shows that the anode resistance is slightly higher for a Sn/Ni anode than a Ni anode SOFC. This could be attributed to the fact that the activation barrier for the electron transfer reaction is higher on Sn/Ni than on Ni.

We have also tested the Sn/Ni and Ni anode SOFCs in the direct electrochemical oxidation of methane. Figure 5.3 shows the current density as a function of time for the two different SOFCs. In these experiments the voltage was maintained at 0.6V while the anodes were exposed to a flowrate of 25 sccm of pure CH_4 at 1013 K. Figure 5.3 shows that the Ni anode SOFC had a higher initial current density than the Sn/Ni anode SOFC but deactivated rapidly. On the other hand, the Sn/Ni anode SOFC was significantly more stable than the Ni anode SOFC. The lower initial current density in the case of the Sn/Ni SOFC was not surprising since we have measured (see chapter 7) that the activation barrier for methane decomposition is ~ 30 kJ/mol higher on the Sn/Ni surface alloy catalyst compared to monometallic Ni.

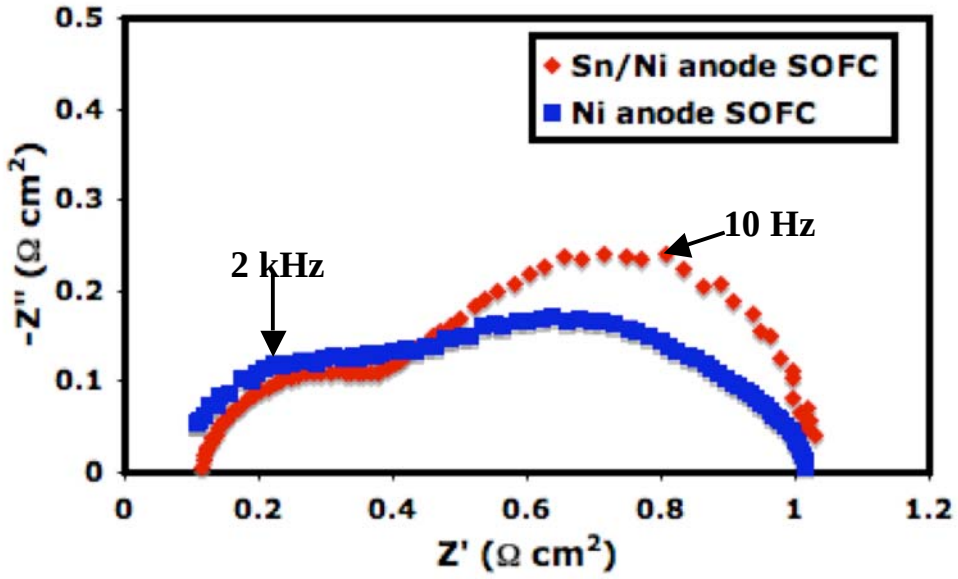

Figure 5.2. Nyquist plots of the real and imaginary components of the impedance at various frequencies across a Sn/Ni anode ans Ni anode SOFC when operating with 50sccm H_2 / 3% H_2O at 1013 K.

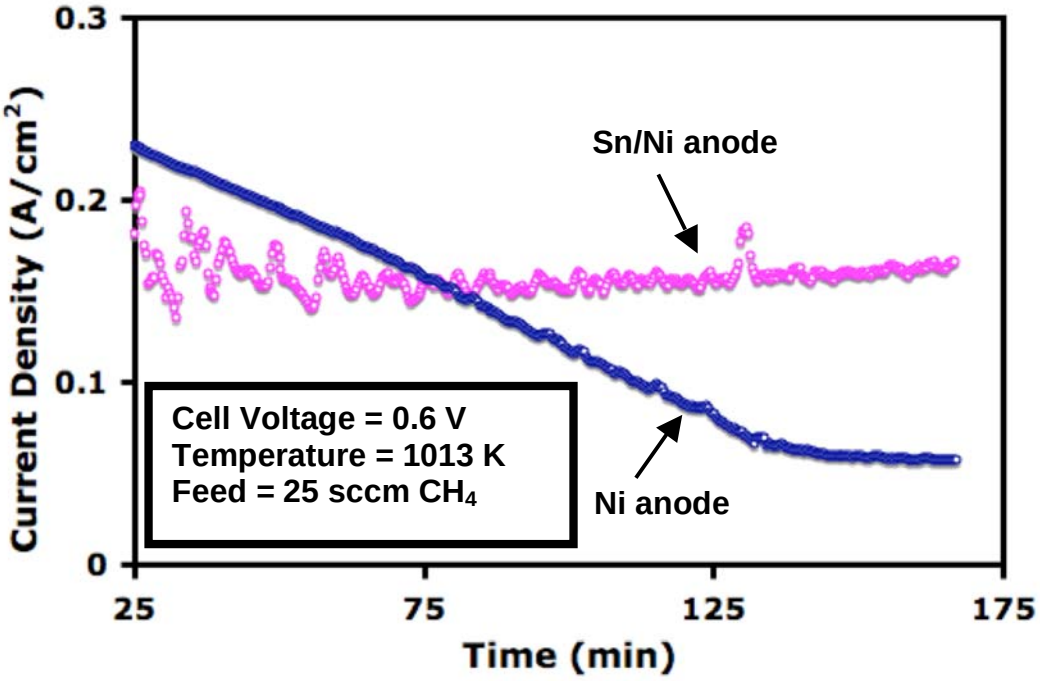

Figure 5.3. A plot of current density as a function of time for a Sn/Ni and a Ni anode SOFC operating under a constant cell voltage of 0.6 V, a temperature of 1013 K and 25 sccm of methane.

We have also tested the performance and stability of the Sn/Ni anode when the SOFC is operated with heavier hydrocarbon fuels such as isooctane. Figure 5.4 shows the measured current density as a function of time for Sn/Ni and Ni anode SOFC operating on a mixture of 5.3% isooctane, 1.8% air diluted in N_2. In these experiments the SOFCs were kept at a constant voltage of 0.5 V and a temperature of 1013 K. Figure 5.4 shows that the Ni-anode SOFC deactivates rapidly when operating with isooctane while the SOFC with a Sn/Ni anode was stable for the duration of the experiment. It is also important to note that the OCV was not recovered for SOFCs with the Ni anode when the fuel was switched back to pure hydrogen. This indicated that the structure of the fuel cell was compromised during the operation on isooctane. On the other hand, the OCV was recovered for the Sn/Ni anode SOFC when switched back to pure hydrogen. It is also important to note that in both, the Sn/Ni and Ni anode SOFCs, gas phase carbon deposits (i.e. carbon deposits formed from gas phase pyrolysis of the fuel) developed inside the alumina tube during the exposure to isooctane. These carbon deposits presented a problem in the long-term operation of the fuel cells due to the pressure induced on the SOFCs by carbon deposits. We alleviated this problem by inserting only a small area of the alumina tube inside of the furnace. This limited the formation of gas phase carbon deposits.

We have also tested the stability of the Sn/Ni anode SOFC under more severe conditions (i.e corresponding to lower oxygen to carbon (O/C) ratios at the anode). For example, we decreased the operating current density from 0.3 A/cm^2 to 0.2 A/cm^2. Decreasing the current density decreases the oxygen flux from the cathode to the anode thus lowering the O/C ratio at the anode.

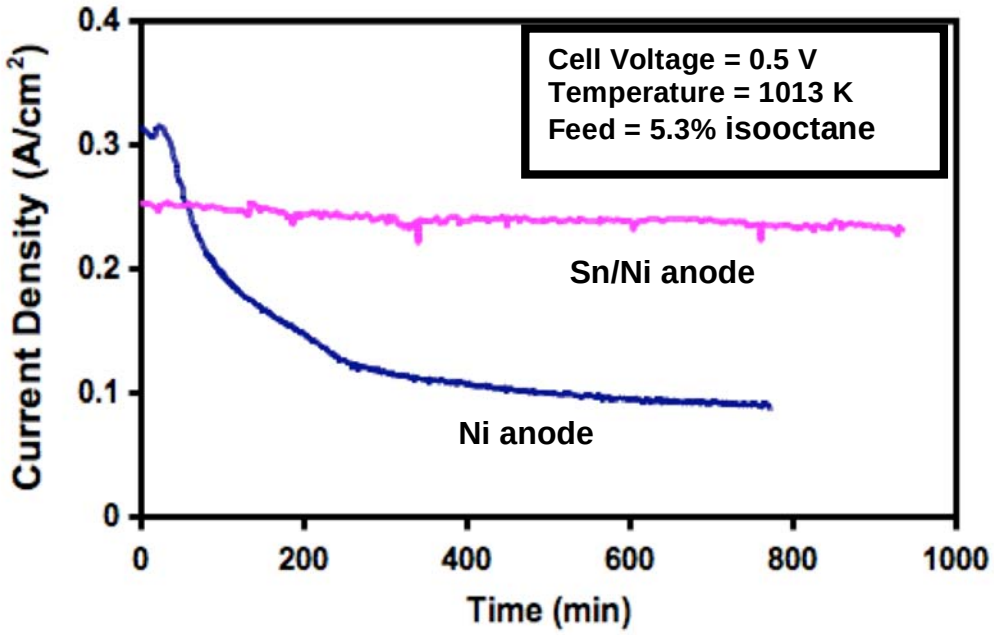

Figure 5.4. A plot of current density as a function of time for a Sn/Ni and a Ni anode SOFC when operating under a constant cell voltage of 0.5 V, a temperature of 1013 K and a mixture of 5.3% isooctane/1.8%air/N_2.

The measured cell voltage as a function of time for a Sn/Ni anode SOFC operating with isooctane as the current density was decreased from 0.3 to 0.2 A/cm^2 is shown in Figure 5.5.

In this process, the cell voltage increased to respond to the decrease in current density but no degradation of the cell voltage was noticed over time for as long as the Sn/Ni anode SOFC was kept under these conditions. Furthermore, we also lowered the O to C ratio by doubling the isooctane partial pressure at the anode. Once again, an increase in the operating voltage occurred to account for the increase in the isooctane partial pressure but no major deactivation of the cell voltage was detected for as long as the Sn/Ni anode SOFC was kept under these conditions. It is also important to note that each time we changed conditions we switched back to hydrogen and were able to recover the OCV. This was a quick indication that no leaks or fractures had occurred to the cell during the process.

Thus far, we have demonstrated through various electrochemical stability tests that Sn/Ni anode SOFCs are more stable than Ni anode SOFCs when operating with various hydrocarbon fuels such as methane and isooctane. In order to fully assess whether carbon poisoning occurred on the Sn/Ni and Ni anode SOFCs, we have characterized these cells using SEM and EDS. In the case of the Ni anode SOFC, SEM and EDS showed that the Ni anode SOFC was completely fractured and disintegrated due to the formation of carbon deposits on the anode see Figure 5.6 a, b, c, d.

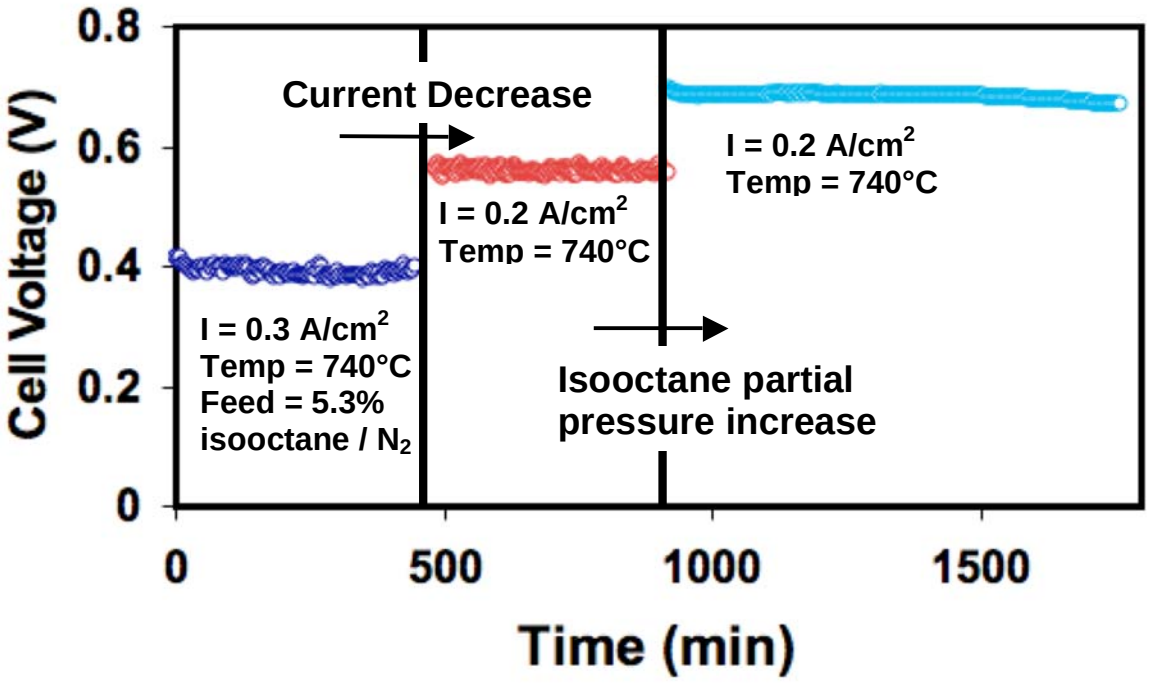

Figure 5.5. A plot of cell voltage as a function of time for a Sn/Ni anode SOFC operating under: a) a current density of 0.3A/cm^2, a temperature of 1013 K and a feed of 5.3% isooctane/N_2 b) a current density of 0.2 A/cm^2, a temperature of 1013 K and a feed of 5.3

Figure 5.6 a and c show the SEM images of the anode/electrolyte interface and the side view of the fuel cell taken after the cell was exposed to isooctane while Figure 5.6c and d show the elemental mapping using EDS of these regions. These results clearly show the large extend of carbon formed at the Ni anode.

Similar studies were conducted on the Sn/Ni anode SOFC after operating with isooctane. Figure 5.7 a, b c show the SEM image of the anode/electrolyte interface of the Sn/Ni anode SOFC and the elemental mapping of various regions of the anode. In this case no fracture or disintegration of the anode was detected. Furthermore EDS mapping showed no signs of carbon deposits at the various regions of the Sn/Ni anode.

Our results demonstrated that Sn/Ni surface alloy anodes were more carbon tolerant than monometallic Ni anodes when operating with methane and isooctane. These results are consistent with our DFT predictions. In the previous chapters, our DFT calculations predicted that Sn/Ni surface alloy might stem from the fact that Sn/Ni surface alloy might be a more carbon tolerant than monometallic Ni since this material favors C-O bond over C-C bond formation and hinders carbon nucleation at the low coordinated sites. [21]

5.4 Conclusions

Herein, we have demonstrated though extensive electrochemical studies that the Sn/Ni surface alloy anode SOFCs are more carbon tolerant than monometallic Ni anode SOFCs when operating on methane and isooctane. This was further corroborated by the characterization of the SOFC after exposure to the various hydrocarbons which showed that the Ni anode SOFCs were completely destroyed by carbon deposits while the Sn/Ni anode SOFC were free of carbon.

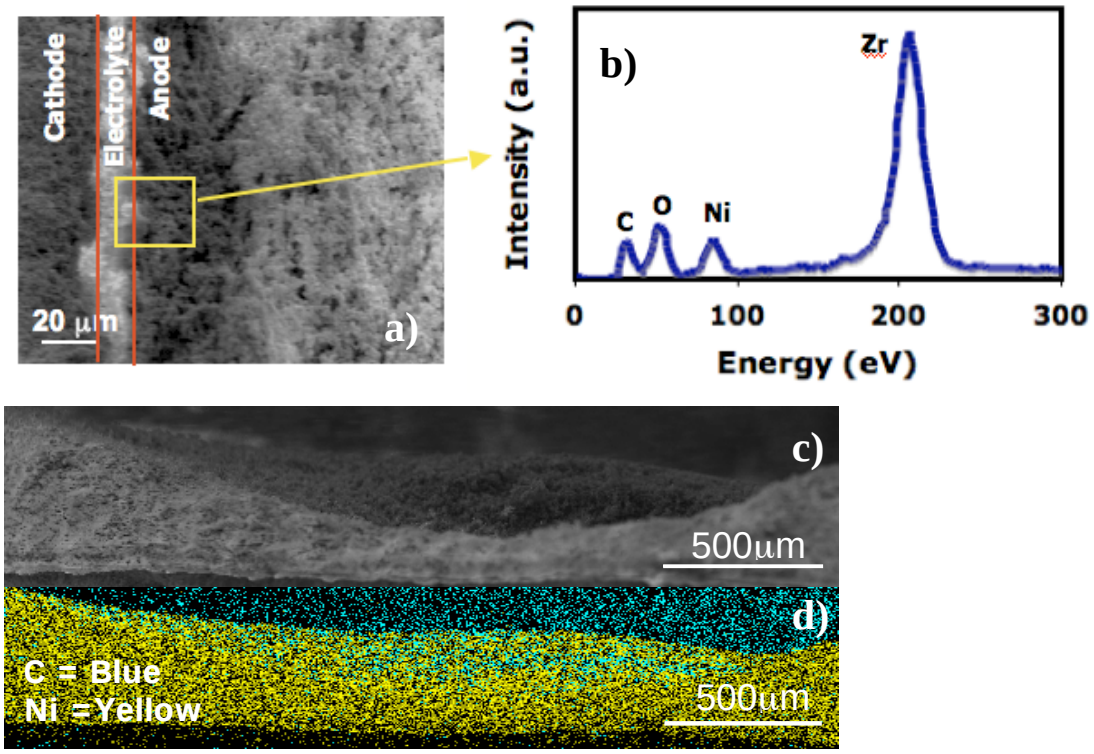

Figure 5.6. a) A scanning electron micrograph of Ni anode SOFC after exposure to isooctane at 740°C. b) EDS plot when probing a region at the electrolyte/anode interface on the Sn/Ni anode SOFC. c) A side view of the Ni anode SOFC obtained using SEM. d) EDS mapping of the side view of the cell shown in c).

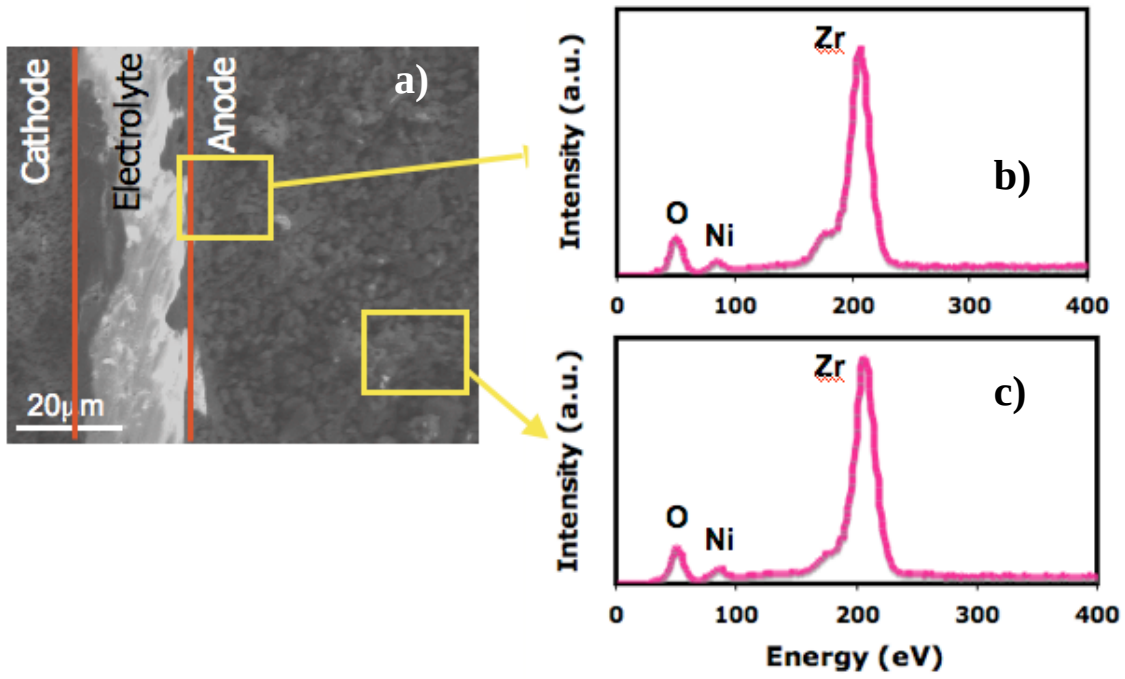

Figure 5.7. a) A scanning electron micrograph of Sn/Ni anode SOFC after exposure to isooctane at 740°C. b) EDS plot when probing a region close to the electrolyte/anode interface c) EDS plot when probing a region away from the electrolyte/anode interface.

5.5 References

1. Atkinson, A., et al., *Advanced anodes for high-temperature fuel cells.* Nature Materials, 2004. **3**(1): p. 17-27.

2. Kim, H., et al., *Cu-Ni cermet anodes for direct oxidation of methane in solid-oxide fuel cells.* Journal of the Electrochemical Society, 2002. **149**(3): p. A247-A250.

3. Lin, Y.B., et al., *Direct operation of solid oxide fuel cells with methane fuel.* Solid State Ionics, 2005. **176**(23-24): p. 1827-1835.

4. Mogensen, M. and K. Kammer, *Conversion of hydrocarbons in solid oxide fuel cells.* Annual Review of Materials Research, 2003. **33**: p. 321-331.

5. Morel, B., et al., *Anode-supported SOFC model centered on the direct internal reforming.* Journal of the Electrochemical Society, 2005. **152**(7): p. A1382-A1389.

6. Murray, E.P., et al., *Direct solid oxide fuel cell operation using isooctane.* Electrochemical and Solid State Letters, 2006. **9**(6): p. A292-A294.

7. Timmermann, H., et al., *Internal reforming of methane at Ni/YSZ and Ni/CGO SOFC cermet anodes.* Fuel Cells, 2006. **6**(3-4): p. 307-313.

8. Triantafyllopoulos, N.C. and S.G. Neophytides, *The nature and binding strength of carbon adspecies formed during the equilibrium dissociative adsorption of CH4 on Ni-YSZ cermet catalysts.* Journal of Catalysis, 2003. **217**(2): p. 324-333.

9. Weber, A., et al., *Oxidation of H-2, CO and methane in SOFCs with Ni/YSZ-cermet anodes.* Solid State Ionics, 2002. **152**: p. 543-550.

10. Nguyen, Q.M. and T. Takahashi, *Science and technology of ceramic fuel cells.* 1995, New York: Elsevier Science. 366.

11. Primdahl, S. and M. Mogensen, *Mixed conductor anodes: Ni as electrocatalyst for hydrogen conversion.* Solid State Ionics, 2002. **152**: p. 597-608.

12. McIntosh, S., et al., *An examination of carbonaceous deposits in direct-utilization SOFC anodes.* Journal of the Electrochemical Society, 2004. **151**(4): p. A604-A608.

13. Gorte, R.J. and J.M. Vohs, *Novel SOFC anodes for the direct electrochemical oxidation of hydrocarbons.* Journal of Catalysis, 2003. **216**(1-2): p. 477-486.

14. Lee, S.I., J.M. Vohs, and R.J. Gorte, *A study of SOFC anodes based on Cu-Ni and Cu-Co bimetallics in CeO_2-YSZ.* Journal of the Electrochemical Society, 2004. **151**(9): p. A1319-A1323.

15. McIntosh, S., J.M. Vohs, and R.J. Gorte, *Impedance spectroscopy for the characterization of Cu-Ceria-YSZ anodes for SOFCs.* Journal of the Electrochemical Society, 2003. **150**(10): p. A1305-A1312.

16. McIntosh, S., et al., *Effect of polarization on and implications for characterization of LSM-YSZ composite cathodes.* Electrochemical and Solid State Letters, 2004. **7**(5): p. A111-A114.

17. Zhan, Z.L. and S.a. Barnett, *An octane-fueled olid oxide fuel cell.* Science, 2005. **308**(5723): p. 844-847.

18. Zhan, Z.L. and S.a. Barnett, *Use of a catalyst layer for propane partial oxidation in solid oxide fuel cells.* Solid State Ionics, 2005. **176**(9-10): p. 871-879.

19. Zhou, Z.F., et al., *Direct oxidation of jet fuels and Pennsylvania crude oil in a solid oxide fuel cell.* Journal of Power Sources, 2004. **133**(2): p. 181-187.

20. Nikolla, E., et al., *Controlling carbon surface chemistry by alloying: Carbon tolerant reforming catalyst.* Journal of the American Chemical Society, 2006. **128**(35): p. 11354-11355.

21. Nikolla, E., J. Schwank, and S. Linic, *Promotion of the long-term stability of reforming Ni catalysts by surface alloying.* Journal of Catalysis, 2007. **250**(1): p. 85-93.

22. Nikolla, E., J. Schwank, and S. Linic, *Hydrocarbon steam reforming on Ni alloys at solid oxide fuel cell condition.* Catalysis Today, 2008. **136**(3-4): p. 243-248.

CHAPTER 6

METHANE STEAM REFORMING KINETICS ON SN/NI SURFACE ALLOY

6.1 Summary

In this chapter, a kinetic assessment of the mechanism of methane steam reforming on Sn/Ni surface alloy and monometallic Ni supported on yttria stabilized zirconia (YSZ) is provided. In the previous chapters, we demonstrated that Sn/Ni surface alloy is a more carbon tolerant catalyst than monometallic Ni. In this chapter, we have employed kinetic studies and isotopic-labeling experiments combined with DFT calculations to develop a kinetic model (i.e. the rate order, activation energy barrier, and the rate limiting-step) for methane steam reforming on Sn/Ni alloy. We find that the reaction rate on Sn/Ni surface alloy is first order with respect to methane and zero order with respect to water. Furthermore, isotopic labeling experiments showed that the activation of the C-H bond activation is the rate-limiting step in this process on Sn/Ni. Similar observations were obtained for Ni/YSZ. The main differences between Sn/Ni and Ni catalysts were: (i) the overall activation energy barrier was ~ 30 kJ/mol higher on Sn/Ni/YSZ than on Ni/YSZ and (ii) the pre-exponential factor for methane steam reforming was 20 times higher on Sn/Ni/YSZ than on Ni/YSZ.

6.2 Introduction

In the previous chapters we have demonstrated that Sn/Ni surface alloy is a more carbon tolerant steam reforming catalyst than monometallic Ni.[1-3] DFT calculations showed that there were two likely mechanisms that led to the improved performance of Sn/Ni: (i) Sn atoms occupied the low coordinated sites on the Ni particles preventing the nucleation of carbon and (ii) Sn lowered the rate of the oxidation of the carbon atoms relative to the rates of the C-C bond formation. In this chapter, we have employed kinetic studies along with isotopic labeling experiments to develop a kinetic model (i.e. the rate order, activation energy barrier, and the rate limiting-step) for methane steam reforming on Sn/Ni surface alloy. Our analysis is supported by DFT calculations on model systems.

The kinetics of methane steam reforming on supported monometallic Ni catalysts have been studied by many researchers.[4-12] Although there have been many controversies, recent theoretical and experimental contributions have shown some consistent results. For example, Bengaard et al. have utilized a combined theoretical and experimental approach to develop a mechanism for steam reforming of methane on Ni.[4] They have shown that methane steam reforming is structure sensitive and under-coordinated Ni surface sites such as step/edge sites are more active than the Ni terrace sites. They have also demonstrated that the rate-limiting step in this process is C-H bond activation in methane. This is consistent with the recent experimental conclusions of Wei and Iglesia that the rate-limiting step in methane steam reforming on Ni/MgO catalysts is the C-H bond activation in methane. Wei and Iglesia also demonstrated that the rate of steam reforming is first order with respect to the methane partial pressure and does not depend on the partial pressure of water.[8]

6.3 Experimental methods

A detailed description of the methods utilized to synthesize the support (8 mol% yttria stabilized zirconia) and the active catalysts is provided in Chapter 2. The Ni metal loading was 15 wt% with respect to the total catalyst (Ni plus YSZ). The Sn/Ni/YSZ catalyst was synthesized by impregnating NiO/YSZ with Sn chloride ($SnCl_2*4H_2O$) via the incipient wetness technique. The nominal Sn loading was about 1 wt% with respect to the Ni content in the catalyst. All catalysts were reduced at 1173 K for 3 hours using 30% H_2/N_2.

Kinetic studies were conducted isothermally in a packed bed quartz reactor system. The diameter of the quartz reactor was 0.375 inches. The set-up included a set of mass flow controllers, a pair of thermocouples (inside and outside the reactor), and a syringe pump for water delivery. The water lines were heated to 473 K to avoid condensation. The reactor effluent was analyzed using a Varian gas chromatograph (Varian CP 3800) equipped with thermal conductivity detectors (TCD) and a flame ionization detector (FID). Approximately 0.01g of Ni/YSZ and Sn/Ni/YSZ catalysts with particles sizes of 150-200 μm were diluted in 0.5g of quartz powder (250-400μm) and loaded in the packed bed reactor. The rates of methane steam reforming were measured as the temperature was varied from 923-1073 K. The absence of diffusion and mass transport limitations was confirmed by analyzing the reaction rates as a function of the total space velocity.

Single point BET analysis was utilized to measure the surface area of the YSZ support via N_2 physisorption. The physisorption experiments were conducted using Quatachome's ChemBet 3000 equipped with thermal conductivity detectors (TCD). The active surface area and dispersion of the Ni/YSZ and Sn/Ni/YSZ catalysts was measured

using H_2 chemisorption at 373 K. The chemisorption experiments were conducted using Micromeritics ASAP 2020.

Thermal gravimetric analysis (TGA) experiments were performed with a TA instruments thermo-gravimetric analysis (TGA Q500). Initially approximately 0.2 g of catalyst was reduced under 30% H_2/N_2 at 1073 K for 2 hours. Once reduced the catalysts were cooled to room temperature while exposed to pure nitrogen. Following the reduction procedure the catalysts were exposed to dry methane and the temperature was ramped to 1073 K at a set heating rate. The weight of the sample was measured as the temperature increased and methane decomposed and deposited carbon on the surface of the catalyst. TGA was also utilized to study the reduction and oxidation behavior of the catalysts. In these experiments the catalysts were initially reduced under 30% H_2/N_2 at 1073 K for 2 hours, cooled to room temperature under nitrogen and exposed to air as the temperature was ramped to 1073 K. Once oxidized, the catalysts were cooled and re-reduced using the same protocol as described above.

The Dacapo pseudo-potentials plane wave code (http://www.camp.dtu.dk) was employed for all Density Functional Theory (DFT) calculations. To model Ni surface we used two different model systems, Ni(111) and Ni(211). These model systems allow us to explore two representative active sites, mainly under-coordinated step-edge sites on the (211) surface and close packed sties on the (111) surface. For model systems with the (111) surface termination, we used a 3x3 supercell with 4 layers of metal atoms. The calculations for the (211) surface termination were performed using slabs with 9 layers of metal in 1x3 supercells. Our approach was to find a set of parameters that ensured the relative convergence, i.e., the convergence of the relative energies of various structures.

With this set of parameters we have been able to reproduce various properties such as carbon atom adsorption energies, oxygen adsorption energies, graphene sheet adsorption energy on Ni(111), and activation barrier for the attachment of a C atom to the graphene sheet over Ni(111) reported previously by others.[4, 13-15] The convergence for the (111) surface was obtained with 18 special Chadi-Cohen *k*-points to sample the Brillouin zone. For the (211) surface, we used Monkhorst-Pack mesh with a 3x3x1 *k*-point grid to sample the Brillouin zone. Adsorbates were adsorbed on one side of a slab. Approximately 15 Å of vacuum separated the slabs, and a dipole-correction scheme was employed to electro-statically decouple the slabs. Electron exchange correlation effects were described using the generalized gradient approximation (GGA) with the Perdew–Wang 91 (PW91) functional.[16-18] Vanderbilt pseudo-potentials were employed to describe core electrons.[19] The density of valence electrons was determined self-consistently by iterative diagonalization of Kohn-Sham Hamiltonian using Pulay mixing of densities. The plane wave basis set used to describe the one-electron states was cut off at 350 eV. An electronic temperature (k_bT) of 0.1 was utilized during calculations with the final results extrapolated to 0 K. In the geometry optimization calculations on the (111) surface termination, the two top substrate layers and adsorbates were allowed to relax. On the (211) termination, the top six substrate layers and adsorbates were allowed to relax. The forces were minimized to 0.05eV/Å.

To model the Sn/Ni surface alloy we have employed identical Ni(111) slabs with a number of Sn atoms, equivalent to 1/9 and 2/9 ML, displacing Ni atoms in the surface layer of Ni. We have previously established using x-ray photoelectron spectroscopy (XPS) and electron energy loss microscopy (EELS) that Sn preferentially segregates to

the surface layers on Ni, i.e., that the surface alloy structures are the most stable Sn/Ni configurations for Ni particles impregnated with small amounts of Sn (between 1 - 3 wt % of Sn with respect to Ni for Ni particles with the diameter between 40-50 nm). Furthermore, DFT calculations also showed that the model surface alloy structures, shown in Figure 6.1 with Sn atoms dispersed in the top layer, have lower formation energies relative to Sn displacing Ni atoms from the slab bulk, Sn adsorbing on the surface of Ni, or Sn assembling in segregated pure Sn phases.

6.4 Results and Discussions

6.4.1 Kinetic Studies

The activation energy and the reaction order for methane steam reforming (rxn 1) were determined using differential reactor studies. The steam reforming reactions were operated at low methane conversions far from equilibrium. The approach to equilibrium (η) was calculated using equation 1.

$$CH_4 + H_2O \leftrightarrow CO + 3H_2 \qquad \text{rxn 1}$$

$$\eta = \frac{[H_2]^3[CO]}{[CH_4][H_2O]} * \frac{1}{K_{eq}} \qquad \text{eqn 1}$$

Where $[CH_4]$, $[H_2O]$, $[CO]$, $[H_2]$ and are the measured concentration of reactants (CH_4, H_2O) and products (CO, H_2) respectively and K_{eq} is the equilibrium constant for methane steam reforming at relevant conditions. The approach to equilibrium at various conditions was less than 0.01. Therefore since the approach to equilibrium is small, the experimental measured rates are the same as the forward rates for methane steam reforming (see eqn 2).

$$rate_f = \frac{rate_n}{(1-\eta)} \qquad \text{eqn 2}$$

Where $rate_n$ is the net reaction rate, $rate_f$ is the forward reaction rate and η is the approach to equilibrium.

Prior to obtaining kinetic data, rigorous tests were conducted to eliminate diffusion and mass transport limitations. One approach was to vary the catalyst (metal plus support) particle size from 800 to 150 μm and measure the change in the reaction rate.[20, 21] We found that the rate was constant for the catalyst particle sizes between 150-300μm, confirming the absence of the internal diffusion limitations. Furthermore the catalyst bed was also diluted with quartz powder until no changes in rate were observed for a particular flowrate. We also confirmed the absence of diffusion limitations by analyzing the overall rates as the total space velocity changed. Figure 6.1 a and b show the plots of methane steam reforming rates as the function of space velocity for a Sn/Ni/YSZ and Ni/YSZ catalyst. These results clearly demonstrate there were no mass transport and diffusion limitations. These tests were conducted for every temperature to ensure the absence of the diffusion artifacts.

The reaction orders with respect to methane and water for methane steam reforming on Sn/Ni/SYZ were determined by measuring the change in rate as a function of the partial pressures of CH_4 and H_2O respectively according to equations 3 and 4. Equation 4 is obtained from taking the log of the right and left side of equation 3.

$$rate = k * [CH_4]^a * [H_2O]^b \qquad \text{eqn 3}$$

$$\ln(rate) = \ln(k) + a * \ln[CH_4] + b * \ln[H_2O] \qquad \text{eqn 4}$$

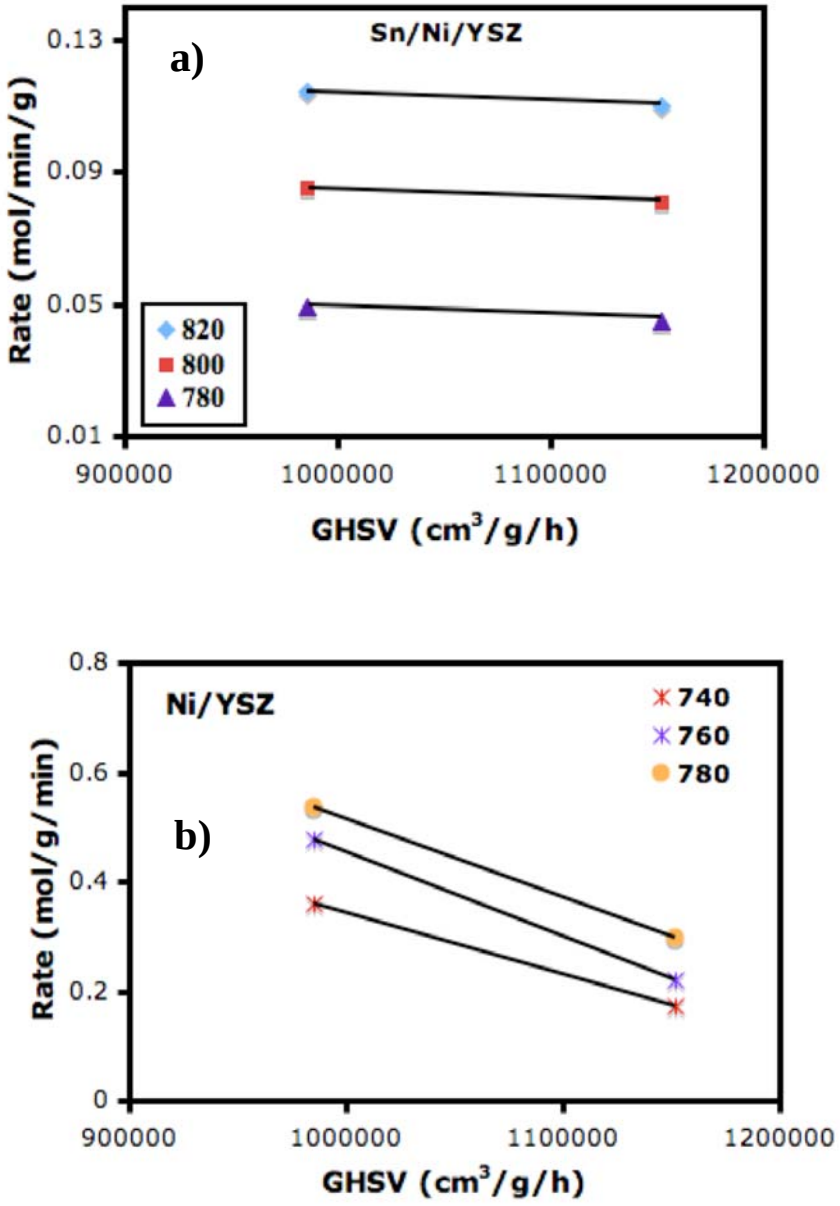

Figure 6.1. Methane steam reforming reaction rates as a function of the gas hourly space velocity (GHSV) for a) Sn/Ni/YSZ and b) Ni/YSZ at different operating temperatures.

Where k is the rate constant for the reaction, $[CH_4]$ and $[H_2O]$ are the concentrations for methane and water, a and b are the reaction orders with respect to methane and water respectively.

Figures 6.2a shows the plot of ln (rate) as a function of the partial pressure of methane during steam reforming of methane on Sn/Ni/YSZ at 1073 K. In these experiments, the partial pressure of methane was varied from 0.2 - 0.6 atm, as the partial pressure of water was kept constant at 0.39 atm. Figure 6.2a shows that the ln (rate) varies linearly with respect to the partial pressure of methane with a slope of ~ 1, indicating that the rate of steam reforming on the Sn/Ni/YSZ catalyst is first order with respect to methane. Figure 6.2b shows the dependence of the rate on the partial pressure of water on Sn/Ni/YSZ at 1073 K while keeping partial pressure of methane at 0.39 atm. The plot shows that the rate of methane steam reforming on Sn/Ni/YSZ does not depend on the partial pressure of water. Similar results were also obtained for the Ni/YSZ catalyst. Figure 6.3a and b show the change in the rate of steam reforming as a function of the partial pressure of methane and water respectively. As in the case of Sn/Ni/YSZ, the methane stem-reforming rate is first order with respect to the methane partial pressure and does not depend on the partial pressure of water.

Our results also show that as we varied the methane conversion by changing the flowrate or temperature, the order of the forward rate with respect to H_2O and CH_4 did not change on either catalyst.

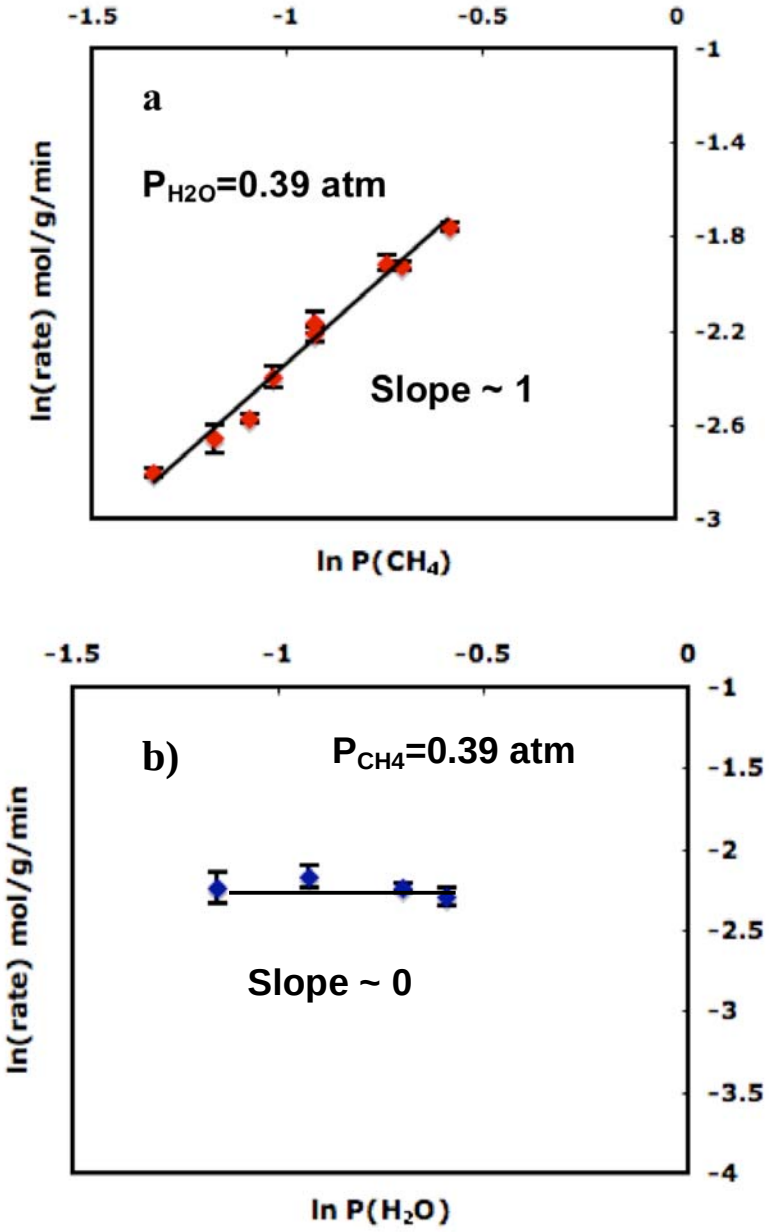

Figure 6.2. a) A plot of ln (reaction rate) as a function of ln (P_{CH4}) for a Sn/Ni/YSZ catalyst under steam reforming conditions at 1073 K and a constant partial pressure of water of 0.39 atm. b) A plot of ln (reaction rate) as a function of ln (P_{H2O}) for a Sn/Ni/ YSZ catalyst under steam reforming conditions at 1073 K and a constant partial pressure of methane of 0.39 atm.

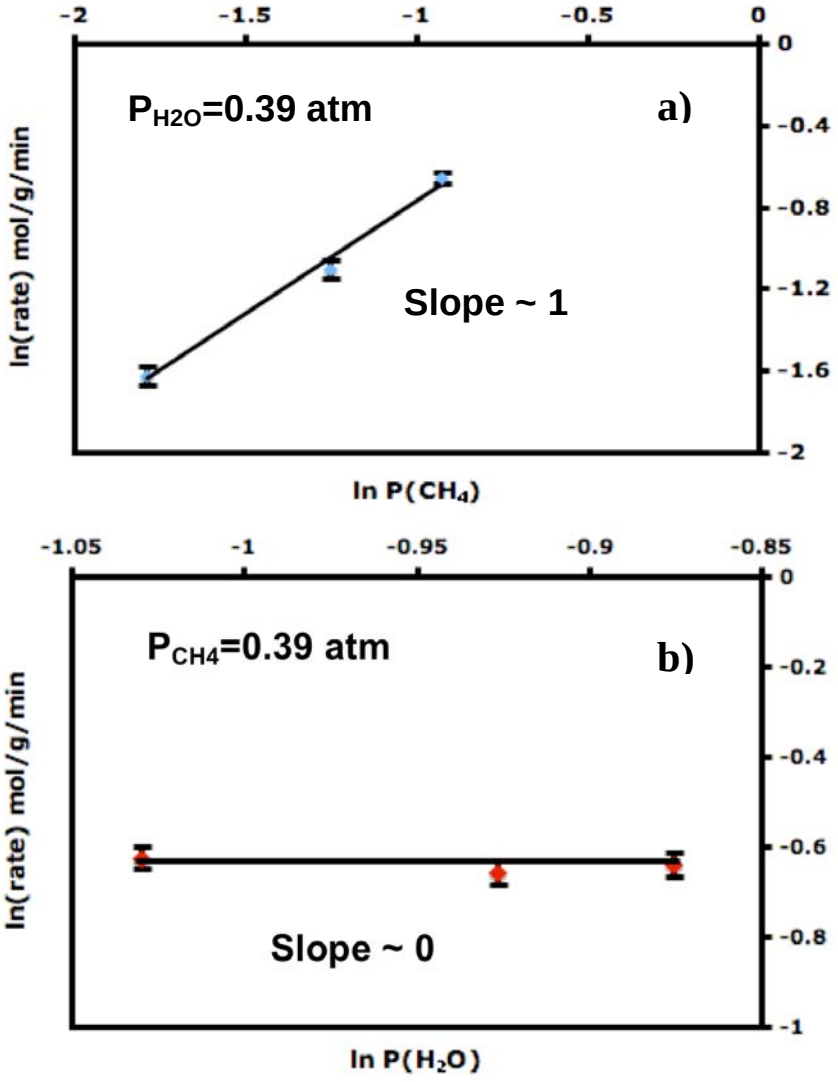

Figure 6.3. a) A plot of ln (rate) as a function of ln (P_{CH4}) for a Ni/YSZ catalyst under steam reforming conditions at 1013K and a fixed partial pressure of water of 0.39 atm. b) A plot of ln (rate) as a function of ln (P_{H2O}) for a Ni/YSZ catalyst under steam reforming conditions at 1013 K and a fixed partial pressure of methane of 0.39 atm.

Since higher CH_4 conversion would lead to higher partial pressures of the reaction products, these observations imply that, for the conditions explored in this paper, the forward reaction rate is not sensitive to the changes in the partial pressure of the reaction products for either catalyst, and that the surface coverage of product species (or surface intermediates which are precursors for the reaction products) on active sites does not change significantly. If this was not the case, we would have seen a measurable deviation in the reaction orders as a function of the change in conversion. These conclusions are consistent with the results of our DFT calculations, which showed that the adsorption energies of CO, H_2O, CO_2, and H_2 in their lowest energy configurations (e.g., dissociated or molecular) on under-coordinated sites of the Ni(211) surface are -1.7, -1.4, 0.2, -0.8 eV respectively. The adsorption energies are even lower for close packed Ni surfaces and for all sites on the Sn/Ni surfaces. These adsorption energies are insufficient to keep the species on the surface in significant concentrations under the high temperature conditions ($T > 973$ K), i.e, the Gibbs free energy of adsorption is positive. Based on the presented experimental results and the results of DFT calculations, we suggest that for both catalysts, the catalyst surface is approximately free of adsorbates under steady state conditions and the overall rate is controlled only by the rate of the dissociation of CH_4. Identical observations were made previously for Ni/MgO catalysts. [8]

The overall activation energy barrier for methane steam reforming on the Sn/Ni/YSZ and the Ni/YSZ catalysts was obtained by measuring methane turnover frequencies (TOF) as a function of temperature. Prior to each measurement, the absence of diffusion and mass transport artifacts was determined using the protocol described above. Figure 6.4 shows a plot of the ln (TOF) as a function of temperature for Ni/YSZ

and Sn/Ni/YSZ catalysts. The activation barrier was determined from the slope of the line of ln (TOF) vs (1/temperature) according to equations 4 and 5.

$$rate = A * \exp(-\frac{E_a}{RT}) * [CH_4] \qquad \text{eqn 4}$$

$$\ln(rate) = \ln(A) + \frac{(-E_a)}{RT} + \ln[CH_4] \qquad \text{eqn 5}$$

The activation energy for steam reforming of methane on Ni/YSZ was measured to be 101 kJ/mol. This is consistent with activation energies for this reaction on supported Ni catalysts reported by others. [8, 10, 22] On the other hand, the activation energy on Sn/Ni/YSZ was measured to be ~ 132 kJ/mol. Furthermore, the pre-exponential factor for Sn/Ni/YSZ was ~20 higher than the one for Ni/YSZ. We also found that measured reaction rates and the methane turnover frequencies were lower for Sn/Ni/SYZ than Ni/YSZ indicating that alloying Ni with Sn had resulted in a less active catalyst than monometallic Ni.

We have also utilized thermal gravimetric analysis (TGA) to obtain the activation barrier for methane dissociation on Sn/Ni/YSZ and Ni/YSZ catalysts. In these experiments, the change in the weight of the catalyst was measured as the catalyst was exposed to dry methane and the temperature was ramped from 298 K to 1173 K. Figure 6.5a shows a plot of the weight gain for the Sn/Ni/YSZ and Ni/YSZ catalysts as a function of temperature under a 1 atm pressure of methane. The increase in the weight of the catalysts is a consequence of the formation of carbon deposits during methane decomposition (rxn 1).

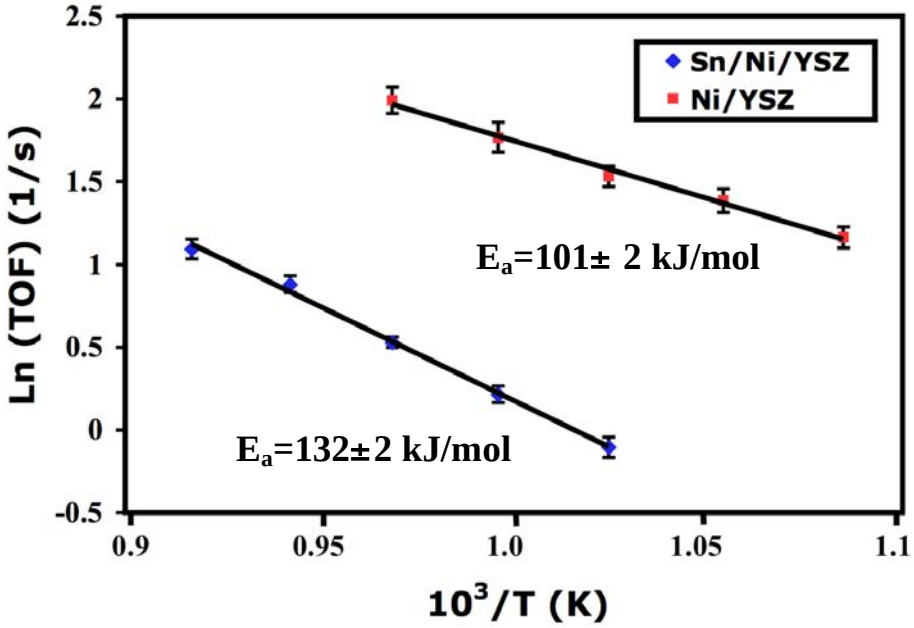

Figure 6.4. A plot of the natural log of the turnover frequency of methane as a function of the inverse temperature for 1wt% Sn/Ni/YSZ and Ni/YSZ catalysts.

$$CH_4 + * \rightarrow C* + 2H_2 \qquad \text{rxn 1}$$

Figure 6.5a shows that methane decomposes at lower temperature on Ni than on Sn/Ni. We have also plotted in Figure 6.5b the measured rate of weight gain as a function of temperature, which is a measure of the rate of methane decomposition on the catalyst surface. Figure 6.5b shows that the rate curve is broader on Sn/Ni compared to Ni. We interpret this in terms of multiple reaction channels (different sites) for methane decomposition on Sn/Ni. This supports the conclusions of our previous characterization studies which showed that in the Sn/Ni catalyst, the Sn atoms are dispersed in the surface layers of Ni particles forming a large number of geometrically and electronically diverse surface sites. Careful inspection of Figure 6.5b also shows that for Sn/Ni there is a small shoulder in the rate curve, appearing at temperature just below 500 K, which overlaps with the peak of the rate curve for Ni. This suggests that there are a small number of sites on Sn/Ni that are similar to the sites on Ni in its ability to activate the C-H bonds in methane. However, the number of these sites is very small, and the sites are not responsible for the main methane decomposition channels, which are moved to higher temperatures for Sn/Ni compared to monometallic Ni.

The activation barriers for methane decomposition on Sn/Ni/YSZ and Ni/YSZ were obtained using the Redhead analysis. In this analysis we have assumed that the rate of methane decomposition is first order with respect to the partial pressure of methane and n^{th} order with respect to the concentration of empty sites (*) as shown by eqn 6.

$$rate = -\frac{d(*)}{dt} = A_a P_{CH_4} [*]^n \exp(\frac{-E_A}{RT}) \qquad \text{eqn 6}$$

where A_a is the pre-exponential factor for adsorption of methane, P_{CH4} is the partial pressure of methane, [*] is the concentration of the empty sites, E_a is the activation energy for methane decomposition, R is the gas constant and T is the temperature.

In the Redhead analysis, T is set to vary linearly with time ($T = T_0 + \beta t$ where β is the heating rate) and the maximum of adsorption rate is assumed to occur when $\frac{dr}{dT} = 0$ at a temperature Tp (the temperature of the maximum in the dissociative adsorption curve). We can insert the rate expression in equation 6 into $\frac{dr}{dT} = 0$ and obtain an expression, which relates the activation energy for methane decomposition to the peak temperature of the TGA plot and the heating rate as shown in equation 7.

$$A_a n[*]^{n-1} P_{CH4} \exp(\frac{-E_A}{RT_p}) = \frac{\beta E_A}{RT_p^2} \qquad \text{eqn 7}$$

If we conduct an experiment with a heating rate of 5 K/min under a partial pressure of CH_4 of 1 atm, and assume that A_a is 10^5 1/s/atm [8] and the reaction order with respect to the concentration of free sites (n) is 1, then using equations 7 we obtain an activation barrier for methane decomposition of ~132 kJ/mol on Sn/Ni/YSZ and 103 kJ/mol on Ni/YSZ.

If we assume that the reaction order with respect to the concentration of free sites is 2, and the fraction of free sites is 0.4 then the activation barriers become ~130 kJ/mol and 101 kJ/mol for Sn/Ni/YSZ and Ni/YSZ respectively. These results indicate that irrespective of the reaction order with respect to the free sites and the fraction of the free sites the activation barrier for methane dissociation is ~ 30 kJ/mol higher on Sn/Ni/YSZ than on Ni/YSZ.

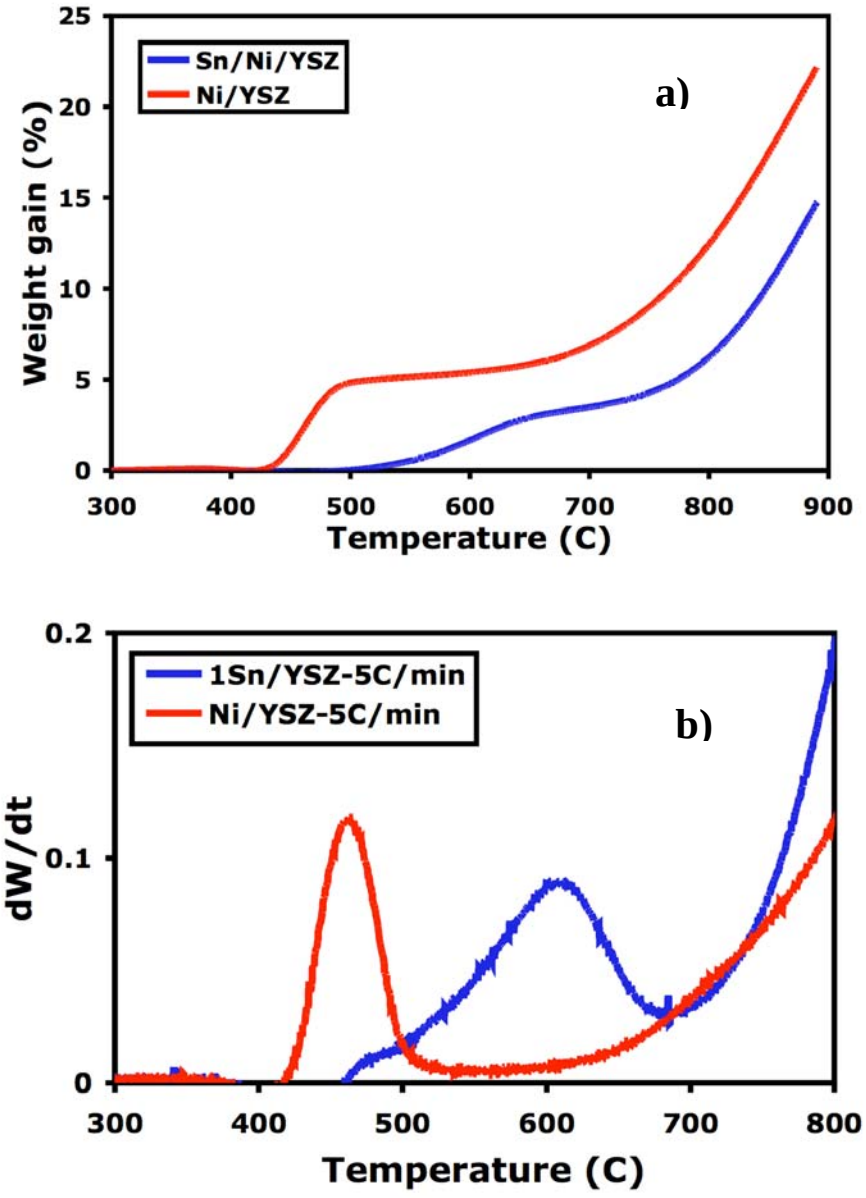

Figure 6.5. a) The percent weight gain of the catalyst as a function of temperature during methane decomposition on Sn/Ni/YSZ and Ni/YSZ catalysts. b) The rate of methane decomposition versus temperature for the same catalysts as in Figure 6.5a.

This is consistent with the difference in the overall activation barrier for steam reforming on Sn/Ni as compared to monometallic Ni obtained from the kinetic studies presented above.

The difference in the activation barriers for methane steam reforming on Sn/Ni and Ni can be attributed to either geometric site poisoning by Sn which results in the change in the nature of the active sites or the change in the rate-limiting step of the process due to alloying between Sn and Ni. Since TGA experiments showed that the difference in the activation barrier for methane decomposition on Sn/Ni and Ni was similar to the one for methane steam reforming on these catalysts, this suggests that the rate-limiting step for both these processes on both catalysts is methane activation. To further verify these observations we have utilized isotopic-labeling experiments to identify the rate limiting step for methane steam reforming on Sn/Ni and Ni.

6.4.2 Isotope Labeling Studies

It has been demonstrated by many researchers that C-H bond activation in methane is the rate-limiting step for methane steam reforming on supported monometallic Ni catalysts.[4, 8, 23] In order to determine whether methane activation is also the rate limiting step in methane steam reforming on Sn/Ni, we have employed isotope-labeling experiments. In these experiment, the reaction rates were measured as CH_4 was replaced by CD_4. According to the kinetic isotope effect, if CH_4 activation is the rate-limiting step for methane steam reforming on Sn/Ni, the rate of the reaction should decrease as CH_4 is replaced by CD_4. This phenomenon can be explained using the transition state theory and the difference in the vibration zero point energies (ZPE) between the reactant and

transition states in CH_4 and CD_4 activation. For example, if we assume that the rates of CH_4 and CD_4 steam reforming are fist order with respect to CH_4 and CD_4 respectively (see equation 6) and that the concentrations of CH_4 and CD_4 and the pre-exponential factors are the same for both CH_4 and CD_4 steam reforming, then we can express the ratio between the CH_4 and CD_4 steam reforming reaction rates as shown by equation 7.

$$\frac{rate_{CH_4}}{rate_{CD_4}} = \frac{k_{CH_4}[CH_4]}{k_{CD_4}[CD_4]} \qquad \text{eqn 6}$$

$$if\,[CH_4] = [CD_4]$$

$$\frac{rate_{CH_4}}{rate_{CD_4}} = \frac{k_{CH_4}}{k_{CD_4}} = \exp\frac{-(E_{a_{CH4}} - E_{a_{CD4}})}{k_B T} \qquad \text{eqn 7}$$

Furthermore we can calculate the activation energies for CH_4 and CD_4 activation from the difference in the total energy at 0 K between the reactant and transition states as shown by equations 8 and 9. The total energy at 0K has two components: the electronic energy and the zero point energy due to vibrational motion of the molecule at 0 K.

$$E_{a_{CH4}} = E_{0-Trans} - E_{0-React} = E_{elect-Trans} + ZPE_{Trans} - E_{elect-React} - ZPE_{React} \qquad \text{eqn 8}$$

$$E_{a_{CD4}} = E_{0-Trans} - E_{0-React} = E_{elect-Trans} + ZPE_{Trans} - E_{elect-React} - ZPE_{React} \qquad \text{eqn 9}$$

where $E_{0\text{-Tans}}$ and $E_{0\text{-Ract}}$ are the energies for the reactant and transition states at 0 K, $E_{elect\text{-}trans}$ and $E_{elect\text{-}Ract}$ are the electronic energies for the reactant and transition states and ZPE_{Trans} and ZPE_{React} are the zero point energies for the transition and reactant states resulting from the vibrational motion of the system. If we assume that the change in the electronic energies between the reactant and transition states for CH_4 and CD_4 activation is similar, then the difference in the activation barriers for CH_4 and CD_4 will only stem from the difference in the ZPEs. The ZPEs can be calculated from the contributions of all the vibrational modes of the system at 0 K. In the reactant states, there exist 4 vibrational

modes for both CH_4 and CD_4 as a result of the C-H and C-D bond vibrations respectively. On the other hand, in the transition state one vibration mode is converted to a translation mode thus resulting in 3 total vibration modes for CH_4 and CD_4 transition states. Equation 10 shows the difference in the ZPEs between the transition state (ZPE_T) and reactant state (ZPE_R) calculated from the vibrational frequency of the C-H or C-D bond.

$$ZPE_T - ZPE_R = \sum_{i=1}^{n-1} \frac{1}{2} h\nu - \sum_{i=1}^{n} \frac{1}{2} h\nu = -\frac{1}{2} h\nu \qquad \text{eqn 10}$$

Where h is the Planck constant, n is the number of the vibrational modes at the reactant states and ν is the vibrational frequency.

If we incorporate equation 10 into the rate expression in equation 7, we can relate the CH_4 and CD_4 steam reforming reaction rates to the ZPEs as follows.

$$\frac{rate_{CH_4}}{rate_{CD_4}} = \exp \frac{-(\frac{1}{2} h\nu_{CD_4} - \frac{1}{2} h\nu_{CH_4})}{k_B T} \qquad \text{eqn 11}$$

The reposted vibrational frequencies for a C-H bond and a C-D bond are ~ 2917/cm and 2108.9/cm respectively (Nist Chemistry WebBook), T is 1073 K, k_B is 1.38 * 10^{-23} J/K, h is 6.63* 10^{-34} J/s, we calculate the ratio between the rates of CH_4 and CD_4 activation to be approximately 1.7. Therefore, we should expect the steam reforming reaction rate to drop by a factor of 1.7 as we switch from CH_4 to CD_4. For a temperature range of 973-1173 K, we obtain a ratio between the rates of CH_4 and CD_4 activation in the range of 1.8 to 1.6.

Figure 6.6 shows plots of the measured reaction rates as a function of time for Ni/YSZ and Sn/Ni/YSZ catalysts as the fuel was switched from CH_4 to CD_4 and back to CH_4 at an operating temperature of 973K and 1053K respectively. The plots show that the reaction rate of Ni/YSZ and Sn/Ni/YSZ catalysts decreases by a factor of 1.6 and 1.5 repectively as the fuel is switched from CH_4 to CD_4. This is consistent with the primary

isotope effect that we discussed above and the findings of others on Ni catalysts. [8, 23] The slight discrepancy between the calculated and the measured isotope effect might be due to the slightly different vibrational frequencies of normal modes involved in the reaction coordinate on two different surfaces compared to the normal modes associated with the gas-phase CH_4 and CD_4. These results reinforce the fact that C-H bond activation in methane is the rate-limiting step for methane steam reforming on both Sn/Ni/YSZ and Ni/YSZ catalysts.

6.4.3 DFT Calculations

Since C-H bond activation in methane is the rate-limiting step for methane steam reforming on both Sn/Ni and Ni, then the increase in the overall activation barrier for methane steam reforming on Sn/Ni as compared to Ni can be attribute to the change in the nature of the active sites. The difference in the pre-exponential factors for methane steam reforming on Sn/Ni and Ni is also indicative of the change in the nature of the active sites in these two systems. We have measured the pre-exponential factor to be ~ 20 times higher on Sn/Ni as compared to Ni. This indicates that the number of active sites on Sn/Ni is higher than on Ni, but these sites are less active than the ones on Ni as corroborated by the higher activation barrier for methane steam reforming on Sn/Ni as compared to Ni.

We have utilized DFT calculations to identify the active sites for methane activation on Ni and Sn/Ni surface alloy. The surface of a catalytic particle is typically composed of terrace (well-coordinated) sites and step/edge (low-coordinated) sites. To model the terrace and step/edge sites we have utilized (111) and (211) terminated surfaces respectively.

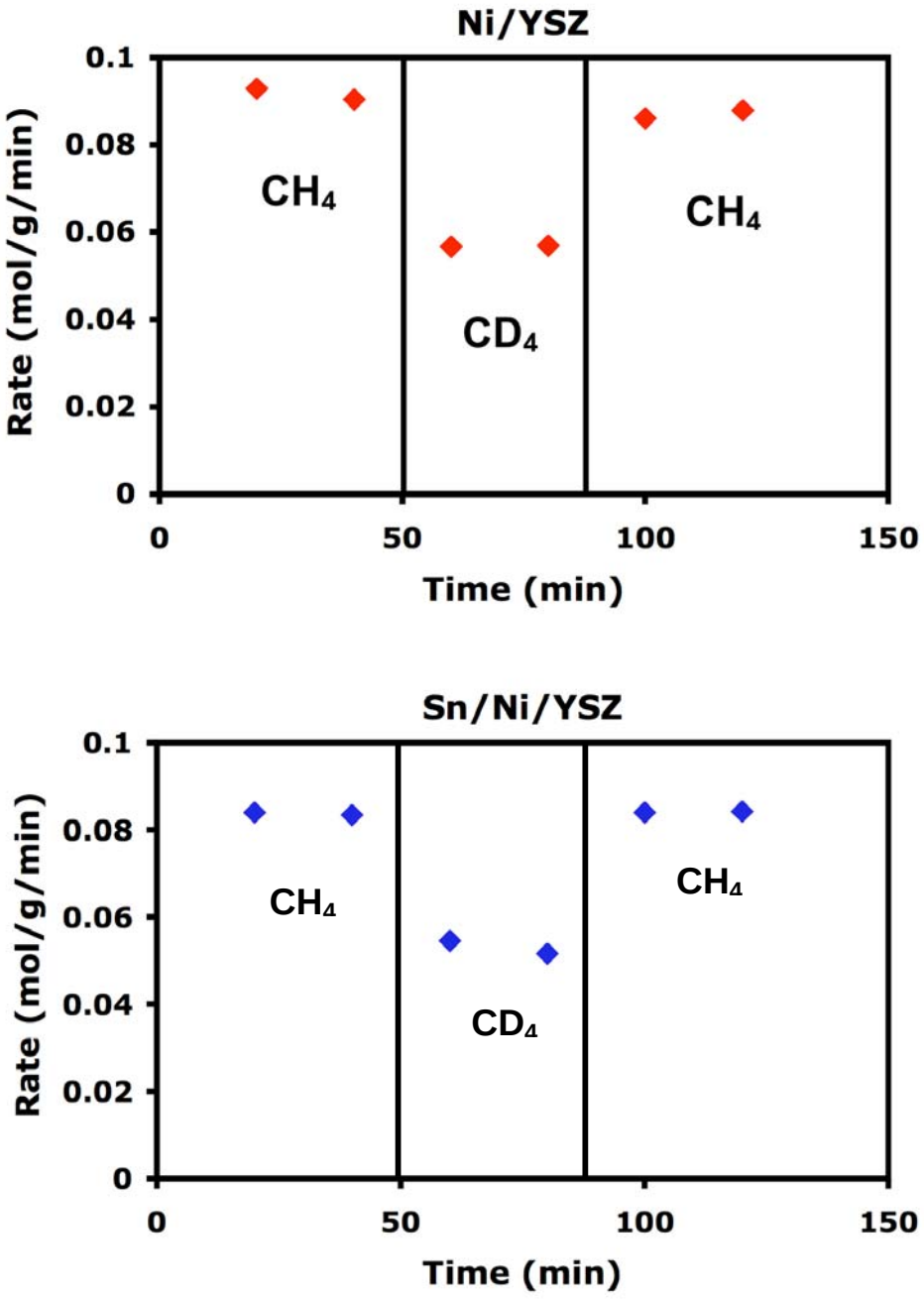

Figure 6-6. Steam reforming rates for CH_4 and CD_4 as a function of time on a) Ni/YSZ at an operating temperature of 973K and b) Sn/Ni/YSZ at an operating temperature of 1053K.

We have calculated the methane activation barrier to be ~ 1.09 eV and 0.8 eV respectively on Ni(111) and Ni(211). This suggests that the active sites on monometallic Ni are the step/edge sites (i.e. under-coordinated surface sites). This is consistent with the findings of others.[13]

On the other hand, in the case of the Sn/Ni surface alloy, we have previously shown using DFT calculations that there is a strong thermodynamic driving force for the Sn atoms to replace Ni atoms from the step edge sites at the limit of low Sn concentrations. This indicates that in the case of the Sn/Ni surface alloy the step/edge sites are mainly populated by Sn atoms thus enabling them to activate methane. Therefore, one would expect terrace sites to be the active sites on Sn/Ni. This is consistent with the fact that the pre-exponential factor is higher for Sn/Ni/YSZ as compared to Ni/YSZ, since terraces are more abundant on the surface of a catalytic particle and are less active than the step/edge sites. We have utilized DFT calculations to obtain the activation barrier for methane on Sn/Ni terrace sites. Figure 6.7 shows that the potential energy barrier for C-H bond activation on Sn/Ni (111) is approximately 1.2 eV. This activation barrier is ~ 0.11 eV higher than the one on Ni (111). This suggests that the electronic effects also play a role in the difference in the methane activation barriers on these sites on Sn/Ni and Ni, since these sites are geometrically identical on Sn/Ni (111) and Ni(111). In the next chapter, we demonstrate how the difference in the electronic structure of the sites is due the interaction between Sn and Ni which leads to the lowering of the d-band center of the Ni atoms in Sn/Ni. Consequently according to the d-band theory this result in a weaker interaction of the Ni atoms in Sn/Ni with adsorbates as compared to monometallic Ni atoms.

The DFT calculations presented herein suggest that the difference in the activation energy of methane on Sn/Ni and Ni is a consequence of both geometric (i.e. poisoning of the Ni sites by Sn resulting in the change of the nature of the active sites from step/edge in monometallic Ni to terraces in Sn/Ni) and electronic effects (i.e. alloying of Sn and Ni resulting in the change of the electronic structure of Ni leading to Ni atoms that are less active than monometallic Ni atoms).

6.5 Conclusion

A kinetic assessment of methane steam reforming on Sn/Ni/SYZ and Ni/YSZ catalysts is obtained using a combination of kinetic studies, isotopic-labeling experiments and DFT calculations. We found that the reaction rate on Sn/Ni/YSZ and Ni/YSZ is first order with respect to methane. Furthermore, we established that C-H bond activation in methane is the rate-limiting step in methane steam reforming on both Sn/Ni/YSZ and Ni/YSZ catalysts. We found that (i) the activation barrier for methane steam reforming was ~ 30 kJ higher on Sn/Ni/YSZ than on Ni/YSZ and (ii) the pre-exponential factor is 20 times higher on Sn/Ni than on Ni. Since the rate-limiting step is the same for Sn/Ni and Ni, then we attributed the difference in the methane activation barrier on Sn/Ni and Ni to the change in the nature of the active sites. We found that on monometallic Ni the active sites are the under-coordinated step/edge sites while on Sn/Ni the active sites are the well-coordinated terrace sites. The DFT-calculated energy barrier for C-H bond activation on the Sn/Ni and Ni terrace sites also suggested that electronic effects play a role in the increased activation barrier for methane on Sn/Ni as compared to monometallic Ni.

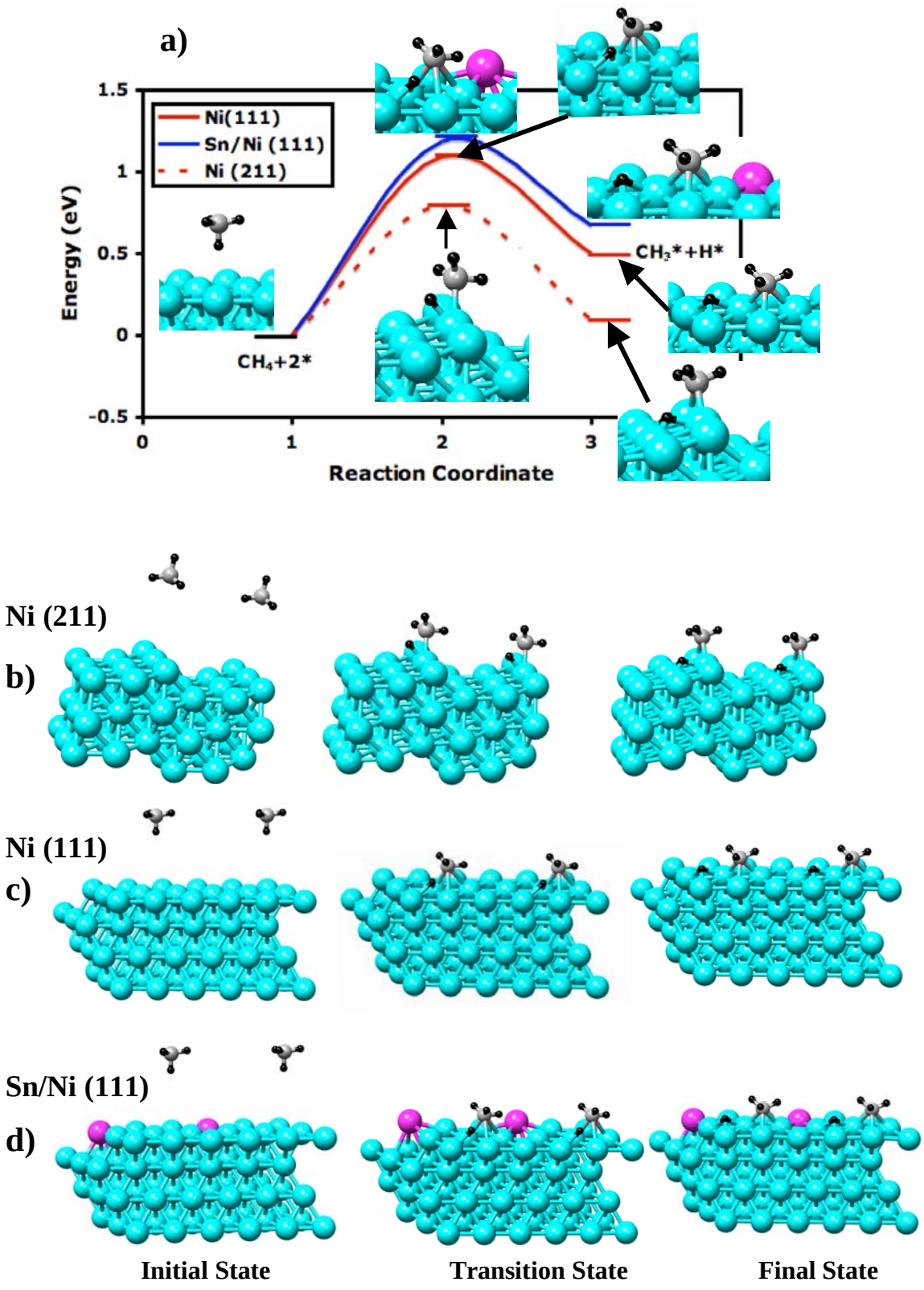

Figure 6.7. a) Potential energy barrier for C-H bond activation in methane on Ni (211), Ni (111) and Sn/Ni (111). The inserts show the geometries of the initial, transition and final states. The detailed geometries of the initial, transition and final states utilized in the DFT calculations for b) Ni(211) c) Ni(111) and d) Sn/Ni (111).

6.6 References

1. Nikolla, E., A. Holewinski, J. Schwank, and S. Linic, *Controlling carbon surface chemistry by alloying: Carbon tolerant reforming catalyst.* Journal of the American Chemical Society, 2006. 128(35): p. 11354-11355.

2. Nikolla, E., J. Schwank, and S. Linic, *Promotion of the long-term stability of reforming Ni catalysts by surface alloying.* Journal of Catalysis, 2007. 250(1): p. 85-93.

3. Nikolla, E., J. Schwank, and S. Linic, *Hydrocarbon steam reforming on Ni alloys at solid oxide fuel cell condition.* Catalysis Today, 2008. 136(3-4): p. 243-248.

4. Bengaard, H.S., et al., *Steam reforming and graphite formation on Ni catalysts.* Journal of Catalysis, 2002. 209(2): p. 365-384.

5. Achenbach, E. and E. Riensche, *Methane Steam Reforming Kinetics for Solid Oxide Fuel-Cells.* Journal of Power Sources, 1994. 52(2): p. 283-288.

6. Xu, J.G. and G.F. Froment, *Methane Steam Reforming, Methanation and Water-Gas Shift.1. Intrinsic Kinetics.* Aiche Journal, 1989. 35(1): p. 88-96.

7. Xu, J.G. and G.F. Froment, *Methane Steam Reforming.2. Diffusional Limitations and Reactor Simulation.* AIChE Journal, 1989. 35(1): p. 97-103.

8. Wei, J.M. and E. Iglesia, *Isotopic and kinetic assessment of the mechanism of reactions of CH_4 with CO_2 or H_2O to form synthesis gas and carbon on nickel catalysts.* Journal of Catalysis, 2004. 224(2): p. 370-383.

9. Snoeck, J.W., G.F. Froment, and M. Fowles, *Steam/CO_2 reforming of methane. Carbon filament formation by the Boudouard reaction and gasification by CO_2, by H-2, and by steam: Kinetic study.* Industrial & Engineering Chemistry Research, 2002. 41(17): p. 4252-4265.

10. Ahmed, K. and K. Foger, *Kinetics of internal steam reforming of methane on Ni/YSZ-based anodes for solid oxide fuel cells.* Catalysis Today, 2000. 63(2-4): p. 479-487.

11. Munster, P. and H.J. Grabke, *Kinetics of the Steam Reforming of Methane with Iron, Nickel, and Iron-Nickel Alloys as Catalysts.* Journal of Catalysis, 1981. 72(2): p. 279-287.

12. Jones, G., et al., *First principles calculations and experimental insight into methane steam reforming over transition metal catalysts.* Journal of Catalysis, 2008. 259(1): p. 147-160.

13. Abild-Pedersen, F., et al., *Methane activation on Ni(111): Effects of poisons and step defects.* Surface Science, 2005. 590(2-3): p. 127-137.

14. Abild-Pedersen, F., et al., *Mechanisms for catalytic carbon nanofiber growth studied by ab initio density functional theory calculations.* Physical Review B, 2006. 73(11)

15. Watwe, R.M., et al., *Theoretical studies of stability and reactivity of CHx species on Ni(111).* Journal of Catalysis, 2000. 189(1): p. 16-30.

16. Perdew, J.P., et al., *Atoms, Molecules, Solids, and Surfaces - Applications of the Generalized Gradient Approximation for Exchange and Correlation.* Physical Review B, 1992. 46(11): p. 6671-6687.

17. Perdew, J.P. and Y. Wang, *Pair-Distribution Function and Its Coupling-Constant Average for the Spin-Polarized Electron-Gas.* Physical Review B, 1992. 46(20): p. 12947-12954.

18. Perdew, J.P., K. Burke, and M. Ernzerhof, *Local and gradient-corrected density functionals.* Chemical Applications of Density-Functional Theory, 1996. 629: p. 453-462.

19. Vanderbilt, D., *Soft Self-Consistent Pseudopotentials in a Generalized Eigenvalue Formalism.* Physical Review B, 1990. 41(11): p. 7892-7895.

20. Fogler, H.S., *Elements of Chemical Reaction Engineering*. 4th ed. 2005: Prentice Hall.

21. Augustine, R.L., *Heterogeneous Catalysis for Synthetic Chemist*. 1996: CRC Press. 647.

22. Wang, S.B. and G.Q. Lu, *Thermogravimetric analysis of carbon deposition over Ni/gamma-Al_2O_3 catalysts in carbon dioxide reforming of methane.* Energy & Fuels, 1998. 12(6): p. 1235-1240.

23. Otsuka, K., S. Kobayashi, and S. Takenaka, *Hydrogen-deuterium exchange studies on the decomposition of methane over Ni/SiO_2.* Journal of Catalysis, 2001. 200(1): p. 4-9.

CHAPTER 7

MEASURING AND RELATING THE ELECTRONIC STRUCTURE OF NONMODEL SUPPORTED CATALYTIC MATERIALS TO THEIR PERFORMANCE

7.1 Summary

Identifying structure-performance relationships is critical for the discovery and optimization of heterogeneous catalysts. Recent theoretical contributions have led to the development of d-band theory, relating the calculated electronic structure of metals to their chemical and catalytic activity. While there are many contributions where quantum chemical calculations have been utilized to validate the d-band theory, experimental examples relating the electronic structure of commercially relevant, nonmodel catalysts to their performance are lacking. We show that even small changes in the near Fermi level electronic structure of nonmodel supported catalysts, induced by a formation of surface alloys, can be measured and related to the chemical and catalytic performance of these materials. We also show that the critical shifts in the alloy d-band are the result of the formation of new electronic states in response to alloying rather than charge redistribution among constitutive alloy elements.

7.2 Introduction

It has been a long-standing goal of fundamental research in heterogeneous catalysis to establish universal relationships between the electronic and geometric structure of catalytic materials and their chemical and catalytic performance.[1-4] Recent theoretical work of Nørskov and coworkers has led to the development of the d-band theory which relates the electronic structure of metals to their chemical activity and catalytic performance.[5-9] In its simplest form the d-band theory states that for a given geometry of an adsorbate on a surface adsorption site, the adsorption energy of the adsorbate depends on the position of the center of mass of d electrons and holes (the d-band center) of the atoms that form the adsorption site. In general, the metals with the d-band center closer to the Fermi level are more chemically active than those with the d-band center further away from the Fermi level. The ultimate value of the d-band theory is that it represents a physically transparent framework towards predictive heterogeneous catalysis, i.e., it allows us to relate even small changes in the electronic structure of an adsorption site, due to alloying, the formation of over-layers of one metal on another metal, chemical poisoning and promotion, to the chemical and catalytic properties of the site. [4-8, 10-13] There are a few contributions where quantum chemical DFT calculations on model systems have been utilized to validate the d-band theory. The experimental examples relating the electronic fingerprint of catalytic materials to their performance have been limited to two recent studies on well-defined model systems.[10, 14] The studies of commercially relevant, supported catalytic materials are lacking.

In this contribution we have utilized a combination of scanning transmission electron techniques and Auger electron spectroscopy (AES) to probe the surface

electronic structure, near Fermi level, of nonmodel supported catalytic materials. We show that even small changes in the electronic structure of supported catalysts, induced by a formation of surface alloys, can be measured and related, in accordance with the d-band model, to the chemical activity and catalytic performance of these materials. Our results show that critical shifts in the d-band center in alloys are related to the formation of new electronic states in response to alloying, rather than to the charge redistribution among constitutive alloy elements. We present our findings in an example where the electronic structure of monometallic Ni and Sn/Ni alloy catalysts supported on yttria stabilized zirconia (YSZ) was measured and related to the chemical behavior of the catalysts. The Sn/Ni alloy contained ~ 2 wt% of Sn with respect to Ni. We have previously characterized the alloy catalyst showing that Sn preferentially segregates in the surface layer of the Ni host, forming the Sn/Ni surface alloy.[15-17] While we present the detailed results for Ni-based catalytic materials, we also show evidence that the conclusions presented herein are universal for other alloys of transition and noble metals.

In the discussion below, we first introduce the experimental measurements that allowed us to make a few general observations regarding the chemical activity of nonmodel Ni and Sn/Ni catalysts. This is followed by an analysis of the relationships between the measured electronic structure of the materials and their chemical activity.

7.3 Experimental Section and Methodology

7.3.1 Catalyst Synthesis

The Ni and the Sn/Ni catalysts were supported on (8 mol %) yttria-stabilized zirconia (YSZ). YSZ was prepared via a standard co-precipitation method. A mixture of yttrium nitrate ($Y(NO_3)_3*6H_2O$) and zirconyl chloride ($ZrOCl_2*2H_2O$) in deionized

water was precipitated using a solution of ammonium hydroxide. After filtration and drying over night, the precipitate was calcined at 1073 K for 2 hours. Ni was introduced to the YSZ support by impregnating Ni nitrate via the incipient wetness technique. The Ni loading in YSZ was about 15 wt% with respect to the total catalyst. After impregnation the catalyst was calcined at 600 ^{o}C for 2 hrs in air in order to convert the Ni nitrate to Ni oxide. The catalyst was then reduced at 1173 K for 3 hours using 30 % H_2/N_2 to insure full reducibility. The Sn/Ni/YSZ catalyst was synthesized by impregnating Sn chloride ($SnCl_2*4H_2O$) to the NiO/YSZ catalyst via the incipient wetness technique. The nominal Sn loading was about 2 wt% with respect to the Ni content in the catalyst. The Sn/Ni/YSZ catalyst was also reduced at 1173 K for 3 hours using 30 % H_2/N_2.

7.3.2 Electron energy loss spectroscopy (EELS) in scanning transmission electron microscope (STEM)

The electron energy loss experiments were carried out in JOEL 2010F field emission electron microscope. The instrument was operated at 200 kV under a pressure of 1.5 * 10^{-7} torr in scanning transmission electron mode (STEM). Gatan imaging filter (GIF) was utilized to collect the low-angle inelasticly scattered electrons to obtain the electron energy loss spectroscopy (EELS) spectra. EELS spectra were analyzed using Digital Micrograph. The lens conditions during operation were defined for a probe sized of about 0.2 nm, with a convergence angle of 13 mrad and a collection angle of 40 mrad. The energy resolution (defined by the full width at half maximum of the zero loss peak) of the energy loss spectra is 1.4 eV at a dispersion of 0.3eV per pixel.

The specimens for the electron microscope experiments were prepared by directly placing the pre-reduced catalyst powders on holey carbon-coated copper grids. Once inside of the electron microscope, the samples were heated under vacuum to 773 K to desorb any impurities. The size of the particles was measured using a number of techniques, including the analysis of XRD spectra, BET measurements, and TEM. The diameter of the analyzed particles was ~ 20 nm.

The reported ELNES spectra were normalized with respect to atomic cross section, which was calculated by integrating the area under the energy loss spectra between 30 and 40 eV above the onset of the Ni L_3 edge. [18, 19] The background effects were subtracted using a standard power law method. [20]

7.3.3 X-ray photoelectron spectroscopy (XPS)

XPS experiments were conducted using Kratos Axis Ultra XPS with 150W Al (Mono) X-ray gun. This instrument was operated under a pressure of $5 * 10^{-9}$ torr. The samples were pre-reduced in a reaction chamber connected to the XPS to avoid oxidation of the samples. The runs were conducted using pass energy of 20 eV. The charge neutralizer was utilized to prevent sample charging. The instrument was calibrated with respect to Au $4f_{7/2}$ at 84 eV.

7.3.4 Reactor Studies

The kinetic studies were conducted isothermally in a packed bed quartz reactor system. The diameter of the quartz reactor was 0.375 inches. Approximately 0.01g of Ni/YSZ and Sn/Ni/YSZ catalysts with particles sizes of 150-200 μm were diluted in 0.5g of quartz powder (250-400μm) and loaded in the packed bed reactor. The catalysts were reduced at 1173 K under a stream of 30% H_2/N_2 for 3 hours prior to measuring reaction rates. The

rates of methane steam reforming were measured as the temperature was varied from 923-1073 K. The absence of diffusion and mass transport limitations was confirmed by analyzing the rates as the total space velocity changed. The set-up included a set of mass flow controllers, a pair of thermocouples (inside and outside the reactor), and syringe pumps for water delivery. The lines after the water inlet were heated to 473K to avoid condensation. The reactor effluent was analyzed using a Varian gas chromatograph (Varian CP 3800) equipped with thermal conductivity detectors (TCD) and a flame ionization detector (FID).

7.3.5 Density functional theory (DFT) calculations

The Dacapo pseudo-potentials plane wave code (http://www.camp.dtu.dk) was employed for all calculations. Our approach was to find a set of parameters that ensured the relative convergence, i.e., the convergence of the respective energies of various structures. For the Ni(111) model system, we utilize 3x3 supercells with 4-layer slabs and 54 special Chadi-Cohen *k*-points. For the Sn/Ni(111) model system, 1/3 of the Ni surface atoms were replaced by Sn in a striped structure. Six layers of vacuum separated the slabs, and a dipole-correction scheme was employed to electro-statically decouple the slabs. The GGA-PW91 functional was employed for self-consistent spin-polarized electronic structure calculations. Vanderbilt pseudo-potentials were employed to describe core electrons. The density of valence electrons was determined self-consistently by iterative diagonalization of Kohn-Sham Hamiltonian using Pulay mixing of densities. The plane wave basis set used to describe the one-electron states was cut off at 350 eV. An electronic temperature (k_bT) of 0.1 was utilized during calculations with the final results extrapolated to 0 K. In the geometry optimization calculations on the (111) surface

termination, the two top substrate layers and adsorbates were allowed to fully relax. The forces were minimized to 0.05eV/A.

The oscillator strength, F(E), shown in Fig 7.3, is the quantity that describes the strength of the transition from one electronic state to another, and it corresponds directly to the information obtained in the experimental ELNES measurements. It was calculated from first principles as a product of two functions: the local density of state, LDOS(E), projected on an atom (in this case on Ni) and a transmission function. [18, 21]

$$F(E) = T(E) * LDOS(E)$$

$$T(E) = \frac{1}{3}\frac{2m}{\hbar^2} E \sum_{i,f} \left| \langle f | r | i \rangle \right|^2$$

The transmission function describes the radial overlap between the initial <i> and final states <f>.[18] It varies slowly with energy and gives the basic edge shape of the spectra. The transmission function for the Ni $L_{2,3}$ edge was calculated previously by Muller and coworkers using linear augmented plane-wave (LAPW) optical oscillator strengths and LAPW-projected LDOS for Ni.[21] While strictly speaking the transition function is dependant on the local environment, this dependence is small. Therefore, in our calculation of oscillator strengths for the $L_{2,3}$ edges we use the transition function calculated for pure Ni. The LDOS for Ni surface atoms in Ni(111) and Sn/Ni(111) was calculated using a plane wave DFT code Dacapo by projected the entire set of states onto spherical harmonics. The cutoff used in the calculation of the Ni d LDOS and the transmission functions were 1.3 Å.

To calculate the broadened oscillator strength (calculated ELNES) we utilized the Lorentzian broadening for the lifetime of the excitations by broadening the initial and final states as described in ref [21, 22]. Gaussian broadening was applied to account for

instrumental resolution. The broadening parameter was estimated based on the instrument resolution, defined by the full width at half maximum of the zero loss peak.

7.4 Results and Discussions

To study the chemical activity of supported Ni and Sn/Ni catalysts, we have performed a number of measurements aimed at quantifying adsorption, desorption, and activation of molecules on the catalysts. All the measurements showed that the supported monometallic Ni catalyst is inherently more chemically active (interacts more strongly with adsorbates) than Sn/Ni (Figure 7.1).[15-17] For example, an Arrhenius analysis of the steady-state reactor data obtained for steam reforming of methane – our kinetic isotope labeling studies and previous contributions of others demonstrated that the rate of methane steam reforming is controlled by the activation of C-H bonds in methane for both catalysts – showed that the overall activation barrier is by ~ 0.3 eV higher on supported Sn/Ni compared to the supported monometallic Ni for the Sn/Ni and Ni particles of identical diameter (Figure 7.1a). Identical conclusions were obtained in thermal gravimetric analysis (TGA) experiments (Figure 7.1b). In these measurements methane was flowed over the catalysts and the catalysts weight was measured. As methane is activated, the weight of the catalyst increases due to the deposition of carbon on the catalysts. The measurements showed that the C-H bond is activated with an activation barrier that is ~ 0.26 eV lower on supported Ni compared to Sn/Ni. Similar conclusions regarding the relative activity on Ni and Sn/Ni were obtained in various molecular desorption studies. For example, temperature programmed reduction (TPR) experiments showed that the reduction temperature for Sn/Ni catalyst was lower than the

reduction temperatures for monometallic Ni and Sn substrates (Figure 7.1c). Quantitative analysis of the TPR data showed that the activation barrier for the oxygen reduction is by ~ 0.09 eV lower on Sn/Ni than on monometallic Ni. We also measured, in the temperature programmed desorption (TPD) of molecular CO, that the activation barrier for the CO desorption is by ~ 0.1 eV lower on supported Sn/Ni compared to Ni.

The difference in the chemical activity of pure Ni and Sn/Ni alloy can be related to the Sn-induced changes in the geometric and electronic structure of Ni. For example, the difference in the C-H activation barrier on Sn/Ni and Ni can to a large degree be explained by a geometric effect where Sn blocks the low-coordinated Ni sites on Ni particles, which are efficient in the activation of C-H bonds. On the other hand, smaller differences between Ni and Sn/Ni in the desorption of O and CO, as measured in the TPR and the CO TPD experiments respectively, are mainly related to the Sn induced modification in the electronic structure of Ni surface atoms. The reason for this is that the O and CO adsorbates interact weakly with the Sn sites in the Sn/Ni surface alloy, i.e., the adsorption of CO and O on Ni and Sn/Ni takes place mainly on the geometrically identical Ni sites on both catalysts. This is illustrated in Figure 7.1d where we have plotted the DFT-calculated adsorption energies for different adsorbates on various sites on Ni and Sn/Ni. Figure 7.1d shows that adsorbate binding energies for the adsorption sites where Sn interacts directly with the adsorbates (Site C in Figure 7.1d) are significantly less exothermic than the adsorption energies on pure Ni.

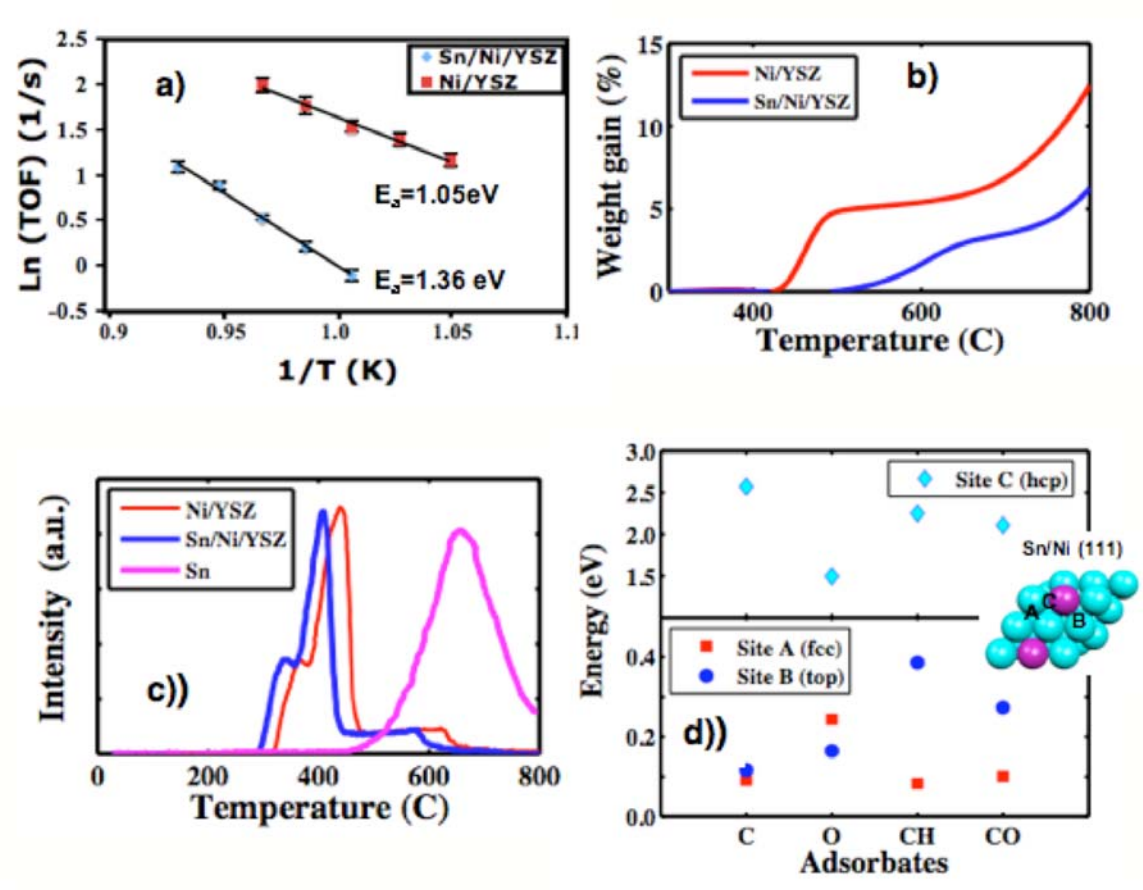

Figure 7.1. a) The catalytic turnover frequency for steam reforming of methane on supported Ni and Sn/Ni alloy as a function of inverse temperature. The slope of the lines is proportional to the overall activation barrier. b) TGA studies of methane decomposition over supported Ni and Sn/Ni. c) TPR measurements for Sn/Ni and monometallic Ni and Sn. d) DFT calculated energies for different adsorbates (O,C, and CH) on various sites Sn/Ni(111) alloy. The energy values for a particular site are referenced to the geometrically identical site on monometallic Ni(111).

The figure also shows that for the geometrically identical Ni sites, the DFT-calculated adsorption energies of oxygen, CO, carbon, and CHx fragments are also less exothermic on Sn/Ni than on Ni, implying that the inherent chemical activity of the Ni atoms is affected by their electronic interaction with the Sn atoms. We note that the Sn-induced decrease in the adsorption energy of C and CH fragments on the Ni sites of Sn/Ni has significant practical implications since it results in lower concentrations of the carbon containing species on Sn/Ni during hydrocarbon reforming reactions, which ultimately improves the tolerance of these materials to carbon-induced deactivation.[15-17]

We have performed a number of studies, including electron energy loss spectroscopy (EELS) and Auger electron spectroscopy (AES) measurements, aimed at identifying the critical electronic features that drive the observed difference in the chemical activity of Ni and Sn/Ni catalysts. We have selected these techniques to study the surface electronic structure of supported catalysts since they allow us to independently probe the states slightly above (EELS) and below (AES) the Fermi level, which is required to measure the shifts in the d-band center. Furthermore, a focused electron beam offers high special resolution and surface sensitivity.

In EELS experiments a high-energy electron beam (~ 0.2 nm in diameter) is focused on a specimen, exciting electrons from the core energy levels to local unoccupied states above the Fermi Level. The process generates atom-specific signals (electron energy loss) referred to as ionization edges. The ionization edge also has small intensity fluctuations which depend on the local chemical environment.[18] The intensity fluctuations just above the onset of the ionization edge (up to 30-40 eV above the onset) are referred to as the electron energy-loss near-edge structure (ELNES), and these can be

related to the unoccupied electronic states above the Fermi level, localized on the atom from which the core electron was exited.[18, 19, 21, 23-27] For example in the case of Ni, electrons can be ejected from the $2p^{1/2}$ and $2p^{3/2}$ core energy states to the unoccupied 3d states, generating L_2 and L_3 edges, respectively.

Figure 7.2(b,c) shows the EELS spectra for supported Ni and Sn/Ni particles obtained with a scanning transmission electron microscope (STEM) for the electron beam focused either on the region close to the boundary of the particles, probing mainly the electronic structure of the surface of particles, or the region close to the center of the particles, probing mainly the particle bulk. Figure 7.2(b,c) shows that the ratio of the Sn M-edge to Ni L-edge is the highest when the boundary of the Sn/Ni catalytic particle is probed, and it decreases as the electron beam is moved closer to the center of the particle. These observations are consistent with our previous studies showing that Sn preferentially segregates to the surface of the Sn/Ni particles. Figure 7.2(d, e) shows the measured Ni $L_{2,3}$ ELNES for the two regions of Ni and Sn/Ni particles normalized with respect to the atomic cross section (see Methods section). The figure shows that the Ni $L_{2,3}$ ELNES for a region close to the center of the Ni and Sn/Ni particles are almost identical to each other (Figure 7.2e), which is not surprising considering that in both cases the spectra are dominated by Ni atoms in the bulk. On the other hand, when a region close to the boundary of the catalytic particles is probed, the Ni $L_{2,3}$ ELNES are broadened for the Sn/Ni particle compared to monometallic Ni particle (Figure 7. 2d).

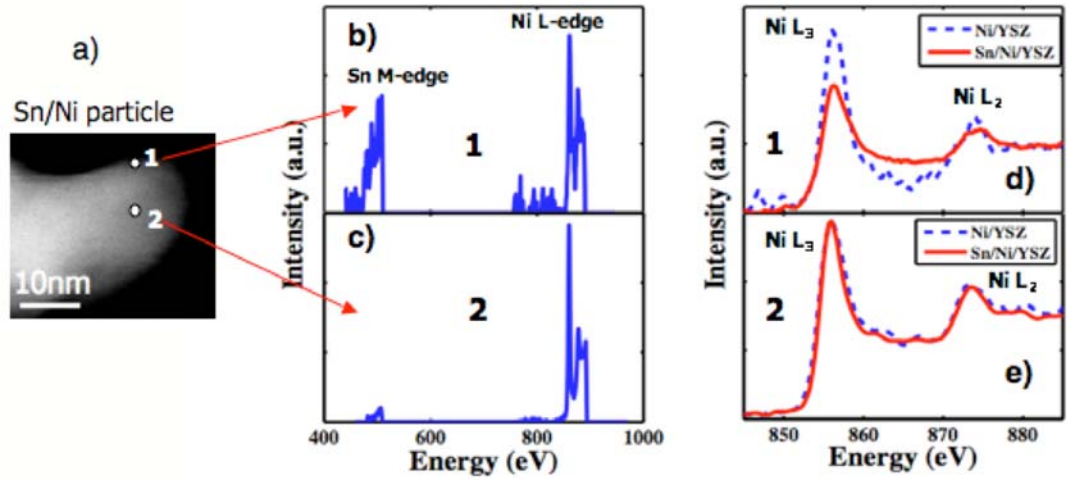

Figure 7.2. a) STEM of a Sn/Ni particle supported on YSZ. b) EELS spectra obtained with a ~ 0.2 nm electron beam focused on the edge of the Sn/Ni particle (edge of the particles is labeled with number 1). c) EELS spectra with the electron beam focused on the center of the particle (center is labeled with number 2). d) Ni $L_{2,3}$ ELNES for the surface region of pure Ni and Sn/Ni. e), Ni $L_{2,3}$ ELNES for the bulk region of Ni and Sn/Ni.

We find that the broadening of the Ni $L_{2,3}$ near edge for the Sn/Ni particles is associated with the formation of new electronic states above the Fermi level due to the hybridization between the d states of Ni atoms and the s, p states of the neighboring Sn atoms. This is illustrated in Figure 7.3(c, d, e) where the DFT calculated local density of states (LDOS) projected on a Ni atom in the surface layer of the monometallic Ni (111) (Figure 7.3c) and Sn/Ni(111) surface alloy (Figure 7.3d) as well as the Sn LDOS for the Sn/Ni(111) surface alloy (Figure 7.3e) are shown. We have performed calculations on the (111) surfaces since these are the lowest energy surfaces and they describe the most dominant terrace sites on a catalytic particle. Thermodynamic simulations of Sn/Ni particles with relevant diameter (~ 20 -30 nm) and Sn concentration (~2 wt % with respect to Ni), based on Wulf Kaishev formalism with surface energies for different Sn/Ni surface facets calculated using DFT, [28] showed that the Sn/Ni(111) surface structure, depicted as an insert in Figure 7.3, dominates the surface of these Sn/Ni particles.

To quantitatively relate the Ni LDOS to the measured ELNES we have calculated from first principles the oscillator strength (this quantity is directly related to measured ELNES signal) for the excitation of electrons from the localized Ni 2p states to the localized Ni 3d states in monometallic Ni(111) and the model Sn/Ni(111) surface (see Methods).[18, 21]

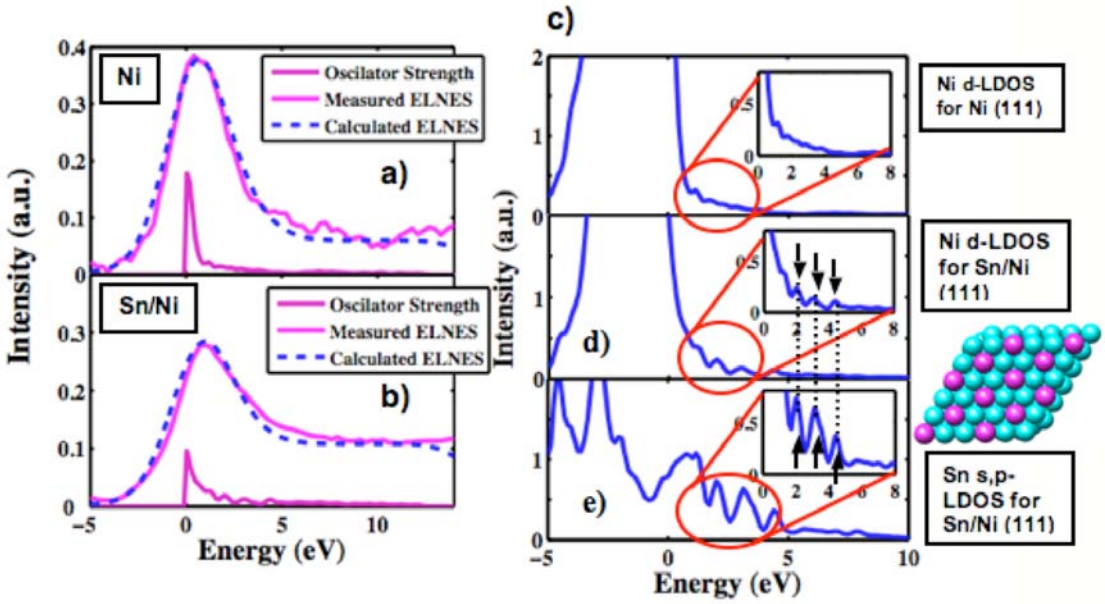

Figure 7.3. a) Calculated Ni $L_{2,3}$ oscillator strength, calculated broadened Ni $L_{2,3}$ oscillator strength (calculated ELNES), and measured Ni $L_{2,3}$ ELNES for pure Ni. b) Calculated Ni $L_{2,3}$ oscillator strength, calculated broadened Ni $L_{2,3}$ oscillator strength (calculated ELNES), and measured Ni $L_{2,3}$ ELNES for Sn/Ni alloy. b) Calculated local density of d states projected on a Ni surface atom in Ni(111). b) Calculated local density of d states projected on a Ni surface atom in Sn/Ni(111). b) Calculated local density of s,p states projected on a Sn surface atom in Sn/Ni(111). The arrows between the inserts in d and e point to the hybridization between the d states of Ni and the s,p states of Sn. The Sn/Ni(111) surface alloy model system is shown in insert.

Figure 7.3(a, b) shows that when we account for the finite lifetime of the excitations and the instrumental resolution, which broaden the calculated oscillator strength, the calculated spectra is almost identical to the measured Ni $L_{2,3}$ ELNES, thus reinforcing the notion that the formation of the Sn/Ni surface alloy results in the broadening of the unoccupied Ni d states above the Fermi Level due to the hybridization between the Sn s, p states and Ni d states and further supporting the model of the Sn/Ni particle surface.

To quantify the number of the d states localized on Ni atoms above the Fermi level (d-holes), we have integrated the Ni-$L_{2,3}$ ELNES for the Sn/Ni alloy and monometallic Ni (Table 1). Table 1 shows that the integrated Ni $L_{2,3}$ ELNES for Ni and Sn/Ni catalytic particle are very similar to each other, with a variation of ~ 2 %. These observations suggest that while the shape of ELNES changes, the number of the d-holes localized on Ni does not change upon the formation of the Sn/Ni surface alloy.

Table 7.1. Values obtained by integrating the measured, normalized with respect to atomic cross section, Ni L2,3 ELNES and calculated oscillator strengths for the Sn/Ni alloy and monometallic Ni. The range of integration for the measured Ni L2,3 ELNES was between -5 to 35 eV from the onset of the Ni L_3 edge. It included the near edge regions of both the Ni L_3 and L_2 edges. The range of integration for the calculated oscillator strength was between 0 to10 eV above the Fermi Level.

Catalysts	Integrated Ni L edge	Normalized w.r.t to Ni	Integrated oscillator strength	Normalized w.r.t Ni
Ni/YSZ	3.48 ± 0.07	1.000	0.256	1.000
Sn/Ni/YSZ	3.41 ± 0.07	0.98 ± 0.04	0.255	0.997

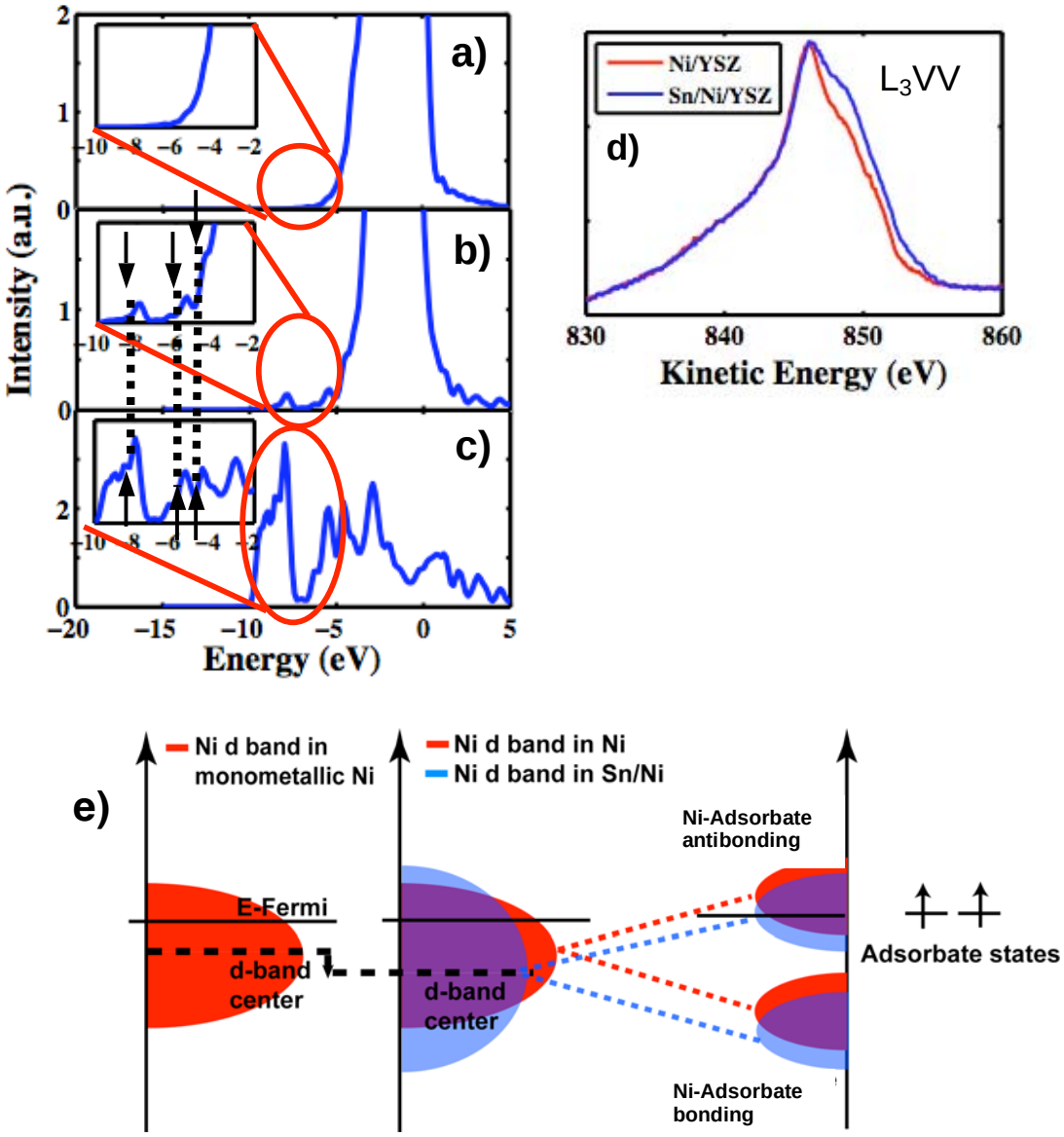

Figure 7.4. a) Calculated local density of d states projected on a Ni surface atom in Ni(111). b) Calculated local density of d states projected on a Ni surface atom in Sn/Ni(111). c) Calculated local density of s,p states projected on a Sn surface atom in Sn/Ni(111). d) Ni $L_3M_{4,5}M_{4,5}$ AES for supported Ni and Sn/Ni. e) Schematics describing the interaction between the Ni d-band in monometallic Ni and the Sn/Ni surface alloy with a generic adsorbate.

To probe the electronic states below the Fermi level we have utilized AES. In the case of Ni, where the width of the d-band is larger than the interaction between two holes created in the d-band upon the emission of the Auger electron, the shape of the Auger spectra for the $L_3M_{4,5}M_{4,5}$ electron transition is sensitive to the width of the Ni LDOS just below the Fermi level.[29, 30] The AES for the Ni $L_3M_{4,5}M_{4,5}$ electron transition for the supported Ni and Sn/Ni catalysts are shown in Figure 7.4d. The figure shows that the Ni Auger spectrum for Sn/Ni is broadened compared to the spectra of pure Ni, indicating that the Ni d-band below the Fermi level is broader for Sn/Ni than for monometallic Ni. These observations are further supported by the DFT calculated Ni and Sn LDOS for pure Ni and Sn/Ni, shown in Figure 7.4(a, b, c), where the hybridized Sn-Ni states below the Fermi level are observed in the Sn/Ni surface alloy.

Further quantitative analysis of the Auger spectra, including the evaluation of the ratios of the Ni $LM_{4,5}M_{4,5}$ to Ni $LM_{2,3}M_{4,5}$ intensities and the Ni $LM_{4,5}M_{4,5}$ to the Ni 2p XPS intensity for the Sn/Ni and pure Ni samples, showed that while the Ni d-band below the Fermi level is broadened due to the Sn-Ni interaction, the number of states in the valence d-band is preserved.

ELNES and AES measurements suggest that the formation of the Sn/Ni surface alloy is accompanied by the formation of new electronic states above and below the Fermi level. While these states broaden the d-projected Ni LDOS, they do not lead to a measurable charge transfer (electrons or holes) between Ni and Sn. The lack of charge transfer between Sn and Ni in the Sn/Ni alloy is further supported by the results of our x-ray photoelectron studies which showed that the Ni 2p and Sn 3d states are not shifted significantly in the two catalysts and are consistent with the neutral Ni^0 and Sn^0 spectra

respectively (see Figure 7.5). This also suggests that for this particular system it is not possible to relate the binding energy of core electrons (as measured by XPS) to the shifts in electronic states near Fermi level.

To preserve the number of d-holes and d-electrons localized on Ni and in response to the formation of new states which broaden the d-band, the center of the Ni d-band for Sn/Ni must shift down in energy with respect to monometallic Ni. This is illustrated in the schematics shown in Figure 7.4e. The measured change in the electronic structure has a number of practical consequences including the diminished chemical activity of the Ni sites in Sn/Ni, which can be understood in terms of the d-band theory. For example, various adsorbates, important in many catalytic processes, such as O, C, OH, CO, and CH_x fragments interact with the d-states of Ni via the formation of bonding and anti-bonding orbitals. The position of the bonding and anti-bonding orbitals with respect to the Fermi level depends on the position of the substrate d-band center. For Ni atoms with the d-band center closer to the Fermi level (i.e., monometallic Ni catalyst) the anti-bonding Ni-adsorbate states will be higher in energy than the anti-bonding Ni-adsorbate states formed when the adsorbate interacts with Ni atoms in Sn/Ni. The consequence of this is that the anti-bonding adsorbate-Ni states for Sn/Ni catalysts are populated to a higher degree than the anti-bonding states for monometallic Ni, which ultimately decreases the strength of interaction between the adsorbates (O, C, OH, CH_x, ..) and the Ni sites on the Sn/Ni substrate. These observations also suggest that the adsorbate/substrate interactions are not directly related to the number of d holes in substrate as has been postulated previously.[4]

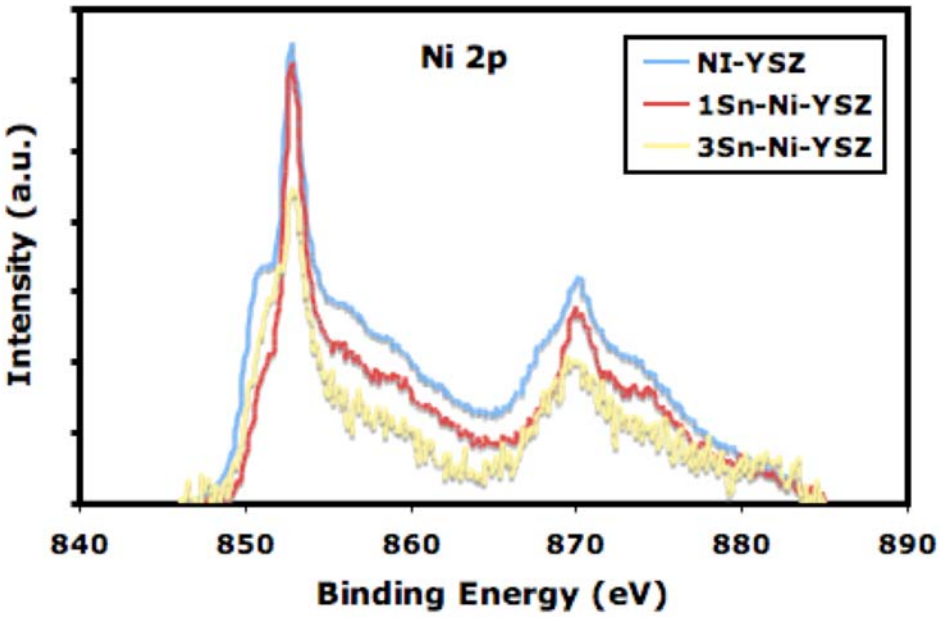

Figure 7.5. Collected Ni 2p XPS spectra for monometallic Ni and Sn/Ni catalysts (3 wt % Sn and 1 wt % Sn with respect to Ni). The figure shows that there is no significant shift in the position of the Ni 2p peak in response to the formation of the Sn/Ni alloys suggesting no significant charge transfer.

Another critical observation that can be made based on the presented studies is that the interaction between Ni and Sn in the surface alloy is dominated by the formation of shared electronic states which are distributed so that the center of d-band is shifted downward. This is in contrast to the models, such us the rigid band description of alloys, which argue that the change in the electronic structure of elements in an alloy is due to the transfer of charge among the constitutive elements rather than due to the rearrangements in the structure of LDOS.[31] Our results suggest that local potentials of constitutive elements and the screening process in metals minimize the measurable charge transfer from one element to another, and that the interaction between constitutive elements is governed by the orbital hybridization and the formation of new electronic states. For Sn/Ni system this is not surprising considering that electro-negativities of Sn and Ni are fairly similar to each other.

We have observed that a similar physical picture, where the changes in the position of the d-band center for various sites in alloys can be explained in terms of the preserved local charge and the formation of new electronic states, explains the change in electronic structure and therefore the chemical activity of the Ni sites in Ag/Ni and Au/Ni alloys (see Figure 7.6).[32] Similar conclusions were obtained in extensive DFT studies of Pt alloys by Kitchin et al. who showed that the formation of the alloys and the induced shifts in d-band are not accompanied by significant charge transfer between Pt and other elements in the alloys.[33] It is our hypothesis that identical observations can be made for almost any combination of two transition or noble metals that form bulk or surface alloys. One reason for this is that the constitutive elements in the alloys will have similar electro-negativities – it has been observed empirically by Hume and Rothery (better known as

Hume-Rothery rules) that in order for two metallic compounds to form an alloy they must have similar electronegativities – and the interaction between the elements will take place via the formation of hybridized electronic states. These states determine the change in the position of the projected d-bands which governs the interaction of the alloys with adsorbates. Another reason might be an innate tendency of metal atoms to maintain a constant local charge as illustrated in recent calculations by Raebiger et al.[34]

It is also important to briefly discuss the relationships between the electronic structure of a catalytic material and its performance. This relationship is critical for the development of systematic approaches towards the discovery of new or improved solid state heterogeneous catalysts. For example, the Sn-induced lowering in the center of the Ni d-band (the decrease in the average energy of d-electrons in the system) led us to conclude that: (i) due to the lower electronic energy of this system compared to pure Ni, there should be a significant thermodynamic driving force to form the Sn/Ni surface alloy and sustain it under catalytic conditions, (ii) the Sn/Ni binds carbon and carbon fragments less strongly than monometallic Ni, therefore decreasing the surface concentration of carbon-carrying intermediates on the catalyst surface during hydrocarbon reforming reactions, and diminishing the driving force for the formation of solid carbon deposits which are known to deactivate monometallic Ni catalysts. These physical characteristics of Sn/Ni have guided us in the identification of these alloy materials as potential carbon-tolerant electro-catalysts for electro-chemical oxidation of hydrocarbons on Solid Oxide Fuel Cells, which was verified experimentally in the previous chapters.

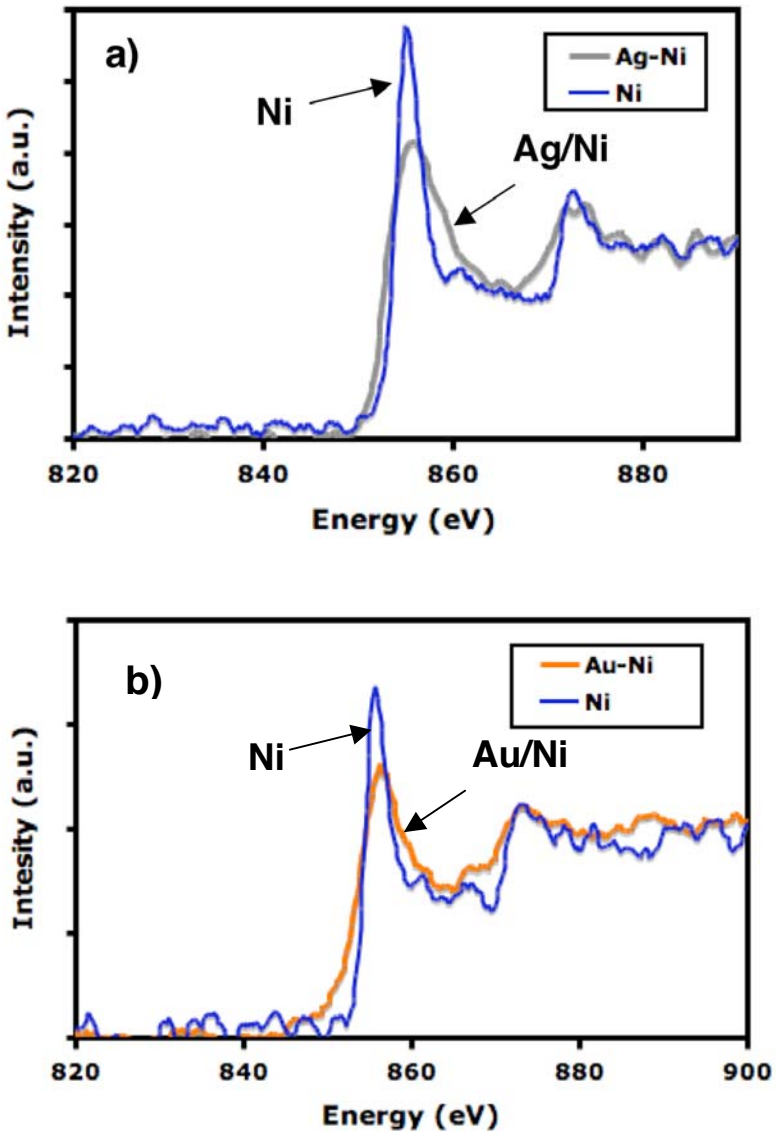

Figure 7.6. Measured ELNES Ni L_2 and L_3 edges for the electron beam penetrating the boundary (probing the surface) of monometallic Ni and Ag/Ni particles (Figure 7.6 (a)) and monometallic Ni and Au/Ni particles (Fig 6(b)). It is clear that the Ni L_2 and L_3 edges are broader for Ag/Ni and Au/Ni compared to Ni. We also find the number of d-holes localized on Ni is identical for both systems suggesting the local charge is preserved.

We have also shown that these physical features are directly responsible for the experimentally established superior carbon tolerance of Sn/Ni compared to monometallic Ni in hydrocarbon reforming reactions.[11, 14-17, 35, 36]

7.5 Conclusion

In conclusion, we analyzed the changes in surface electronic structure associated with the formation of supported Ni alloy catalysts. We quantified the electronic states in the vicinity of Fermi level using a number of electronic probes and showed that even small changes in the electronic structure of nonmodel supported catalysts, induced by a formation of surface alloys, can be related to the chemical activity and catalytic performance of these materials. These findings support the models that suggest that the position of the center of electronic d-band can be related to the catalytic activity of the material. We also find that the critical shifts in the d-band center in alloys are the result of the formation of new electronic states in response to alloying, and that the electronic charge on constitutive alloy elements is preserved. These results provide a framework for predicting the shifts in the d-band center in response to alloying. This is important for establishing universal structure-performance relationships that can guide us in the discovery of novel or improved heterogeneous catalyst.

7.6 References

1. Feibelman, P.J. and D.R. Hamann, *Electronic-Structure of a Poisoned Transition-Metal Surface.* Physical Review Letters, 1984. 52(1): p. 61-64.

2. Falicov, L.M. and G.a. Somorjai, *Correlation between Catalytic Activity and Bonding and Coordination-Number of Atoms and Molecules on Transition-Metal Surfaces - Theory and Experimental-Evidence.* Proceedings of the National Academy of Sciences of the United States of America, 1985. 82(8): p. 2207-2211.

3. Cohen, M.H., M.V. Gandugliapirovano, and J. Kudrnovsky, *Orbital Symmetry, Reactivity, and Transition-Metal Surface-Chemistry.* Physical Review Letters, 1994. 72(20): p. 3222-3225.

4. Harris, J. and S. Andersson, *H-2 Dissociation at Metal-Surfaces.* Physical Review Letters, 1985. 55(15): p. 1583-1586.

5. Hammer, B. and J.K. Norskov, *Electronic factors determining the reactivity of metal surfaces.* Surface Science, 1995. 343: p. 211-220.

6. Hammer, B., Y. Morikawa, and J.K. Norskov, *CO chemisorption at metal surfaces and overlayers.* Physical Review Letters, 1996. 76(12): p. 2141-2144.

7. Hammer, B. and J.K. Norskov, *Why Gold Is the Noblest of All the Metals.* Nature, 1995. 376(6537): p. 238-240.

8. Norskov, J.K., et al., *Universality in heterogeneous catalysis.* Journal of Catalysis, 2002. 209(2): p. 275-278.

9. Hammer, B., *Special sites at noble and late transition metal catalysts.* Topics in Catalysis, 2006. 37(1): p. 3-16.

10. Nilsson, a., et al., *The electronic structure effect in heterogeneous catalysis.* Catalysis Letters, 2005. 100(3-4): p. 111-114.

11. Greeley, J. and M. Mavrikakis, *Alloy catalysts designed from first principles.* Nature Materials, 2004. 3(11): p. 810-815.

12. Delbecq, F. and P. Sautet, *Density functional periodic study of CO adsorption on the Pd3Mn(100) alloy surface: Comparison with Pd(100).* Physical Review B, 1999. 59(7): p. 5142-5153.

13. Pedersen, M.O., et al., *How a gold substrate can increase the reactivity of a Pt overlayer.* Surface Science, 1999. 426(3): p. 395-409.

14. Stamenkovic, V.R., et al., *Trends in electrocatalysis on extended and nanoscale Pt-bimetallic alloy surfaces.* Nature Materials, 2007. 6(3): p. 241-247.

15. Nikolla, E., et al., *Controlling carbon surface chemistry by alloying: Carbon tolerant reforming catalyst.* Journal of the American Chemical Society, 2006. 128(35): p. 11354-11355.

16. Nikolla, E., J. Schwank, and S. Linic, *Promotion of the long-term stability of reforming Ni catalysts by surface alloying.* Journal of Catalysis, 2007. 250(1): p. 85-93.

17. Nikolla, E., J. Schwank, and S. Linic, *Hydrocarbon steam reforming on Ni alloys at solid oxide fuel cell condition.* Catalysis Today, 2008. 136(3-4): p. 243-248.

18. Keast, V.J., et al., *Electron energy-loss near-edge structure - a tool for the investigation of electronic structure on the nanometre scale.* Journal of Microscopy-Oxford, 2001. 203: p. 135-175.

19. Botton, G.A., et al., *Experimental and theoretical study of the electronic structure of Fe, Co, and Ni aluminides with the B2 structure.* Physical Review B, 1996. 54(3): p. 1682-1691.

20. Egerton, R.F., *Electron Energy Loss Spectroscopy in the Electron Microscope*. 2nd ed. 1996, New York: Plenum.

21. Muller, D.A., D.J. Singh, and J. Silcox, *Connections between the electron-energy-loss spectra, the local electronic structure, and the physical properties of a material: A study of nickel aluminum alloys.* Physical Review B, 1998. 57(14): p. 8181-8202.

22. Muller, J.E. and J.W. Wilkins, *Band-Structure Approach to the X-Ray-Spectra of Metals.* Physical Review B, 1984. 29(8): p. 4331-4348.

23. Muller, D.A. and M.J. Mills, *Electron microscopy: probing the atomic structure and chemistry of grain boundaries, interfaces and defects.* Materials Science and Engineering a-Structural Materials Properties Microstructure and Processing, 1999. 260(1-2): p. 12-28.

24. Pearson, D.H., C.C. Ahn, and B. Fultz, *White Lines and D-Electron Occupancies for the 3D and 4D Transition-Metals.* Physical Review B, 1993. 47(14): p. 8471-8478.

25. Muller, D.A., P.E. Batson, and J. Silcox, *Measurement and models of electron-energy-loss spectroscopy core-level shifts in nickel aluminum intermetallics.* Physical Review B, 1998. 58(18): p. 11970-11981.

26. Muller, F., et al., *EELS investigation of thin epitaxial NiO/Ag(001) films: surface states in the multilayer, monolayer and submonolayer range.* Surface Science, 2000. 459(1-2): p. 161-172.

27. Potapov, P.L., et al., *Structural and chemical effects on EELS L-3,L-2 ionization edges in Ni-based intermetallic compounds.* Physical Review B, 2001. 6418(18)

28. In these calculations the energies of various Sn/Ni structures, including those where Sn displaces Ni from bulk, subsurface, or surface, were calculated using DFT. The calculated energies were an input in thermodynamic simulations which allowed us to identify the lowest energy structure of Sn/Ni particles following Wulf Kaishev theorem. For the relevant particle size and Sn concentrations of interest the Sn/Ni particles were dominated by the (111) facets with the Sn and Ni distribution shown in Fig. 4.

29. Bennett, P.A., et al., *Electronic-Structure of Ni and Pd Alloys.3. Correlation-Effects in the Auger-Spectra of Ni-Alloys.* Physical Review B, 1983. 27(4): p. 2194-2209.

30. Diplas, S., et al., *Characterization of Ni-B amorphous alloys with x-ray photoelectron and secondary ion mass spectroscopy.* Surface and Interface Analysis, 2005. 37(5): p. 459-465.

31. Pollock, D.D., *Physic Properties of Materials for Engineers*. 2nd ed. 1993: CRC Press.

32. Besenbacher, F., et al., *Design of a surface alloy catalyst for steam reforming.* Science, 1998. 279(5358): p. 1913-1915.

33. Kitchin, J.R., et al., *Role of strain and ligand effects in the modification of the electronic and chemical properties of bimetallic surfaces.* Physical Review Letters, 2004. 93(15)

34. Raebiger, H., S. Lany, and A. Zunger, *Charge self-regulation upon changing the oxidation state of transition metals in insulators.* Nature, 2008. 453: p. 763-766.

35. Zhang, J.L., et al., *Controlling the catalytic activity of platinum-monolayer electrocatalysts for oxygen reduction with different substrates.* Angewandte Chemie-International Edition, 2005. 44(14): p. 2132-2135.

36. Xu, Y., A.V. Ruban, and M. Mavrikakis, *Adsorption and dissociation of O-2 on Pt-Co and Pt-Fe alloys.* Journal of the American Chemical Society, 2004. 126(14): p. 4717-4725.

CHAPTER 8

NI SURFACE ALLOYS AS CARBON TOLERANT ELECTROCATALYSTS

8.1 Summary

In the previous chapters, we have employed a combined experimental and theoretical approach to identify ways to prevent carbon-induced deactivation of Ni catalysts during catalytic and electro-catalytic hydrocarbon reforming. Density functional theory (DFT) calculations were employed to study carbon chemistry on Ni. Through this process, we were able to identify possible strategies that could lead to the identification of carbon tolerant catalysts and electrocatalysts. We suggested that possible carbon tolerant electrocatalysts are those materials that facilitate C-O versus C-C bond formation and hinder carbon nucleation at the low coordinated surface sites. These strategies led to the identification of the Sn/Ni surface alloy as a promising carbon tolerant catalyst. In this chapter, we implement the same strategies to screen for other Ni alloys that might be more carbon tolerant catalysts than monometallic Ni. We test the carbon tolerance of the

predicted Ni alloys under steam reforming of isooctane at moderate steam to carbon ratios.

8.2 Introduction

Carbon poisoning of Ni catalysts and electrocatalysts has been an obstacle for the long term stability of the steam reforming processes and the development of solid oxide fuel cells (SOFCs) that can utilize hydrocarbon fuels directly on-cell.[1-7] In this chapter, we expand on the ideas developed in the previous chapters and attempt to identify additional Ni alloys that might exhibit superior carbon tolerance compare to pure Ni. Again, we screen for Ni alloy catalysts that facilitate C-O over C-C bond formation and that hinder carbon nucleation at the low coordinated surface sites. Aside from these characteristics, the alloy catalysts need to be stable under relevant external conditions. We have utilized quantum DFT calculations to calculate the formation energies for the alloys and have investigated their stability under relevant conditions. Packed bed reactor studies were employed to test the carbon tolerance of the Ni alloys during the steam reforming of isooctane at moderate steam to carbon ratios.

8.3 Experimental Section

8.3.1 Density Functional Theory (DFT)

The Dacapo pseudo-potentials plane wave code (http://www.camp.dtu.dk) was employed for all calculations. For the Ni(111) model system, we utilize p(3x3) supercells with 4-layer slabs and 18 special Chadi-Cohen *k*-points. The calculations for the (211) termination surfaces were performed using p(1x3) supercells with 9-layer slabs and 3x3x1 Monkhorst-Pack *k*-points. Six layers of vacuum separated the slabs, and a dipole-

correction scheme was employed to electro-statically decouple the slabs. The GGA-PW91 functional was employed for self-consistent spin-polarized electronic structure calculations. Vanderbilt pseudo-potentials were employed to describe core electrons. The density of valence electrons was determined self-consistently by iterative diagonalization of Kohn-Sham Hamiltonian using Pulay mixing of densities. The plane wave basis set used to describe the one-electron states was cut off at 350 eV. An electronic temperature (k_bT) of 0.1 was utilized during calculations with the final results extrapolated to 0 K. In the geometry optimization calculations on the (111) surface termination, the two top substrate layers and adsorbates were allowed to fully relax. On the (211) termination, the three top substrate layers were alloyed to relax in the x (normal to the direction of the step-edge) and z directions. The forces were minimized to 0.05eV/Å.

The first order transition states for one-atom diffusion were identified by probing the high-symmetry sites between reactant and product states. The diffusing atom was fixed in the x-y plane on these sites and it was allowed to relax in the z direction. Energies were calculated for all high symmetry sites (hollow, bridge, and on-top) and the potential energy surfaces were constructed. The identity of the first order transition states was validated by making sure that the forces acting on the system vanish at the transition state and that the force on the diffusing atom changes sign as it moves through the transition state from the reactant to the product state. We have further validated the transition states by slightly changing the geometry of the transition state along the reaction coordinate towards the product or reactant geometry and allowing the system to fully relax into the respective product and reactant states. [8] This procedure established that the transition state energies are maximum along the reaction coordinate and

minimum with respect to other degrees of freedom. [9-11] The forces in these calculations were minimized to 0.05 eV/Å. Transition states for the C-O and C-C bond formation were identified using Climbing Nudged Elastic Band method [12-14].

8.3.2 Catalyst Synthesis

The catalysts utilized herein were composed of Ni or Ni alloys supported on 8 mol% yttria-stabilized zirconia (YSZ). The technique employed to synthesize the support is outlined in Chapter 2. The Ni loading on the monometallic Ni and Ni alloy catalysts was 15 % by weight with respect to the total catalysts. Ni/YSZ catalysts were synthesized by impregnating the appropriate amount of $Ni(NO_3)_3$ on the support. The Ni surface alloys were synthesized by impregnating $SnCl_2*xH_2O$, $AgNO_3$ or $HAuCl_4*xH_2O$ on the support via the incipient wetness method. The nominal loading of the Sn, Ag, and Au on the Sn/Ni, Ag/Ni and Au/Ni catalysts respectively was 1 wt % with respect to the weight of Ni. The catalyst were calcined at 873K for two hours and reduced under a stream of 30% H_2/N_2 for 3 hours at 1173K.

8.3.3 Reactor Studies

The reactor experiments were conducted isothermally at 1073 K in a packed bed reactor set-up. The set-up included a set of mass flow controllers, a pair of thermocouples (inside and outside the reactor), and peristaltic pumps for liquid delivery. Approximately 0.8 g of catalyst (active material plus support in both powder and pellet form) and a total inlet gas flow-rate of 1400 sccm were used, yielding a gas hourly space velocity (GHSV) of 50,000 hr^{-1}. Gas feeds were delivered with mass flow controllers while liquid fuels and water were supplied via peristaltic pumps. The reactor effluent

was analyzed using a Varian gas chromatograph (Varian CP 3800) equipped with thermal conductivity detectors.

8.3.4 Thermal gravimetric analysis (TGA)

Thermal gravimetric analysis (TGA) experiments were performed with a TA instruments thermo-gravimetric analysis (TGA Q500). Initially approximately 0.2 g of catalyst was reduced under 30% H_2/N_2 at 1073 K for 2 hours. Once reduced the catalysts were cooled to room temperature while exposed to pure nitrogen. Following the reduction procedure the catalysts were exposed to dry methane and the temperature was ramped to 1073 K at a set heating rate. The weight of the sample was measured as the temperature increased and methane decomposed on the surface of the catalyst.

8.4 Results and Discussions

We have previously demonstrated using quantum DFT calculations that in methane steam reforming and oxidation reactions, the two most thermodynamically stable states for the C atoms formed during methane activation are CO and graphene. Any carbon-tolerant catalyst needs to be able to oxidize carbon and form CO and CO_2 with higher rates than to form C-C bonds. The formation of the C-C bonds leads to the formation of solid carbon structures, which deactivate the catalyst. Furthermore, it has also been shown that carbon nucleation on the low coordinated Ni surface sites also plays an important role in the growth of extended carbon structures.[15, 16] If one accepts that these mechanisms play an important role in the carbon-induced deactivation of Ni, then in order to prevent carbon poisoning one has to identify materials that favor CO over graphene formation and also hinder carbon nucleation.

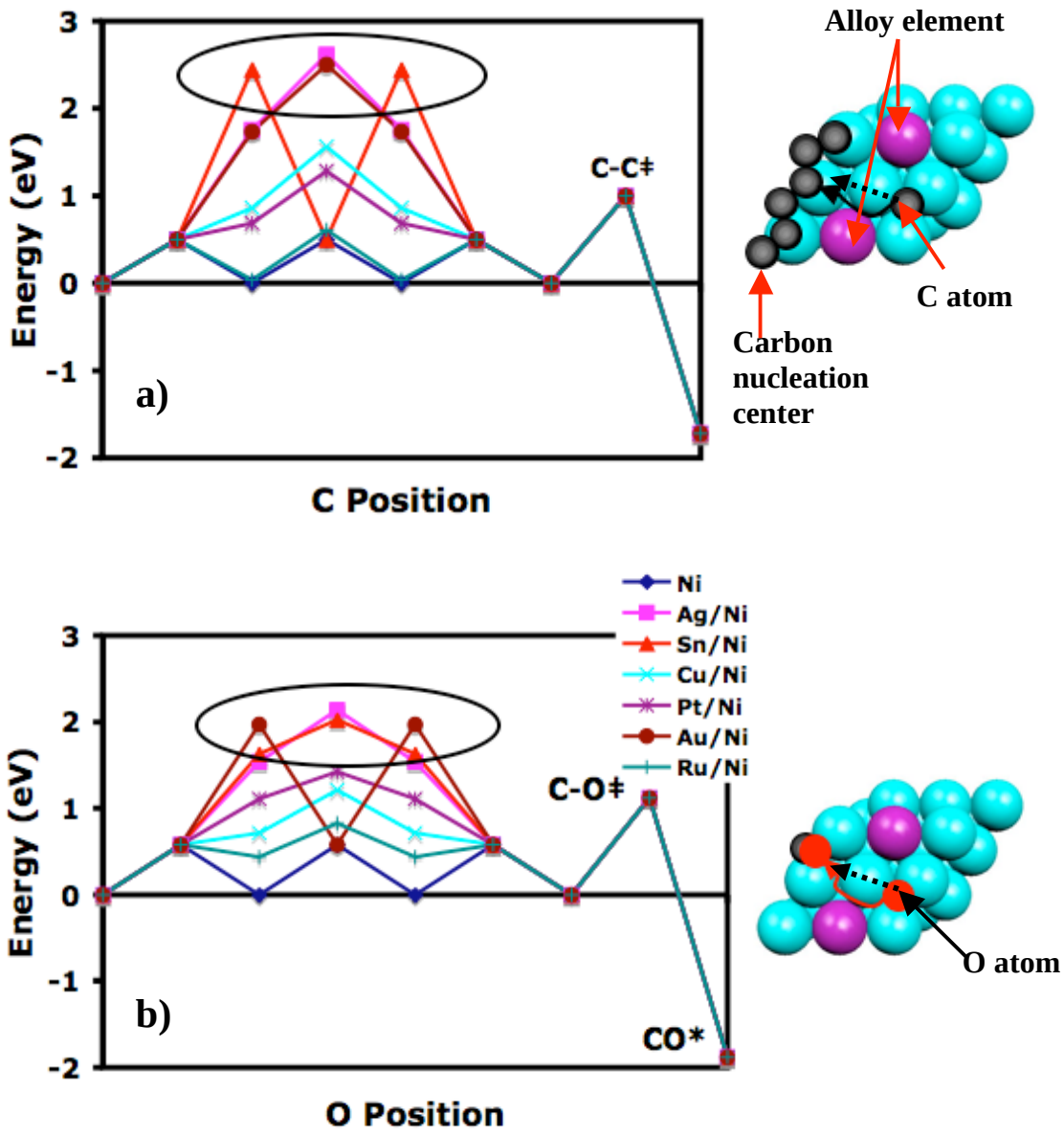

Figure 8.1. a) The lowest potential energy surface for C-C bond formation on monometallic Ni and various Ni surface alloys. The insert shows the model system used to represent the Ni surface alloys and the lowest energy pathway for C diffusion on the Ni alloys and and monometallic Ni (shown with a solid arrow). The lowest energy pathway for C diffusion on Sn/Ni is shown with a dashed arrow. b) The lowest potential energy surface for C-O bond formation on monometallic Ni and various Ni surface alloys. The insert shows the model system used to represent the Ni surface alloys and the pathway for O diffusion on the Ni alloys and monometallic Ni (shown with a solid arrow). The lowest O diffusion pathway on Au/Ni is shown with a dashed arrow.

Figure 8.1 shows the lowest potential energy surfaces for C-O and C-C bond formation on various Ni surface alloys. Ni surface alloys are characterized by an alloy element (i.e. Sn, Au, Ag…) replacing Ni atoms from the Ni surface layer as illustrated by the inserts. As we have previously shown in chapter 3, on monometallic Ni (111) the processes of C-O and C-C bond formation are kinetically comparable, indicating that the rates of C-C bond formation on Ni are fairly high. On the other hand, Ni surface alloys such as Au/Ni, Sn/Ni and Ag/Ni induce a barrier for the diffusion of C and O atoms making this step kinetically important in the process of C-C and C-O bond formation respectively. Furthermore, Figure 8.1 shows that Au/Ni, Sn/Ni and Ag/Ni induce a lower energy barrier for O diffusion than C diffusion resulting in a lower energy barrier for the C-O bond formation than the C-C bond formation. Based on these DFT results, one would expect that these alloys would favor the C-O over C-C bond formation thus would be more carbon tolerant catalysts than monometallic Ni. On the other hand, on Cu/Ni , Pt/Ni, Ru/Ni alloys C-O and C-C bond formation processes are kinetically comparable as in the case of Ni. Although this indicates that these alloys (Ru/Ni, Cu/Ni and Pt/Ni) would behave similarly to monometallic Ni, it is hard to assess only based on these results their carbon tolerance since these structures might not be the most stable structures under relevant condition and other mechanisms might be playing a more significant role. For the remaining of the chapter we will mainly focus on Au/Ni, Ag/Ni and Sn/Ni alloys.

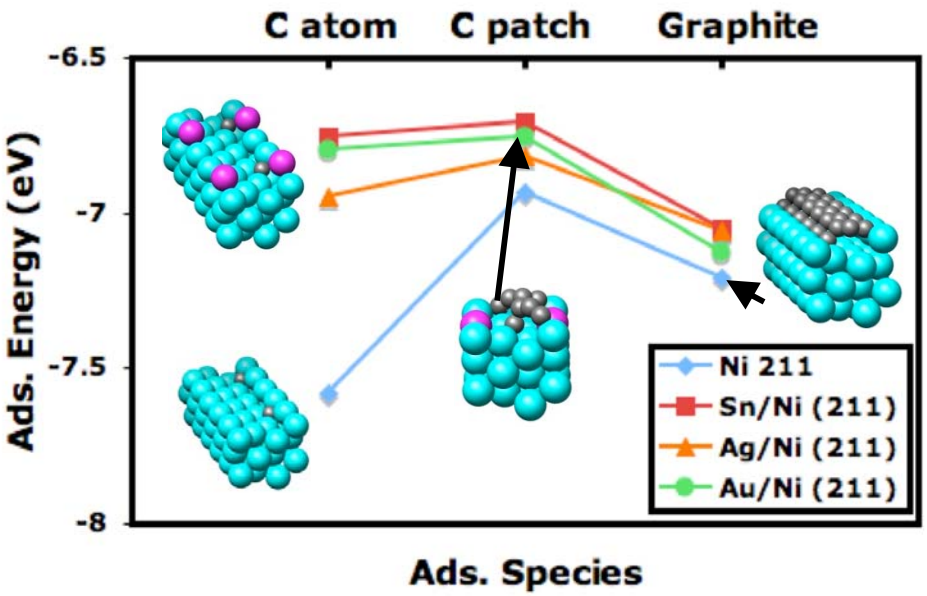

Figure 8.2. DFT-calculated adsorption energies (per one carbon atom) for a C atom, a cluster of 8 C atoms and a graphene sheet adsorbed on Ni (211), Sn/Ni (211), Ag/Ni (211), Au/Ni (211).

As we stated above, carbon nucleation also plays an important role in the growth of extended carbon structures on Ni. To assess whether Au/Ni, Sn/Ni and Ag/Ni surface alloys would affect the process of carbon nucleation on the low-coordinated sites, we have also analyzed the stability of carbon nucleation centers on these sites. Figure 8.2 shows the DFT calculated adsorption energies for various carbon species (i.e. a C atom, a cluster of 8 C atoms and a one-dimensional graphene sheet) on Au/Ni, Ag/Ni, Sn/Ni and monometallic Ni. Figure 8.2 shows that the adsorption energies for all C structures are less endothermic on Au/Ni, Ag/Ni, and Sn/Ni surface alloys than monometallic Ni, suggesting that these surface alloys have a lower thermodynamic driving force to nucleate carbon than monometallic Ni.

Thus far DFT calculations have suggested that Au/Ni, Ag/Ni and Sn/Ni surface alloys might be more carbon tolerant catalysts than monometallic Ni since they favor C-O over C-C bond formation and hinder the nucleation of extended carbon structures. The question now becomes whether we can synthesize these alloys and whether they would be more resistant to carbon-induced deactivation as compared to monometallic Ni under catalytic steam reforming conditions.

8.4.1 Formation of Surface Alloys

We have employed DFT calculations to calculate the formation energies of various surface alloy structures in order to assess the driving force for these alloy to assemble into the preferred surface alloy structures. The aim of this study was to identify thermodynamically the most stable configuration of Au, Ag, Sn with Ni for a given Au, Ag, Sn and Ni concentration. Since we are interested in only slightly perturbing Ni, we have explored only the structures in the limit of low Sn, Au and Ag concentrations. The

formation energies for various Au/Ni, Ag/Ni, and Sn/Ni alloy configurations were calculated with respect to pure Ni slab using the following expression (eqn 1).

$$E = E\,(Ni/X_{slab}) - N(X)\,\mu(X) - N(Ni)\,\mu(Ni) - E_{formation}\,(Ni_{slab}) \qquad \text{eqn 1}$$

$$E_{formation}\,(Ni_{slab}) = E\,(Ni_{slab}) - N\,(Ni_P)\,\mu(Ni) \qquad \text{eqn 2}$$

where X refers to Sn, Au or Ag atoms, $E(Ni/X_{slab})$ and $E(Ni_{slab})$ are the DFT calculated energies of an alloy slab composed of Ni and X (Au, Ag or Sn) atoms and a pure Ni slab respectively, N(X) and N(Ni) correspond to the number of the Sn, Au, Ag and Ni atoms in the alloy slab, $N(Ni_P)$ is the number of Ni atoms in the pure Ni slab, while $\mu(X)$ and $\mu(Ni)$ are the respective chemical potentials of Sn, Au or Ag and Ni atoms. The chemical potential of Sn, Au, Ag and Ni is a function of the concentration of these atoms in a catalytic particle. In this formulation, the formation energy of zero (E = 0) corresponds to the pure Ni slab.

Figure 8.3 shows the calculated formation energies for various Sn/Ni, Au/Ni and Ag/Ni structures at the limit of low Sn, Au, Ag concentrations. The calculations were performed by for a number of alloy configurations using (911) fcc surface terminations in a p(1x3) unit cell. This model system was utilized since it contains well-coordinated terrace sites and under-coordinated step edge sites. Furthermore, due to the fact that the unit cell is fairly large, certain terrace and step sites are sufficiently far away from each other so that they are effectively decoupled. The results in Figure 8.3 indicate that surface alloy structures (i.e where the alloy element replaces Ni atoms from the surface layer) of Au/Ni, Ag/Ni and Sn/Ni have lower formation energies than the structures where the alloy elements (Sn, Au or Ag) replace Ni atoms in the Ni bulk and than the structures where monometallic phase of Ni and the alloy element are separated from each other.

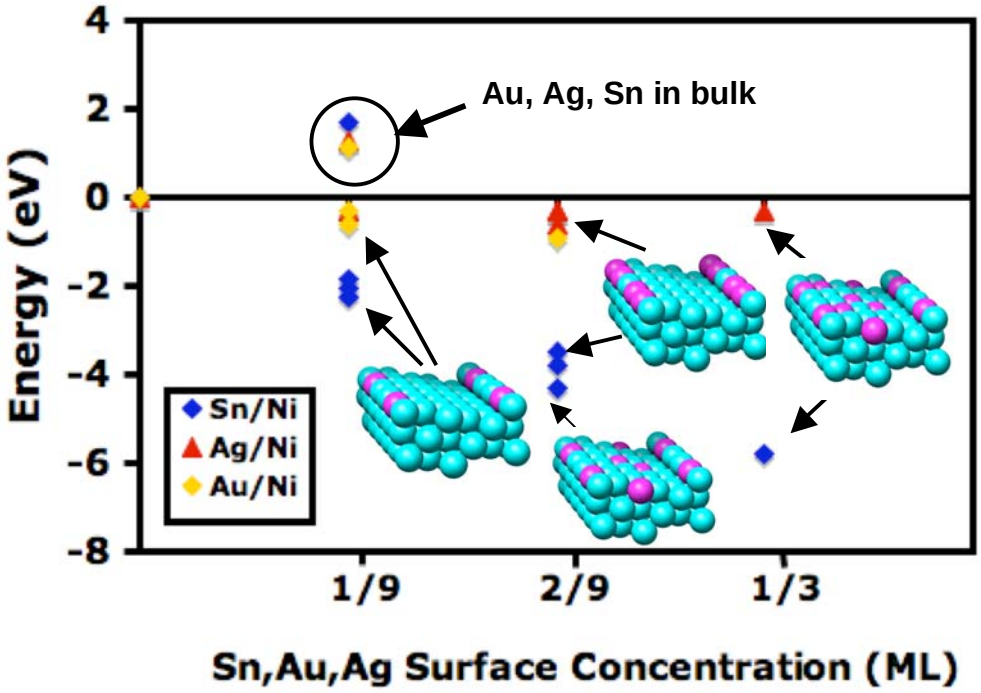

Figure 8.3. DFT-calculated formation energies for various Sn/Ni, Au/Ni and Ag/Ni structures as a function of the Sn, Au and Ag surface concentration respectively. The energies were calculated for (911) fcc surface terminations in a p(1x3) unit cell. The inserts show selected geometries of the Sn/Ni, Ag/Ni and Au/Ni.

For example, at the alloy element concentration of 1/9 ML, the most stable structure for the Sn/Ni, Ag/Ni and Au/Ni is the structure with the dispersed alloy element atoms (Au, Ag, or Sn) replacing Ni atoms at the edge sites. Figure 8.3 also shows that as the concentration of the alloy element atoms is increased, these atoms start displacing Ni atoms from the well-coordinated terrace sites. The results in figure show that if a Ni slab is impregnated with a small concentration of Sn, Au or Ag atoms there is a thermodynamic driving force to form a surface alloy.

We have also utilized the DFT calculated formation energies to determine the free energy of formation of a spherical catalytic particle with a given diameter composed of Ni and an alloy element such as Au, Ag or Sn with respect to a reference state which is a catalytic particle with an identical geometry and the same number of Ni and alloy element atoms arranged in a dilute bulk alloy structure. The free energy of formation of the particle is calculated as a function of moving atoms of the alloy element (Sn, Ag or Au) from the bulk to the surface layer (i.e. surface segregation of the alloy element) of the Ni particle. The free energy of formation of the particle is calculated using the following expression.

$$G_{formation}^{particle} = E_{seg} * N(X_{surface}) + \Delta T * S_{bulk}^{conf} * N_{bulk} + T * \Delta S_{surface}^{conf} * N_{surface}$$

eqn 3

Where E_{seg} is the energy cost or gain to change a slab with a dilute bulk alloy structure (characterized by an alloy element (Au, Ag, Sn) replacing the Ni atoms from the bulk layers) to a slab with a surface alloy structure characterized by the alloy element (Au, Ag or Sn) replacing Ni atoms from the surface layers (i.e. segregation of the alloy element atoms from the bulk to the surface), $N(X_{surface})$ is the number of atoms of the alloy

element (Au, Ag or Sn) in the surface layer of the particle, N_{bulk} and $N_{surface}$ are the total number of atoms in the bulk and surface layers of the particle respectively, and ΔS_{bulk}^{conf} and $\Delta S_{surface}^{conf}$ are the configurational entropies of the bulk and surface layers respectively. In this formulation, we have assumed that the contributions of the vibrational free energy to the free energy are negligible.

The segregation energy (E_{seg}) is calculated as follows.

$$E_{seg} = E_{formation}^{slab}(Ni/X_{surface}) - E_{formation}^{slab}(Ni/X_{bulk}) \quad \text{eqn 4}$$

Where $E_{formation}^{slab}(Ni/X_{surface})$ and $E_{formation}^{slab}(Ni/X_{bulk})$ are the formation energies for a surface alloy structure and a bulk alloy structure respectively and were calculated using equations 1 and 2.

Configuration entropies ΔS_{bulk}^{conf} , $\Delta S_{surface}^{conf}$ are the entropies associated with the geometric arrangements of the alloy element (Sn, Au, or Ag) in the bulk and surface layers of the Ni particle respectively calculated using equations 8 through 10.

$$\Delta S_{bulk}^{conf} = R*[Y_{bulk}\ln(Y_{bulk}) + (1-Y_{bulk})\ln(1-Y_{bulk})] \quad \text{eqn 8}$$

$$\Delta S_{surface}^{conf} = R*[Y_{surface}\ln(Y_{surface}) + (1-Y_{surface})\ln(1-Y_{surface})] \quad \text{eqn 9}$$

$$Y_{bulk} = \frac{N(X_{bulk})}{N_{bulk}^{total}}, Y_{surface} = \frac{N(X_{surface})}{N_{surface}^{total}} \quad \text{eqn 10}$$

Where X refers to atoms of Sn, Au or Ag, N is the number of atoms, μ is the chemical potential, R is the gas constant, Y_{bulk}, $Y_{surface}$ are the mole fractions of the alloy element (Sn, Ag or Au) in the bulk and surface layers of a Ni particle respectively.

Figure 4 shows the free energy of formation for a particle with a diameter of 150 nm composed of 1 wt% Sn and 99 wt% Ni as a function of the Sn surface concentration.

We find that the free energy of the particle decreases as the Sn atoms are moved from the bulk of the particle (the initial configuration) to the surface until the total Sn surface coverage reaches approximately 0.33. The figure suggests that the most stable configuration for a catalytic particle of 150 mn diameter composed of 99 % Ni and 1 % Sn by weight is a surface alloy with ~ 3/9 of the surface occupied by Sn. The rest of Sn atoms would move sub-surface.

A similar analysis was conducted for the Au/Ni system. Figure 8.5 shows the free energy of formation for a 150 nm diameter particle with 1 wt % Au and 99 wt % Ni as a function of the Au surface coverage. The energy is reported with respect to the structure where Au atoms are dispersed in the bulk of a Ni particle in a dilute limit, i.e., there is no interaction among the Au particles in the bulk. The energy of the particle is calculated as Au atoms are moved from the bulk to the surface layer of the particle. We find that the free energy of the particle decreases as the surface gets populated with Au atoms until it reaches an Au surface coverage of approximately 0.23. Figure 8.5 indicates that the most stable structure of a 150 nm particles with 1 wt % Au and 99 wt% Ni is a surface alloy with the Au surface concentration of 23 %.

In the discussion above we have described DFT calculation, which showed that the chemistry of Ag/Ni and Au/Ni alloys is similar to Sn/Ni. The DFT calculations indicated that that at low loadings of impurity elements (i.e. Au., Ag...) the surface alloy is thermodynamically the most stable structure. In the sections below, we describe the results of the experimental studies where these alloy were tested in hydrocarbon steam reforming reactions.

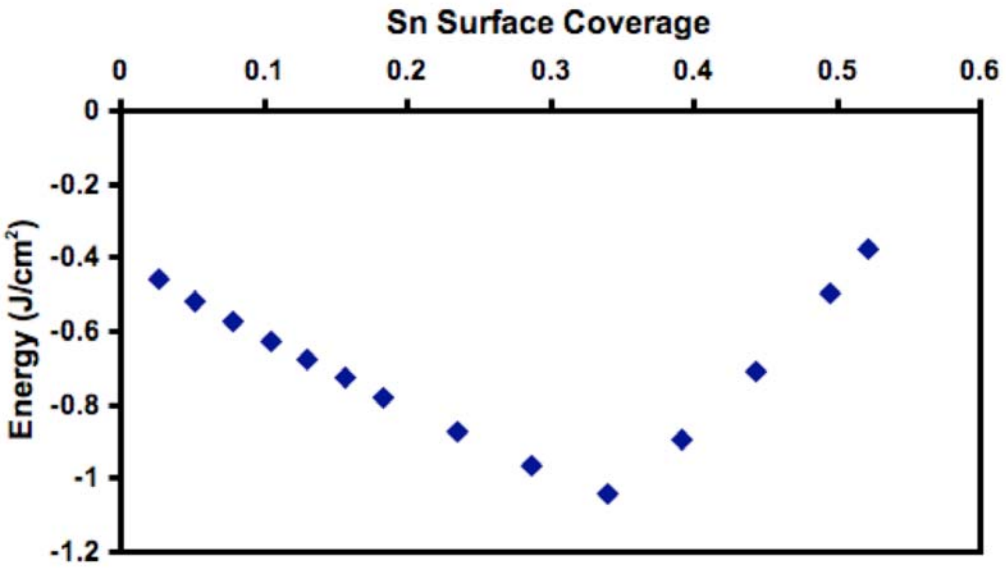

Figure 8.4. Total formation energy of a 150 nm diameter particle composed of 1wt% Sn and 99 wt % Ni as a function of Sn surface coverage. The energy is expressed with respect to the energy of a dilute Sn/Ni bulk alloy.

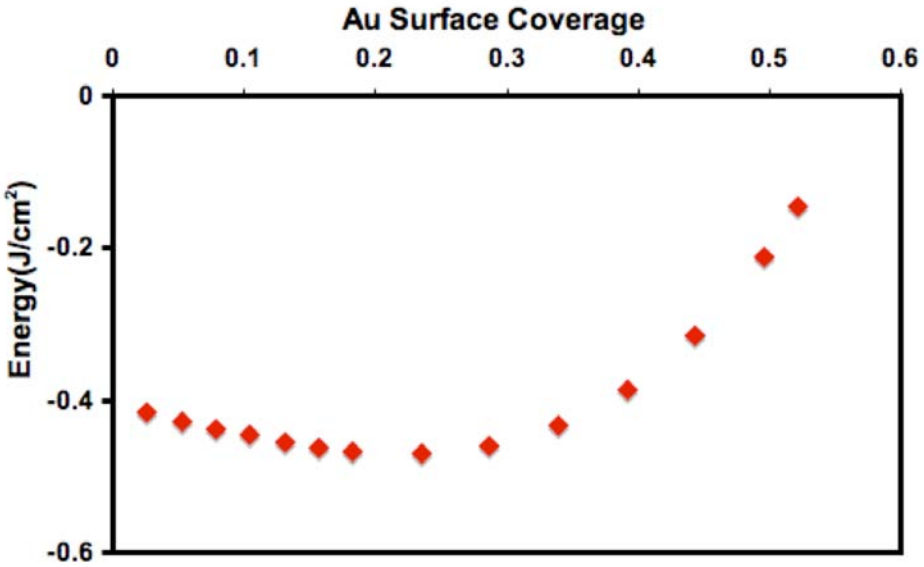

Figure 8.5. Total formation energy of a 150 nm diameter particle composed of 1wt% Au and 99 wt % Ni as a function of Au surface coverage. The energy of the particle is expressed with respect to the energy of a dilute Au/Ni bulk alloy.

Reactor Studies

We have utilized standard synthesis methods (i.e co-impregnation, incipient wetness) to synthesize various Ni alloys. A detailed description of the synthesis methods is given in the Experimental Section. We have employed various experimental techniques to characterize the Ni alloys. These techniques are described in the previous chapters in the context of the characterization of the Sn/Ni alloy. The carbon tolerance of the Ni alloys was assessed in packed bed reactor studies under isooctane steam reforming conditions. Figure 8.6 shows the isooctane conversion as a function of time for Sn/Ni, Ag/Ni and Ni catalysts. The Sn/Ni and Ag/Ni catalysts contained 1 wt% of Sn and Ag with respect to Ni, respectively. Figure 8.6 shows that both Sn/Ni and Ag/Ni are more stable than nonmetallic Ni.

Furthermore we have also utilized thermal gravimetric (TGA) experiments to study carbon formation on the Ni and Ni alloy catalysts during methane decomposition. Figure 8.7 shows the measured weight of the Ni and Ni alloys (Ag/Ni, Au/Ni and Sn/Ni) as a function of temperature during methane decomposition. The increase in the weight of the catalyst is a consequence of the formation of solid carbon deposits. Figure 8.7 shows that Ni/YSZ nucleates carbon at a lower temperature than Sn/Ni, Ag/Ni and Au/Ni alloy catalysts. Furthermore, the amount of carbon deposited on the monometallic Ni is much higher than on Ag/Ni, Au/Ni and Sn/Ni. These results suggest that Sn/Ni, Au/Ni and Ag/Ni alloys are more carbon tolerant catalysts than monometallic Ni.

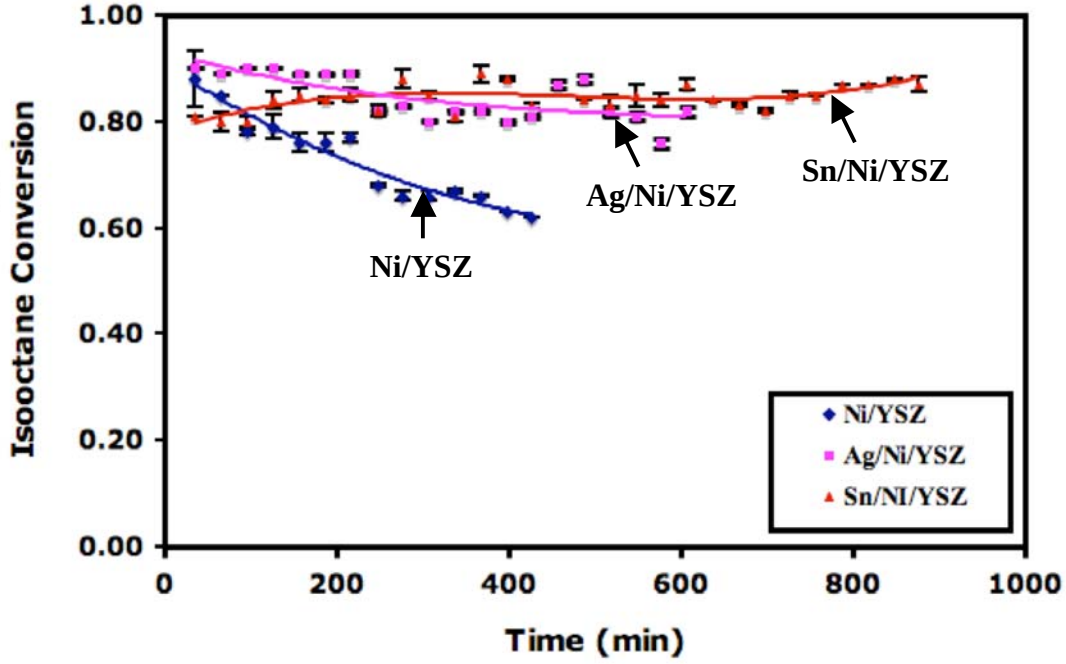

Figure 8.6. Isooctane conversion as a function of time on stream at 1073 K for a Ni/YSZ, Ag/Ni/YSZ and Sn/Ni/YSZ catalyst. The loading of Ag, Sn was 1 wt% with respect to Ni.

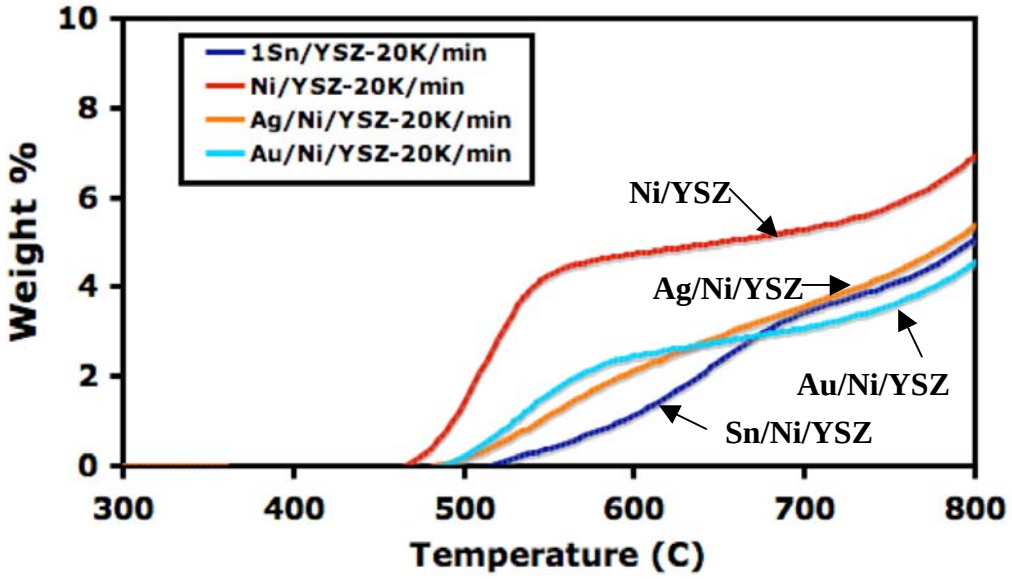

Figure 8.7. A plot of change in the weight of various catalysts (i.e. Sn/Ni/YSZ, Ni/YSZ, Ag/Ni/YSZ and Au/Ni/YSZ) during methane decomposition as a function of temperature obtained using the TGA. The loading of the Sn, Ag, Au was 1 wt % with respect to Ni.

8.5 Conclusion

In this chapter, we have utilized DFT calculation to screen for Ni alloys that might be more carbon tolerant catalysts and electrocatalysts than monometallic Ni. The tolerance toward carbon poisoning of the Ni alloys was assessed by analyzing the process of C-O and C-C bond formation and carbon nucleation on these surfaces using DFT calculations. We found that Au/Ni and Ag/Ni like Sn/Ni are promising carbon tolerant Ni alloys. We also demonstrated how we utilized DFT calculations to determine the most thermodynamically stable structure of these Ni alloys under low concentrations of the alloy element (i.e. Au, Ag). The carbon tolerance of the Ni alloys was tested using packed bed reactor studies and TGA experiments. The results obtained from the experimental studies clearly demonstrated that the Sn/Ni, Ag/Ni and Au/Ni alloys are more carbon tolerant catalysts than monometallic Ni.

8.6 References

1. Bengaard, H.S., et al., *Steam reforming and graphite formation on Ni catalysts.* Journal of Catalysis, 2002. 209(2): p. 365-384.

2. Finnerty, C.M., et al., *Carbon formation on and deactivation of nickel-based/zirconia anodes in solid oxide fuel cells running on methane.* Catalysis Today, 1998. 46(2-3): p. 137-145.

3. Rostrup-Nielsen, J.R., *Catalytic Steam Reforming*, in *Catalysis - Science and Technology*. 1984, Springer: Berlin.

4. Rostrup-Nielsen, J.R., T.S. Christensen, and I. Dybkjaer, *Steam reforming of liquid hydrocarbons.* Recent Advances in Basic and Applied Aspects of Industrial Catalysis, 1998. 113: p. 81-95.

5. Rostrup-Nielsen, J.R., J. Sehested, and J.K. Norskov, *Hydrogen and synthesis gas by steam- and CO_2 reforming.* Advances in Catalysis, Vol 47, 2002. 47: p. 65-139.

6. Takeguchi, T., et al., *Study on steam reforming of CH_4 and C-2 hydrocarbons and carbon deposition on Ni-YSZ cermets.* Journal of Power Sources, 2002. 112(2): p. 588-595.

7. Trimm, D.L., *Coke formation and minimisation during steam reforming reactions.* Catalysis Today, 1997. 37(3): p. 233-238.

8. Linic, S. and M.A. Barteau, *Construction of a reaction coordinate and a microkinetic model for ethylene epoxidation on silver from DFT calculations and surface science experiments.* Journal of Catalysis, 2003. 214(2): p. 200-212.

9. Linic, S., J.W. Medlin, and M.A. Barteau, *Synthesis of oxametallacycles from 2-iodoethanol on Ag(111) and the structure dependence of their reactivity.* Langmuir, 2002. 18(13): p. 5197-5204.

10. Laursen, S. and S. Linic, *Oxidation catalysis by oxide-supported Au nanostructures: The role of supports and the effect of external conditions.* Physical Review Letters, 2006. 97(2)

11. Enever, M., et al., *Synthesis, structure, and reactions of stable oxametallacycles from styrene oxide on Ag(111).* Journal of Physical Chemistry B, 2005. 109(6): p. 2227-2233.

12. Henkelman, G., B.P. Uberuaga, and H. Jonsson, *A climbing image nudged elastic band method for finding saddle points and minimum energy paths.* Journal of Chemical Physics, 2000. 113(22): p. 9901-9904.

13. Mills, G., H. Jonsson, and G.K. Schenter, *Reversible Work Transition-State Theory - Application to Dissociative Adsorption of Hydrogen.* Surface Science, 1995. 324(2-3): p. 305-337.

14. Linic, S. and M.A. Barteau, *On the mechanism of Cs promotion in ethylene epoxidation on Ag.* Journal of the American Chemical Society, 2004. 126(26): p. 8086-8087.

15. Helveg, S., et al., *Atomic-scale imaging of carbon nanofibre growth.* Nature, 2004. 427(6973): p. 426-429.

16. Abild-Pedersen, F., et al., *Mechanisms for catalytic carbon nanofiber growth studied by ab initio density functional theory calculations.* Physical Review B, 2006. 73(11)

17. Besenbacher, F., et al., *Design of a surface alloy catalyst for steam reforming.* Science, 1998. 279(5358): p. 1913-1915.

CHAPTER 9
GENERAL CONCLUSIONS AND FUTURE WORK

This is not the end.
It is not even the beginning of the end.
But it is, perhaps, the end of the beginning.
(Winston Churchill, 1874 - 1965)

9.1 Summary

In this thesis we have employed a hybrid experimental/theoretical approach to study the chemistry of carbon on Ni and Ni alloys aimed at developing carbon tolerant anode electrocatalysts for solid oxide fuel cells (SOFCs). The combination of the various experimental techniques with state-of-the-art theoretical calculations was instrumental in the identification of Ni surface alloys as promising carbon tolerant catalysts and electrocatalysts. Furthermore, we have also utilized electron microscopy and spectroscopy to experimentally measure the electronic structure of nonmodel supported catalysts and have related it to the catalytic performance of these materials. In this chapter we outline some of the major conclusions of the thesis and discuss possible future directions of this work.

9.2 General Conclusions

This work presents a rare example where density functional theory (DFT) calculations in concert with various experimental techniques were employed in identifying improved heterogeneous catalysts and electrocatalysts. The utility of the combined experimental/theoretical approach was illustrated through the example of carbon poisoning of Ni based catalysts and electrocatalysts. Carbon-induced deactivation of Ni reforming catalysts and electrocatalysts has been a major obstacle for the stability of the steam reforming catalysts and the implementation of on-cell hydrocarbon reforming SOFCs. The main conclusion derived from this work were:

- We found using DFT calculations that the process of carbon poisoning is governed by the nucleation of carbon on low coordinated Ni surface sites and the diffusion of carbon to these sites. We also found that a process that competes with the nucleation and growth of carbon deposits is the oxidation of carbon atoms. Based on these insights we developed a strategy for the identification of alloy catalysts that are more carbon-tolerant than monometallic Ni. Our strategy was based on finding materials that favor the formation of C-O over C-C bonds and hinder the nucleation of carbon at the low coordinated sites.
- We identified based on the DFT insights Ni surface alloys (i.e. Sn/Ni, Au/Ni, Ag/Ni) as carbon tolerant catalysts and electrocatalysts. The carbon tolerance of the Ni surface alloys was tested using various experimental techniques including reactor studies, isotope labeling experiments, electrochemical testing (impedance spectroscopy, linear sweep voltammetry..) as well as numerous microscopy and spectroscopy techniques.

- Using kinetic measurements, isotope labeling, microscopic and spectroscopic experiments, we determined that the difference in the chemical activity of the Ni alloys from monometallic Ni was governed by both geometric (i.e. alloy element (Sn, Au or Ag) replacing Ni atoms from the active sites resulting in the change of the active sites) and electronic (i.e. alloying of the Sn, Au or Ag with Ni leading to the change in the electronic structure of Ni atoms in the alloy which changes the chemistry on the surface) effects.
- We determined using electron microscopy and spectroscopy that in Ni alloys, new electronic states form in response to alloying and that the electronic charge is preserved on constituent alloy elements. The change in the electronic structure has an effect in the chemical and catalytic activity of Ni alloys because in order to account for conservation of charge and the creation of the new electronic states, the average energy of the d electrons (the d-band center) of Ni atoms in Ni alloys has to shift down in energy thus leading to Ni atoms in Ni alloys that interact weaker with various adsorbates as compared to monometallic Ni. Based on our analysis, we derived a framework for predicting the changes in the electronic structure of materials induced by alloying and the effect of these electronic changes on the chemical and catalytic activity of these materials.

In this thesis, we have employed a breadth of experimental techniques along with DFT calculations to derive to the conclusions outlined above. For example, various spectroscopic and microscopic techniques including x-ray diffraction (XRD), scanning electron microscopy (SEM), transmission electron microscopy (TEM), scanning

transmission electron microscopy (STEM), x-ray photoelectron spectroscopy (XPS), energy x-ray dispersive spectroscopy (EDS), Auger electron spectroscopy (AES) and electron energy loss spectroscopy (EELS) allowed for a thorough characterization of the catalysts and solid oxide fuel cells (SOFCs). We have also employed EELS and AES to measure the electronic structure of Ni and Ni alloy catalysts and related the electronic structure to their chemical properties of these materials.

The work presented in this thesis is significant to the field heterogeneous catalysis since it is a rare example that demonstrates the value of DFT methodology as a predictive tool in heterogeneous catalysis. In the recent years, DFT methodology has emerged as a method that is not only utilized to explain observable phenomena but also as a tool to obtain fundamental insights regarding a chemical process that can lead to the development of new or improved heterogeneous catalysts. In the work presented herein, DFT was instrumental in predicting Ni surface alloys as more carbon tolerant catalysts and electrocatalysts than monometallic Ni.

9.3 Future Research Directions

In this thesis, we have mainly focused on the identification of carbon tolerant electrocatalysts for SOFC anodes. Another challenging problem for on-cell reforming SOFCs is sulfur poisoning of the anode electrocatalysts.[1] Contributions of others have shown that the current Ni/YSZ anodes deactivate dramatically upon exposure to small concentrations of sulfur compounds such as H_2S.[2, 3] Even if one uses a desulfurizer in front of a SOFC, small amounts of sulfur can slip through the desulfurizer and deactivate the SOFC anodes. Future research should focus on identifying materials that are more resistant to sulfur poisoning thus can operate at higher concentrations of sulfur-containing

compounds than Ni. A similar approach to the one utilized in this thesis, combining experimental and theoretical techniques, could be implemented in identifying ways to prevent sulfur poisoning of the electrocatalysts. Since herein we demonstrated that Ni surface alloys are resilient to carbon poisoning, a natural approach would be to test their ability toward sulfur poisoning. In order to understand the interaction of these materials with sulfur, one could employ DFT to understand the chemistry of sulfur on these surfaces. The promising materials can be tested using both packed bed reactor studies and electrochemical experiments in a SOFC test station.

Another natural extension of the work presented in this thesis would be to utilize the tools employed herein to improve the stability and performance of other SOFC components such as the cathode. It has been shown that the commonly utilized SOFC cathode electrocatalysts (lanthanum strontium manganite (LSM)) deactivate quite significantly over time.[4, 5] This deactivation has been attributed to several factors such as the impurities in the air, the migration of the interconnect materials to the cathode and the change in the structure of the LSM as a function of the oxygen chemical potential.[6, 7] In order to improve the stability or identify new cathode materials, a better understanding of the chemical transformations that lead to deactivation of the cathodes is required. One could utilize DFT to obtain insights regarding the chemical transformations that lead to cathode deactivation. This information can be then utilized to identify ways to improve the stability of the cathode electrocatalysts.

9.4 References

1. Matsuzaki, Y. and I. Yasuda, *The poisoning effect of sulfur-containing impurity gas on a SOFC anode: Part I. Dependence on temperature, time, and impurity concentration.* Solid State Ionics, 2000. 132(3-4): p. 261-269.

2. Sasaki, K., et al., *H_2S poisoning of solid oxide fuel cells.* Journal of the Electrochemical Society, 2006. 153(11): p. A2023-A2029.

3. Zha, S.W., Z. Cheng, and M.L. Liu, *Sulfur poisoning and regeneration of Ni-based anodes in solid oxide fuel cells.* Journal of the Electrochemical Society, 2007. 154(2): p. B201-B206.

4. Yokokawa, H., et al., *Fundamental mechanisms limiting solid oxide fuel cell durability.* Journal of Power Sources, 2008. 182(2): p. 400-412.

5. McIntosh, S., et al., *Effect of polarization on and implications for characterization of LSM-YSZ composite cathodes.* Electrochemical and Solid State Letters, 2004. 7(5): p. A111-A114.

6. Jorgensen, M.J., P. Holtappels, and C.C. Appel, *Durability test of SOFC cathodes.* Journal of Applied Electrochemistry, 2000. 30(4): p. 411-418.

7. Koch, S., et al., *Solid oxide fuel cell performance under severe operating conditions.* Fuel Cells, 2006. 6(2): p. 130-136.